INTERPRETING HORIZONTAL WELL FLOW PROFILES AND OPTIMIZING

WELL PERFORMANCE BY DOWNHOLE TEMPERATURE AND

PRESSURE DATA

A Dissertation

by

ZHUOYI LI

Submitted to the Office of Graduate Studies of
Texas A&M University
in partial fulfillment of the requirements for the degree of

DOCTOR OF PHILOSOPHY

December 2010

Major Subject: Petroleum Engineering

INTERPRETING HORIZONTAL WELL FLOW PROFILES AND OPTIMIZING

WELL PERFORMANCE BY DOWNHOLE TEMPERATURE AND

PRESSURE DATA

A Dissertation

by

ZHUOYI LI

Submitted to the Office of Graduate Studies of
Texas A&M University
in partial fulfillment of the requirements for the degree of

DOCTOR OF PHILOSOPHY

Approved by:

Chair of Committee,	Ding Zhu
Committee Members,	A. Daniel Hill
	Akhil Datta-Gupta
	Yalchin Efendiev
Head of Department,	Stephen A. Holditch

December 2010

Major Subject: Petroleum Engineering

ABSTRACT

Interpreting Horizontal Well Flow Profiles and Optimizing Well Performance by

Downhole Temperature and Pressure Data. (December 2010)

Zhuoyi Li, B.E., Tsinghua University (Beijing);

M.E., Tsinghua University (Beijing)

Chair of Advisory Committee: Dr. Ding Zhu

Horizontal well temperature and pressure distributions can be measured by production logging or downhole permanent sensors, such as fiber optic distributed temperature sensors (DTS). Correct interpretation of temperature and pressure data can be used to obtain downhole flow conditions, which is key information to control and optimize horizontal well production. However, the fluid flow in the reservoir is often multiphase and complex, which makes temperature and pressure interpretation very difficult. In addition, the continuous measurement provides transient temperature behavior which increases the complexity of the problem. To interpret these measured data correctly, a comprehensive model is required.

In this study, an interpretation model is developed to predict flow profile of a horizontal well from downhole temperature and pressure measurement. The model consists of a wellbore model and a reservoir model. The reservoir model can handle transient, multiphase flow and it includes a flow model and a thermal model. The calculation of the reservoir flow model is based on the streamline simulation and the

calculation of reservoir thermal model is based on the finite difference method. The reservoir thermal model includes thermal expansion and viscous dissipation heating which can reflect small temperature changes caused by pressure difference. We combine the reservoir model with a horizontal well flow and temperature model as the forward model. Based on this forward model, by making the forward calculated temperature and pressure match the observed data, we can inverse temperature and pressure data to downhole flow rate profiles. Two commonly used inversion methods, Levenberg-Marquardt method and Marcov chain Monte Carlo method, are discussed in the study. Field applications illustrate the feasibility of using this model to interpret the field measured data and assist production optimization.

The reservoir model also reveals the relationship between temperature behavior and reservoir permeability characteristic. The measured temperature information can help us to characterize a reservoir when the reservoir modeling is done only with limited information. The transient temperature information can be used in horizontal well optimization by controlling the flow rate until favorite temperature distribution is achieved. With temperature feedback and inflow control valves (ICVs), we developed a procedure of using DTS data to optimize horizontal well performance. The synthetic examples show that this method is useful at a certain level of temperature resolution and data noise.

DEDICATION

To my parents, sister, and grandmother

ACKNOWLEDGEMENTS

I would like to express my gratitude to my advisor Dr. Zhu for her support, guidance, and encouragement throughout my graduate studies.

I also thank my committee members, Dr. Hill, Dr. Datta-Gupta, and Dr. Efendiev, for their suggestion and help in my research study.

I appreciate my friends' help too.

NOMENCLATURE

A	section area of the pipe
a	coefficient defined in Eq. 2.40
AB	coefficient defined in Eq. 2.34
AE	coefficient defined in Eq. 2.34
AN	coefficient defined in Eq. 2.34
AP	coefficient defined in Eq. 2.34
AS	coefficient defined in Eq. 2.34
AT	coefficient defined in Eq. 2.34
AW	coefficient defined in Eq. 2.34
B	coefficient defined in Eq. 2.34
$\mathbf{C}$	covariance matrix
C_p	heat capacity
D	depth
D_T	weight of temperature in objective function
D_p	weight of pressure in objective function
$\mathbf{d}$	observed data
$\mathbf{e}$	error or residual vector between observation and model calculation
F_w	fraction flow
f	friction factor

f	objective function
G	sensitivity matrix
g	model calculated data
g	gravity
H	Hessian matrix
H	enthalpy
I_{ani}	anisotropy ratio
I	identify matrix
J	Jacobian matrix
K	thermal conductivity
K_{Tt}	total thermal conductivity in reservoir
k	permeability
k_d	damage permeability
k_e	effective permeability
k_{ri}	relative permeability of phase i
l	distance
M	constant value to adjust damping factor
N_{Re}	Reynolds number
$N_{Re,w}$	wall Reynolds number
p	pressure
p_d	pressure at damage boundary

p_{grid}	average pressure in a grid
p_{wf}	flowing bottomhole pressure
$\dot{Q}_h$	heat transfer rate
q	flow rate
R	radius of well's wall
r_d	damage radius
r_e	effective radius
r_w	wellbore radius
S	saturation
T	temperature
T_I	arriving temperature
T_{grid}	grid temperature
t	time
U	internal energy
u	Darcy velocity
V	arbitrary volume
$\mathbf{v}$	velocity vector
v	velocity
v_s	superficial velocity
$\mathbf{w}$	derivative vector

x	parameter vector
y	hold up
Z	kriging function

Greek

α_T	overall heat transfer coefficient
$\alpha_{T,I}$	combined overall heat transfer coefficient
β	thermal expansion coefficient
γ	pipe open ratio
γ	semi-variogram in Chapter V
$\delta\mathbf{x}$	upgrading parameter
θ	wellbore inclination
λ	kriging weight in Chapter V
μ	viscosity
ρ	density
ρ_{prob}	probability density
ϕ	porosity
σ	covariance in normal distribution
ω	coefficient defined in
ϖ	coefficient defined in
τ	time of flight

Λ kriging weight vector

Subscripts

B block in Chapter V

e, eff effective

g gas

I inflow

i phase index

i, j, k position index in Appendix A

l liquid

l phase index in Appendix A

N total parameter number

n iteration step

m total observed data number

o oil

P point in Chapter V

s solid rock

w water

x, y, z position in Appendix A

TABLE OF CONTENTS

LIST OF FIGURES

LIST OF TABLES

Page

CHAPTER I

INTRODUCTION

1.1   BACKGROUND

Horizontal well technology has been widely used to obtain larger contact between wellbore and reservoir. Downhole flow conditions of horizontal well in general are complicate because of a large degree of reservoir heterogeneity being involved compared with vertical wells. With correct understanding of downhole flow conditions, well operation may be applied to improve production, for example, unwanted fluid can be constrained to enter the wellbore. Therefore, diagnosis of horizontal well downhole flow conditions has important impact on production optimization.

One of the commonly used methods to obtain downhole flow conditions is production logging. Spinner flowmeter is one of the most popular conventional ways to generate downhole flow distributions. Profiles of fluid velocities in a well can be obtained by interpreting spinner flowmeter responses. However, in multiphase flow horizontal well, because the well is horizontal, phases will be segregated by gravity. Therefore, spinner flowmeter may involve higher-level of error, and it is hard to identify individual phase flux.

Temperature and pressure data are generally measured during a conventional production logging. Recently, advanced technology, such as distributed temperature sensor (DTS) and downhole permanent pressure sensor, have been installed in horizontal

---

This dissertation follows the style of *SPE Journal*.

wells as a part of well completion. This new technology provides us continuous downhole temperature and pressure data with certain accuracy. It is possible to reveal the downhole flow conditions from interpretation of measured temperature and pressure data.

For horizontal wells, because geothermal temperature changes are relatively small, the dominating effects on the wellbore temperature changes may be thermal expansion, viscous dissipative heating, and thermal conduction. Model for temperature interpretation should be able to handle these subtle thermal effects. These features post additional challenges to methodology development. Over-simplified model will not provide useful information, but too detailed model will result in interpretation difficulties.

1.2   LITERATURE REVIEW

1.2.1   Downhole Temperature Monitoring

Temperature log has been used to evaluate production profiles and problems in the industry, such as detecting water or gas entries, locating casing leaks, identifying injection or production zones (Hill, 1990). As a standard practice of production and diagnosis, production has to be disturbed. When running production logging, it is costly and time consuming, and it is only provides periodical information while logging. Sometimes the information strongly depends on well completions and trajectory, especially for horizontal well.

Currently, new techniques, such as distributed temperature sensor (DTS), have been used to achieve real-time monitoring. Its applications are broad. Foucault et al. (2004) used DTS data to detect the water entry location at a horizontal well. Fryer et al. (2005) monitored the real time temperature profiles to identify and correlate production changes for the well in multizone reservoir. Johnson et al. (2006) and Huebsch et al. (2008) calculated gas flow profiles from the measured DTS data. Julian et al. (2007) showed that DTS data can be used to determine the leak location in vertical wells. Huckabee (2009) applied the DTS data to diagnose the fracture stimulation and evaluate well performance.

DTS technology has shown its great potential of production evaluation. However, temperature data is qualitatively analyzed in most of these previous works. Quantitative interpretation of the temperature data can provide more useful information for understanding the downhole flow condition, adding invaluable benefit to production monitoring and optimization.

1.2.2 Temperature Modeling and Interpretations

One of the earliest works on temperature modeling was proposed by Ramey (1962). Ramey's model can be applied to predict temperature profiles for injection or production wells with only single phase flowing. In this model, no inflow or outflow between the wellbore and the formation, temperature in well is a function of time and depth. The heat conducted radially from the casing to the formation is transient. A time-dependent function is introduced, which is a log linear solution of time, thermal diffusivity, and

radius of outside casing, and depends on the boundary condition assumed for the heat conduction between formation and wellbore.

Satter (1965) modified Ramey's model for steam injection wells by including phase changes. Sagar et al. (1991) extended Ramey's equation to inclined wells, and considered Joule-Thomson effect caused by pressure change along the wellbore. Hasan and Kabir (1994) further developed Ramey's model. They provided an approximate solution of the time-dependent function based on a detailed thermal conduction model of the formation. They also considered the Joule-Thomson effect in the wellbore, and the model can handle two-phase flow. All of the above models assume that there is no fluid transport between wellbore and formation.

To study the transient thermal behavior and allow fluids to entry into the wellbore from different locations along the wellbore, new temperature models were developed. Kabir et al. (1996) derived a detailed wellbore model based on mass, momentum and energy balance. The arriving temperature which implies the inflow fluid temperature at the boundary of outside the wellbore and the reservoir is assumed to be the geothermal temperature. One advantage of this model is that it accounts the tubular heat absorption or the thermal storage effect, which is observed during well testing. Izgec et al. (2006) developed a coupled wellbore/reservoir model for transient fluid and heat flow. In their work, they also assume the arriving temperature is equal to the reservoir geothermal temperature. These works are based on the assumption that fluid flow in the well is single-phase flow.

For vertical or inclined wells, the well temperature change is dominated by heat transfer between the wellbore fluid and the formation. Because of geothermal gradient, formation temperature along the depth of the wellbore changes significantly. At such a situation, some small thermal effects, such as fluid thermal expansion and viscous dissipation heating, can be ignored compared with the heat transfer caused by fluids flow from the formation to the wellbore. Therefore, the above models have been applied in the field. However, for horizontal wells, the geothermal temperature change is very small. At this condition, these small thermal effects become important. We can imagine that if assuming the arriving temperature is equal to geothermal temperature and ignoring the pressure change along the horizontal well, the temperature distribution in a horizontal well should be close to a constant. Many field observations (Carnegie et al., 1998; Chace et al., 2000; Foucault et al., 2004; Heddleston, 2009) showed that temperature distributions in horizontal wells changes along the wellbore, which is not caused by the geothermal temperature. These field measured data indicate that small thermal effects of fluids from formation to wellbore should be included in a more precise thermal model when coupling the well and the reservoir model for horizontal wells.

The early work including these small thermal effects is proposed by Maubeuge et al. (1994). Their reservoir thermal model numerically solves a transient temperature equation which includes thermal expansion and viscous dissipation. However, their wellbore model is not explained clearly in their paper.

Because the DTS technique has been used increasingly, many temperature models (Ouyang and Belanger, 2006; Pinzon et al., 2007; Wang et al., 2008; Yoshioka et

al., 2005; Yoshioka et al., 2007b) have been developed to interpret the DTS data for vertical, inclined or horizontal wells. The significant improvement of these models is that they include subtle thermal changes in the reservoir for multiphase flow wells, comparing with conventional reservoir thermal model used in thermal flooding. These models still assume that the flow in the wellbore is steady state. Most of them assume the arriving temperature is equal to geothermal temperature plus the Joule Thomson effect, and the pressure used to calculate Joule Thomson effect is equal to average drawdown pressure. In Pinson's work, they pointed out that the relation overestimates the temperature change. This was also noticed by Brady et al. (1998) who used half of the pressure drawdown to calculate the Joule Thomson effect. In Yoshioka's model, the reservoir model is segmented into finite pieces. Over each segment, the flow is single phase, steady sate flow, and the temperature does not change with time. Analytical solution of reservoir flow was used to describe the pressure and flow relationship, and the arriving temperature is analytically solved.

Besides these steady state models, Duru and Horne (2008), and Sui et al. (Sui et al., 2008b) developed thermal models that consist of both a transient wellbore model and a transient reservoir model. The well models are mainly used for vertical wells, and radial flow assumption is used in the reservoir models. Sui's work also showed that the transient well model can be reduced to steady state condition if observed time is long enough, for example, days (Sui, 2009).

Based on these models, measured temperature data can be interpreted for different applications, such as diagnosing downhole flow rate profiles, detecting water

entry, and determining reservoir and formation damage permeabilities. Generally, the interpretation is based on a forward thermal model and an inversion method to minimize the least-square difference between the forward calculated result and the observed data. Sui et al. (2008a), and Yoshioka et al. (2007a) used the standard gradient based method, Levenberg-Marquardt method, in their inversion, and Donovan et al. (2008) used a probalistic production model for their temperature interpretation. All of these results proved the success of temperature data applications in analyzing wellbore downhole conditions.

Additionally, inflow control valves (ICV) are increasingly used in horizontal wells. These equipments can regulate the inflow fluid for horizontal wells, which may optimize production. Alhuthali et al. (2007) proposed a rate control method to obtain uniform travel time based on streamline method. This method is based on known geology characteristic of the reservoir. For unknown geology characteristic, operating the ICVs based on this method requires other information, such as measured temperature, to analysis whether the operation of ICVs achieves the design of the controlling rate.

1.3 OBJECTIVES

The objective of this study is to interpret measured temperature and pressure data to downhole flow conditions in horizontal wells for completely transient flow conditions. The interpretation is based on a detailed thermal model. Though numerous wellbore models are developed, the reservoir models coupled with the wellbore models still have

limitations. For transient, multiphase flow in horizontal wells, the coupled reservoir model for temperature interpretation should have functions to predict complex flows, and accounts for subtle thermal effects of fluid thermal expansion and viscous dissipation heating when fluid flows from the reservoir to the wellbore.

In this study, we first develop a transient, multiphase flow, 3D reservoir model based on streamline simulation for reservoir flow calculation and finite difference method for temperature calculation. The reservoir thermal model includes thermal expansion and viscous dissipation heating. Then we obtain a forward model by integrating the reservoir model and a previous published well model (Yoshioka et al, 2005). Although the wellbore thermal model is under steady state assumption, temperature was updated at each time step sequentially after solving the reservoir temperature.

From the forward model, we invert observed temperature and pressure data to flow rate profiles by using inversion methods. We also apply this model to field applications, use temperature data to generate reservoir characteristics, and optimize intelligent horizontal well performance by monitoring real time temperature feedback with a rate control method. The results shown in this study illustrates how temperature data can help to monitor, control and optimize oil and gas production.

CHAPTER II

FORWARD MODEL

2.1 INTRODUCTION

In this chapter, we develop a forward model to predict downhole temperature, pressure and flow rate profiles for horizontal wells. The forward model consists of a wellbore model and a reservoir model.

The wellbore model is a steady state model. It includes a wellbore flow model calculating pressure and fluid velocity distributions along wellbore, and a wellbore thermal model solving the wellbore temperature distribution. The model includes detailed heat transfer mechanism to predict wellbore temperature.

The reservoir model is a transient, multiphase flow, 3D model which is based on streamline simulation for reservoir flow calculation and finite difference method for temperature calculation. The reservoir thermal model includes thermal expansion and viscous dissipation heating which can reflect small temperature changes caused by pressure difference. At each time step, the wellbore temperature is updated based on the reservoir temperature to count on the temperature change as a function of time.

All of the wellbore model equations and the reservoir model equations are discretized to solve by numerical simulation. An integrated model is developed to couple temperature behavior at the contact between the wellbore and the reservoir. Combing the wellbore model, the reservoir model, and the integrated model, we can obtain transient

pressure, temperature, and flow rate profiles along wellbore by applying appropriate initial and boundary conditions.

2.2 WELLBORE MODEL

The model developed by Yoshioka et al. (2005, 2007b) was adopted directly in this study. Fig. 2.1 shows a differential volume element of a wellbore, and the reservoir fluid flows into the well through the wall of wellbore. Wellbore flow and thermal behaviors are steady state.
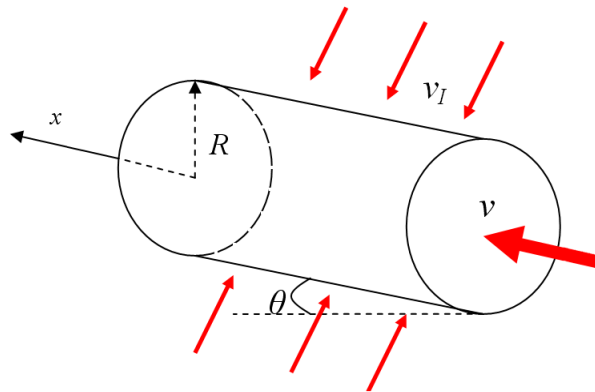
Fig. 2.1 Differential volume element of a wellbore

2.2.1 Wellbore Flow Model

The velocities in wellbore and at the wall of well are represented by:

$$\mathbf{v} = \begin{pmatrix} v_x \\ v_r \\ v_\theta \end{pmatrix} = \begin{cases} \begin{pmatrix} v \\ 0 \\ 0 \end{pmatrix} & \text{in wellbore} \\ \begin{pmatrix} 0 \\ v_I \\ 0 \end{pmatrix} & \begin{array}{c} \text{at well's wall} \\ r = R \end{array} \end{cases} \quad \text{.. (2.1)}$$

where **v** is the velocity vector and the subscript I means arriving. Fig. 2.1 illustrates the velocity component in the system. In the wellbore, the velocity vector in wellbore has only one component at axial (x) direction, and the arriving velocity vector at well's wall (r=R) has only one component at radial (r) direction.

Mass Balance

Considering the fluid flows from reservoir into wellbore, the mass balance equation for each phase is

$$\frac{d(\rho v y)_i}{dx} = \frac{2\gamma}{R}(\rho_I v_I)_i \quad \text{.. (2.2)}$$

where the subscript i is the type of fluid phase, which could be oil, gas, or water. And γ is the ratio of the opening section versus the total well length. For an open hole completion, γ=1. And if the well is partially open to the reservoir though completion, the γ is less than one.

Momentum Balance

Using the momentum balance, the pressure equation can be obtained as follows:

$$\frac{dp}{dx} = -\frac{\rho_m v_m{}^2 f}{R} - \frac{d\left(\rho_m v_m{}^2\right)}{dx} - \rho_m g \sin\theta \quad\text{...} \quad (2.3)$$

where the subscript m denotes the mixed multi-phase fluids, and f is friction factor. For horizontal wells, Ouyang et al. (1998) has presented a friction factor model which states: for laminar flow, the friction factor is independent of completion type and is calculated by:

$$f = \frac{16}{N_{\text{Re}}}\left(1 + 0.04304\left(N_{\text{Re},w}\right)^{0.6142}\right) \quad\text{...} \quad (2.4)$$

For turbulence flow, friction factor is affected by different completion types,

$$f = \begin{cases} f_0\left(1 - 29.03\left(\dfrac{N_{\text{Re},w}}{N_{\text{Re}}}\right)^{0.8003}\right) & \text{openhole completion} \\[4mm] f_0\left(1 - 0.0153\left(N_{\text{Re},w}\right)^{0.3978}\right) & \text{perforated well} \end{cases} \quad\text{........................} \quad (2.5)$$

where N_{Re} and $N_{\text{Re},w}$ are the Reynolds number and the wall Reynolds number. Their definitions are

$$N_{\text{Re}} = \frac{2R\rho v}{\mu} \quad\text{..} \quad (2.6)$$

and

$$N_{\text{Re},w} = \frac{2R\rho_I v_I}{\mu_I} \quad\text{..} \quad (2.7)$$

f_0 is the friction factor without radial influx and is calculated from Moody's diagram or from Chen's correlation (Chen, 1979):

$$f_0 = \left[-4\log\left\{ \frac{\varepsilon}{3.7065} - \frac{5.0452}{N_{Re}}\log\left[\frac{\varepsilon^{1.1098}}{3.7065} + \left(\frac{7.149}{N_{Re}} \right)^{0.8981} \right] \right\} \right]^{-2} \quad \text{.................. (2.8)}$$

where ε is the relative roughness of the pipe.

For multiphase flow conditions, we need to calculate average density and velocity to solve Eq. 2.3. When the flow is oil-water two-phase flow, we assume no slip between phases, and then the mixed velocity can be expressed

$$v_m = \frac{\rho_o}{\rho_m}v_{so} + \frac{\rho_w}{\rho_m}v_{sw} \quad \text{... (2.9)}$$

where v_{sw} and v_{so} represent superficial velocities of water and oil. The oil-water mixture viscosity is estimated by a correlation (Jayawardena et al., 2000):

$$\mu_m = \mu_c\left(1 - y_d\right)^{-2.5} \quad \text{... (2.10)}$$

where the subscript c means continuous phase, d means dispersed phase, and y_d is the holdup of dispersed phase.

When the flow is gas-liquid multi-phase flow, the drift flux model (Ouyang and Aziz, 2000) is used to estimate the pressure gradient. Its final expression (Yoshioka, 2007) is

$$\frac{dp}{dx} = \frac{1}{1-\chi}\left[-\frac{\rho_m v_m^2 f}{R} - \rho_m g \sin\theta + \varpi\left(\frac{dp}{dx} \right)_{aW1} + (1-\varpi)\left(\frac{dp}{dx} \right)_{aW2} \right] \quad \text{............... (2.11)}$$

where

$$\chi = \left(\rho_l v_{sl} + \rho_g v_{sg}\right)\frac{v_{sg}}{p} \quad\text{...} \quad (2.12)$$

$$\left(\frac{dp}{dx}\right)_{aW1} = -\frac{1}{A}\left[\left(v_{sl} + v_{sg}\right)\left(\rho_l v_{I,l} + \rho_g v_{I,g}\right) + \left(\rho_l v_{sl} + \rho_g v_{sg}\right)\left(v_{I,l} + v_{I,g}\right)\right] \quad\text{...........} \quad (2.13)$$

and

$$\left(\frac{dp}{dx}\right)_{aW2} = -\frac{2}{A\rho_m}\left(\rho_l v_{sl} + \rho_g v_{sg}\right)\left(\rho_l v_{I,l} + \rho_g v_{I,g}\right) \quad\text{...} \quad (2.14)$$

Eq. 2.13 and Eq. 2.14 account for the accelation pressure drop casued by wall influx. The subscript s denotes surperficial, l denotes liquid, g denotes gas, A is the section area of the pipe. The value of ϖ is proposed as 0.8 by Ouyang and Aziz (2000).

2.2.2 Wellbore Thermal Model

Wellbore temperature equation is derived from energy balance. It is assumed that the temperature in horizontal well is 1D, steady state. Kinetic energy and viscous shear are ignored because they almost do not affect temperature profiles. The final formulation of temperature in wellbore is:

$$\frac{dT}{dx} = \frac{\left(\rho v C_p K_{JT}\right)_T}{\left(\rho v C_p\right)_T}\frac{dp}{dx} + \frac{2}{R}\frac{\alpha_{T,I}}{\left(\rho v C_p\right)_T}\left(T_I - T\right) - \frac{\left(\rho v\right)_T}{\left(\rho v C_p\right)_T}g\sin\theta \quad\text{.......................} \quad (2.15)$$

where

$$\alpha_{T,I} = \gamma\left(\rho v C_p\right)_{T,I} + (1 - \gamma)\alpha_T \quad\text{...} \quad (2.16)$$

$$\left(\rho v\right)_T = \sum_i \rho_i v_i y_i \quad\text{...} \quad (2.17)$$

$$\left(\rho v C_p\right)_T = \sum_i \rho_i v_i y_i C_{p,i} \quad\text{...} \quad (2.18)$$

and

$$\left(\rho v C_p K_{JT}\right)_T = \sum_i \rho_i v_i y_i C_{p,i} K_{JT,i} \quad\text{...} \quad (2.19)$$

the subscript T means total fluid phases in the flow, and α_T denotes the overall heat transfer coefficient.

The full formulation of α_T was originally presented by Willhite (1967), which includes the heat convection between flowing fluid and inside wall of tubing, heat conduction in tubing wall, casing, and cement, and conduction, natural heat convection, and radiation in annulus between tubing and casing.

In this study, the temperature change in horizontal wells is very small, so we can ignore the natural heat convection and radiation in annulus. Fluid flow in tubing is usually at relatively high Reynolds number, so the thermal resistance by heat convection between flowing fluid and inside wall of tubing can be ignored. And because steel has high thermal conductivity, the thermal resistance of tubing and casing are negligible. Therefore, to calculate α_T, we use a reduced equation presented by Sagar et al. (1991):

$$\alpha_T = \left[r_{tubing-ID} \left(\frac{\ln \frac{r_{ca\sin g-ID}}{r_{tubing-OD}}}{K_{annulus}} + \frac{\ln \frac{r_w}{r_{ca\sin g-OD}}}{K_{cement}} \right) \right]^{-1} \quad\text{... (2.20)}$$

Thus, the overall heat transfer coefficient is constant if the completion structure of a well is specified.

Because the wellbore mass, pressure, and temperature equations are all non-linear equations, they are discretized with a finite difference scheme and solved by numerical simulation.

2.3   RESERVOIR MODEL

In this section, we introduce the reservoir model, which is a transient, multiphase flow, 3D model. The model is based on streamline simulation for reservoir flow calculation and finite difference method for temperature calculation. The reservoir thermal model includes thermal expansion and viscous dissipation heating.

2.3.1   Streamline Simulation for Reservoir Pressure and Saturation

A parallelepiped shaped reservoir is used to develop the reservoir flow and thermal model. For reservoir flow, we use the streamline simulation method (Datta-Gupta and King, 2007; Pollock, 1988) to solve the reservoir pressure and saturation distribution. The streamline simulation is a black oil simulation model that uses mass conservation equation for each phase:

$$\frac{\partial}{\partial t}\left(\rho_i S_i \phi\right)+\nabla \cdot\left(\rho_i \bar{u}_i\right)=0 \quad \text{...} \quad (2.21)$$

and the velocity follows Darcy's law

$$\bar{u}=-\frac{\bar{\bar{k}}}{\mu}\cdot\left(\nabla p+\rho \bar{g}\right) \quad \text{..} \quad (2.22)$$

Streamline is formed based on the velocity field, and the phase saturation is solved along the streamline space. The saturation equation for two-phase slightly compressible fluid in streamline time of flight coordinate is

$$\frac{\partial S_w}{\partial t}+\frac{\partial F_w}{\partial \tau}=0 \quad \text{...} \quad (2.23)$$

where

$$\tau=\int_0^{} \frac{\phi}{\bar{u}} d\xi \quad \text{...} \quad (2.24)$$

is the time of flight, and the fractional flow, F_w, is

$$F_w=\frac{k_{rw}/\mu_w}{k_{rw}/\mu_w+k_{ro}/\mu_o} \quad \text{..} \quad (2.25)$$

where k_r is relative permeability and μ is viscosity. Neglecting the viscosity change, F_w is only a function of saturation.

In this work, a numerical simulation (FrontSim, 2008) was used to obtain the solution of the above equations.

2.3.2 Reservoir Thermal Model

For an arbitrary volume V in reservoir, the energy conservation equation can be expressed as,

$$\begin{Bmatrix} \text{Accumulation} \\ \text{rate of energy} \\ \text{in } V \end{Bmatrix} = \begin{Bmatrix} \text{Net rate of} \\ \text{energy transport} \\ \text{into } V \end{Bmatrix} + \begin{Bmatrix} \text{Rate of energy} \\ \text{production} \\ \text{in } V \end{Bmatrix} \quad \text{......................... (2.26)}$$

Neglecting the kinetic energy change, the accumulation rate in V is (Lake, 1989)

$$\begin{Bmatrix} \text{Accumulation} \\ \text{rate of energy} \\ \text{in } V \end{Bmatrix} = \left(\phi \sum_i \rho_i S_i (U_i + gD) + (1-\phi)\rho_s U_s \right) \Big|_t^{t+dt} \cdot V \quad \text{....................... (2.27)}$$

where the subscript i denotes fluid phase, s is solid rock, U is the internal energy, D is the depth, and S is the saturation.

The energy transport includes convection,

$$\begin{Bmatrix} \text{Convection of} \\ \text{energy transport} \\ \text{into } V \end{Bmatrix} = \sum_i \rho_i \bar{u}_i (H_i + gD) \cdot A \quad \text{.. (2.28)}$$

and conduction

$$\begin{Bmatrix} \text{Conduction of} \\ \text{energy transport} \\ \text{into } V \end{Bmatrix} = (-K_{Tt} \nabla T) \cdot A \quad \text{.. (2.29)}$$

where H is the enthalpy, and K_{Tt} is the total heat conductivity, and A is the surface area of the arbitrary volume V.

For the arbitrary volume *V* in reservoir without a wellbore, the rate of energy production is zero. Substituting Eq. 2.27 through Eq. 2.29 into Eq. 2.26, the reservoir energy conservation can be expressed as

$$-\frac{\partial}{\partial t}\left[\phi\sum_i \rho_i S_i (U_i + gD) + (1-\phi)\rho_s U_s \right]$$

$$= \nabla \cdot \left[\sum_i \rho_i \bar{u}_i (H_i + gD)\right] - \nabla \cdot (K_{Tt}\nabla T) \qquad \text{(2.30)}$$

From the definition of enthalpy and internal energy,

$$dH = C_p dT + \frac{1}{\rho}(1-\beta T)dp \qquad \text{(2.31)}$$

and

$$U = H - p/\rho \qquad \text{(2.32)}$$

and we assume that for the formation rock

$$dU_s \approx C_{ps} dT \qquad \text{(2.33)}$$

Then substituting Eq. 2.31 through Eq. 2.33 into Eq. 2.30, and rearranging it, we can obtain the temperature equation in reservoir as follows:

$$-\left[\sum_i (\phi S_i \rho_i C_{pi}) + (1-\phi)\rho_s C_{ps}\right]\frac{\partial T}{\partial t} + \sum_i \left(\phi S_i \beta_i T \frac{\partial p_i}{\partial t}\right)$$

$$= \sum_i \rho_i \bar{u}_i \cdot C_{pi}\nabla T - \nabla \cdot (K_{Tt}\nabla T) + \sum_i \bar{u}_i \cdot \nabla p_i \qquad \text{(2.34)}$$

$$- \sum_i \beta_i T(\bar{u}_i \cdot \nabla p_i) + \sum_i \rho_i \bar{u}_i \cdot \nabla(gD)$$

On the left hand side of Eq. 2.34, the first term is the accumulative term, and the second term is a thermal expansion term related to transient pressure change. On the right hand side, the first term is the convection term, the second term is the conduction term, the

third one is the viscous dissipation heating, the fourth one is the thermal expansion because of pressure change, and the last term is related to potential energy.

K_{Tt} is the total heat conductivity and its change is not significant. Therefore, it is treated as a constant in this work.

We use the finite difference method to solve the temperature equation numerically. If it is no specified, the top and bottom boundaries are assigned a constant temperature, and all the other reservoir boundaries are set equal to geothermal distributed temperature. Only for water injection cases, two parallel horizontal wells are set near reservoir boundaries, and it is assumed no heat flux at the boundary.

To solve Eq. 2.34, we apply finite difference scheme to discretize the equation. The general form for this discretized equation is:

$$AP_{i,j,k}T_{i,j,k}^{n+1} = AW_{i,j,k}T_{i-1,j,k}^{n+1} + AE_{i,j,k}T_{i+1,j,k}^{n+1} + AS_{i,j,k}T_{i,j-1,k}^{n+1}$$
$$+ AN_{i,j,k}T_{i,j+1,k}^{n+1} + AB_{i,j,k}T_{i,j,k-1}^{n+1} + AT_{i,j,k}T_{i,j,k+1}^{n+1} + B_{i,j,k} \quad \text{..........................} \quad (2.35)$$

The detailed procedure of discretization and coefficients in Eq. 2.35 can be found in Appendix A.

In the numerical simulation, if a reservoir grid has a wellbore segment in it, then its temperature equation, Eq. 2.30, should include the heat transfer between the grid and the wellbore segment into the right hand side. The heat transfer term is

$$\dot{Q}_h\big|_{res-well} = -K_{Tt}\frac{\partial T}{\partial r}\bigg|_{r=r_w} + \sum_i \left(\rho\bar{u}C_p\right)_i \cdot \left(T_{res} - T_I\right) \quad \text{..} \quad (2.36)$$

In this work, the reservoir temperature change is relatively small, so it is assumed that the fluid properties are not affected by temperature change, which implies

that the temperature solution has no influence on the pressure and saturation solution. To couple the pressure, saturation and temperature in numerical simulation, the pressure discretized equation was solved first. Then fluxes were solved from the Darcy's law, and used total velocity tracing 1D streamline. Along streamlines we can calculate saturations based on Eq. 2.23. After that, the saturation in grid is averaged calculated from streamlines to their passing grids. With the pressure and saturation fields, the temperature equation is then solved. For pressure and temperature fields, it uses the same time step for update, which should guarantee that it does not change general streamline pattern, e.g., total time of fight along streamlines do not vary more than 5% (if fail, reduce the time step).

2.4 INTEGRATED MODEL FOR TEMPERATURE AT RESERVOIR AND WELLBORE CONTACT

To solve temperature equations, Eq. 2.15 and Eq. 2.30, we must know the arriving temperature T_I, which is the link between reservoir grid temperature and wellbore temperature. The following assumptions have been made to solve T_I :

1. Reservoir grid temperature and pressure are located at the effective radius, r_{eff}, which follows the definition of Peaceman's model (Peaceman, 1983):

$$r_{eff} = 0.28 \frac{\left[\left(\dfrac{k_z}{k_y}\right)^{0.5} \cdot \Delta y^2 + \left(\dfrac{k_y}{k_z}\right)^{0.5} \cdot \Delta z^2\right]^{0.5}}{\left(\dfrac{k_z}{k_y}\right)^{0.25} + \left(\dfrac{k_y}{k_z}\right)^{0.25}}$$ .... (2.37)

2. The permeability is isotropic and homogenous in reservoir grid, which is given by

$$k_e = \left(k_y \cdot k_z\right)^{0.5}$$ .... (2.38)

3. Fluid flow from the effective radius to the wellbore is radial flow.

4. In one time step, both the pressure and temperature are assumed at steady state.

5. Because the distance from the grid to wellbore is very small, the fluid properties and saturation are treated as constant

6. Effects of capillary pressure and gravity are ignored.

For the grid contains a well in it, Fig. 2.2 illustrates the thermal/flow system used in this work.
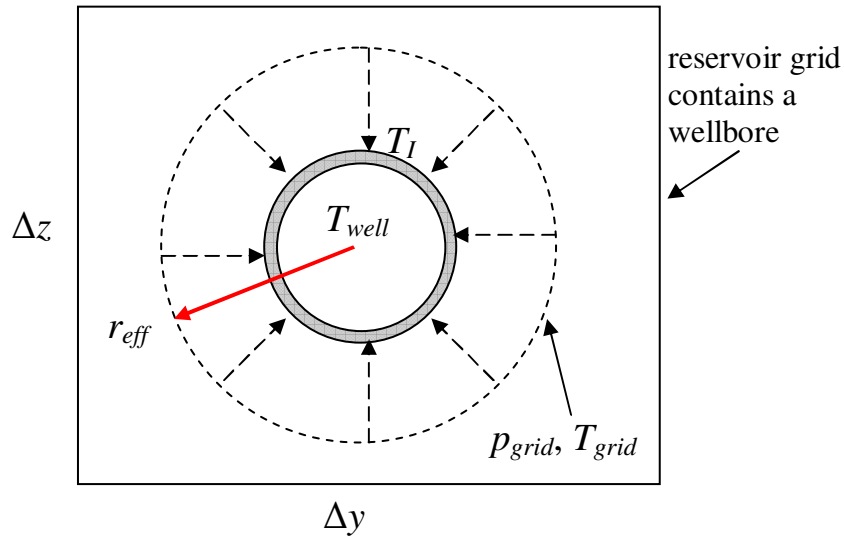
Fig. 2.2 Integrated temperature behavior between reservoir grid and wellbore

Based on these assumptions for coupling the reservoir and wellbore, the pressure distribution from the effective radius to the wellbore is given by

$$\frac{d^2 p}{dr^2} + \frac{1}{r}\frac{dp}{dr} = 0 \quad \text{..} \quad (2.39)$$

Pressure boundary conditions:

$$\begin{cases} r = r_{eff} \ , \ \ at \ \ p = p_{grid} \\ r = r_w \ \ , \ \ at \ \ p = p_{wf} \end{cases} \text{..} \quad (2.40)$$

This equation can be solved analytically for steady-state condition. The solution is

$$p = a\ln\frac{r}{r_w} + p_{well} \quad \text{...} \quad (2.41)$$

where

$$a = \frac{p_{grid} - p_{wf}}{\ln(r_{eff}/r_w)} \quad\text{...} \quad (2.42)$$

The equation described temperature distribution from the reservoir grid to the wellbore outside is

$$\sum_i (\rho_i C_{pi} u_{ri}) \frac{dT}{dr} + \sum_i (\beta_i u_{ri}) T \frac{dp}{dr} + \sum_i (u_{ri}) \frac{dp}{dr} - K_{Tt} \frac{1}{r} \frac{d}{dr}\left(r \frac{dT}{dr}\right) = 0 \quad\text{..............} \quad (2.43)$$

The first term is convection term, the combination of the second and third term is viscous dissipation heating, and the fourth term is the conduction term.

The boundary conditions for the temperature equation are:

$$\begin{cases} T = T_{grid} , & at \quad r = r_{eff} \\ K_{Tt} \left.\frac{dT}{dr}\right|_{r=R} = \alpha_T \left(T|_{r=r_w} - T_w\right), & at \quad r = r_w \end{cases} \quad\text{...} \quad (2.44)$$

First, we get the velocity from Darcy's law for each phase:

$$u_{ri} = -k_e \frac{k_{ri}}{\mu_i} \frac{dp}{dr} = -k_e \frac{k_{ri}}{\mu_i} \frac{a}{r} \quad\text{...} \quad (2.45)$$

Substituting Eq. 2.41, Eq. 2.42, and Eq. 2.45 into Eq. 2.43, and rearranging it, we get a second order partial differential equation of temperature only:

$$\sum_i \left(\rho_i C_{pi} \frac{k_{ri}}{\mu_i} a k_e\right) \frac{1}{r} \frac{dT}{dr} + \sum_i \left(\beta_i \frac{k_{ri}}{\mu_i} a^2 k_e\right) \frac{T}{r^2} +$$
$$\sum_i \left(\frac{k_{ri}}{\mu_i} a^2 k_e\right) \frac{1}{r^2} - K_{Tt} \frac{1}{r} \frac{d}{dr}\left(r \frac{dT}{dr}\right) = 0 \quad\text{....................................} \quad (2.46)$$

Because we assume the fluid properties and saturation are constant in one time step, Eq. 2.46 can be simplified as

$$-K_{Tt}r^2\frac{d^2T}{dr^2}+C_1r\frac{dT}{dr}+C_2T+C_3=0 \dots\dots\dots (2.47)$$

where

$$C_1=\sum_i\left(\rho_iC_{pi}\frac{k_{ri}}{\mu_i}ak_e\right)-K_{Tt}$$

$$C_2=\sum_i\left(\beta_i\frac{k_{ri}}{\mu_i}a^2k_e\right), \qquad \dots\dots\dots (2.48)$$

$$C_3=\sum_i\left(\frac{k_{ri}}{\mu_i}a^2k_e\right)$$

are treated as constant. Solution for this second-order differential equation is

$$T=c_1r^{n_1}+c_2r^{n_2}+b \dots\dots\dots (2.49)$$

where

$$n_1=\frac{-\omega}{2}+\frac{1}{2}\sqrt{\omega^2+4\frac{k_ea^2}{K_{Tt}}\sum_i\left(\frac{k_{ri}}{\mu_i}\beta_i\right)} \dots\dots\dots (2.50)$$

$$n_2=\frac{-\omega}{2}-\frac{1}{2}\sqrt{\omega^2+4\frac{k_ea^2}{K_{Tt}}\sum_i\left(\frac{k_{ri}}{\mu_i}\beta_i\right)} \dots\dots\dots (2.51)$$

$$c_1=\frac{r_{eff}^{n_2}\dfrac{\alpha_T}{K_{Tt}}(b-T_w)-\left(\dfrac{n_2}{r_w}-\dfrac{\alpha_T}{K_{Tt}}\right)r_w^{n_2}(T_{grid}-b)}{\left(\dfrac{n_1}{r_w}-\dfrac{\alpha_T}{K_{Tt}}\right)r_w^{n_1}r_{eff}^{n_2}-\left(\dfrac{n_2}{r_w}-\dfrac{\alpha_T}{K_{Tt}}\right)r_w^{n_2}r_{eff}^{n_1}} \dots\dots\dots (2.52)$$

$$c_2=\frac{\left(\dfrac{n_1}{r_w}-\dfrac{\alpha_T}{K_{Tt}}\right)r_w^{n_1}(T_{grid}-b)-r_{eff}^{n_1}\dfrac{\alpha_T}{K_{Tt}}(b-T_w)}{\left(\dfrac{n_1}{r_w}-\dfrac{\alpha_T}{K_{Tt}}\right)r_w^{n_1}r_{eff}^{n_2}-\left(\dfrac{n_2}{r_w}-\dfrac{\alpha_T}{K_{Tt}}\right)r_w^{n_2}r_{eff}^{n_1}} \dots\dots\dots (2.53)$$

$$\omega = \sum_i \left(\rho_i C_{pi} \left(\frac{k_{ri}}{\mu_i} \right) \right) \frac{k_e a}{K_{Tt}} \quad \text{...} \quad (2.54)$$

and

$$b = \frac{\sum_i \left(\frac{k_{ri}}{\mu_i} \right)}{\sum_i \left(\left(\frac{k_{ri}}{\mu_i} \right) \beta_i \right)} \quad \text{...} \quad (2.55)$$

For the arriving temperature $T_I = T\big|_{r=r_w}$, just substitute $r = r_w$ into Eq. 2.49.

According to these equations, reservoir grid, arriving temperature, and wellbore temperature are coupled together. To uncouple them and reduce the numerical simulation time without losing significant accuracy, we use explicit scheme to estimate the heat transfer term for reservoir grid. Arriving temperature T_I and wellbore temperature T_w are implicit. We iteratively solve the wellbore temperature Eq. 2.15 and the integrated temperature Eq. 2.49, until the solution reaches convergence.

During drilling, completion, and production, formation damage may occur, which will increase the pressure drop for a given flow rate. This change of pressure behavior can affect temperature behaviors. One possible way to account formation damage effect is to use small grid to catch the damage range. However, generally the formation damage range is very small, and small grid requires small time step to satisfy the numerical stability.

Another way to handle formation damage is to keep the same grid distribution, but use a new effective permeability to estimate formation damage. Assume the

formation damage is radial range with permeability k_d and radius r_d, as shown in Fig. 2.3. Peaceman effective radius r_{eff} ($r_{eff} > r_d$) and effective permeability k_e are still calculated by Eq. 2.37 and Eq. 2.38 respectively. The flow from reservoir grid to outside damage range is radial flow, and the flow from outside damage to wellbore is also radial flow. The pressure at outside damage, r_d, is p_d. Thus, the flow rate from the grid to the wellbore at the defined boundary condition is:

$$q_1 = \frac{k_e \Delta x \left(p_{grid} - p_d\right)}{\mu \ln \dfrac{r_{eff}}{r_d}} = \frac{k_d \Delta x \left(p_d - p_w\right)}{\mu \ln \dfrac{r_d}{r_w}} \quad \text{...} \quad (2.56)$$

We use a new effective permeability $k_e^{'}$ to account the formation damage effect, which leads only one permeability range in the grid, showed in Fig. 2.3. Then the flow rate from reservoir grid to wellbore is:

$$q_2 = \frac{k_e^{'} \Delta x \left(p_{grid} - p_w\right)}{\mu \ln \dfrac{r_{eff}}{r_w}} \quad \text{...} \quad (2.57)$$

The production rate from Eq.2.56 and Eq. 2.57 should be the same, thus,

$$\frac{k_e \Delta x \left(p_{grid} - p_d\right)}{\mu \ln \dfrac{r_{eff}}{r_d}} = \frac{k_d \Delta x \left(p_d - p_w\right)}{\mu \ln \dfrac{r_d}{r_w}} = \frac{k_e^{'} \Delta x \left(p_{grid} - p_w\right)}{\mu \ln \dfrac{r_{eff}}{r_w}} \quad \text{...................................} \quad (2.58)$$

The effective permeability is derived as

$$k_e^{'} = \ln \frac{r_{eff}}{r_w} \cdot \left(\frac{1}{k_e} \ln \frac{r_{eff}}{r_d} + \frac{1}{k_d} \ln \frac{r_d}{r_w} \right)^{-1} \quad \text{...} \quad (2.59)$$
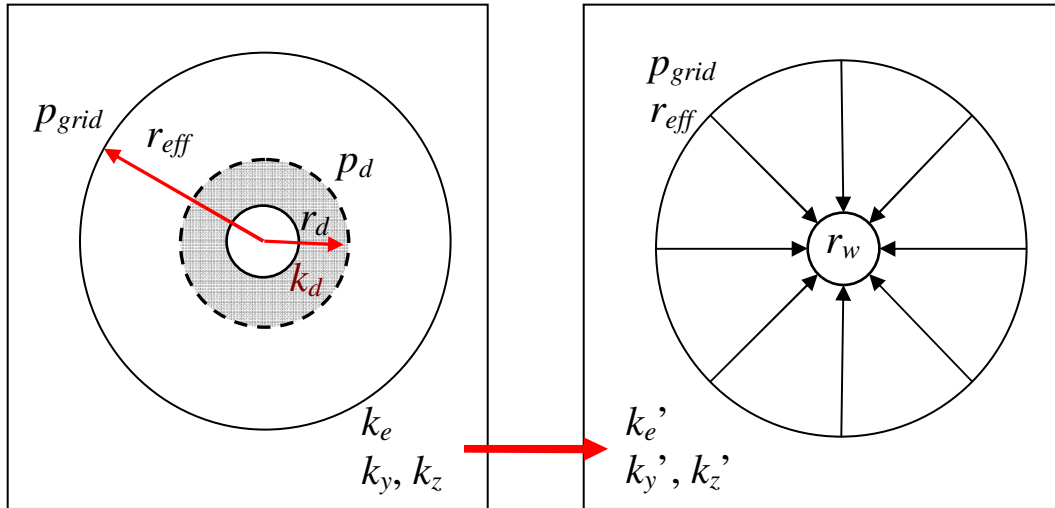
Fig. 2.3 Estimate formation damage effect by effective permeability

According to Eq. 2.38, $k_e = (k_y k_z)^{0.5}$. Substituting anisotropy ratio $I_{ani}^2 = k_H / k_V$, we can obtain

$$k_y' = I_{ani}^2 k_z' = I_{ani} \cdot k_e' \dots\dots\dots\dots\dots\dots\dots\dots\dots\dots\dots\dots\dots\dots\dots\dots (2.60)$$

Therefore, we just need to change permeability in the reservoir grids containing a wellbore segment to the permeability defined by Eq. 2.59 and Eq. 2.60, and then we can account for the formation damage effect.

This estimation is reasonable. For example, if $r_d = r_w$, or $k_d = k_e$, which means no formation damage. Eq. 2.54 yields $k_e' = k_e$. If k_d approaches to zero, the $k_e' = k_d \ln(r_{eff} / r_w)(\ln(r_d / r_w))^{-1}$ is also close to zero. The inflow rate decreases to zero.

2.5   SOLUTION PROCEDURE AND MODEL VALIDATION

Because we assume reservoir temperature change does not affect fluid properties during the transient behavior, reservoir pressure and saturation calculation is independent to reservoir temperature calculation. Fig. 2.4 shows the calculation procedure of the forward model.

time N

Step 1: Run streamline simulation for reservoir saturation and pressure distribution

Step 2: Solve wellbore pressure

Step 3: Solve reservoir temperature using reservoir p, $S_{w, o, g}$

Step 4: Solve wellbore temperature with the temperature integration relation between the reservoir and the wellbore

time N+1
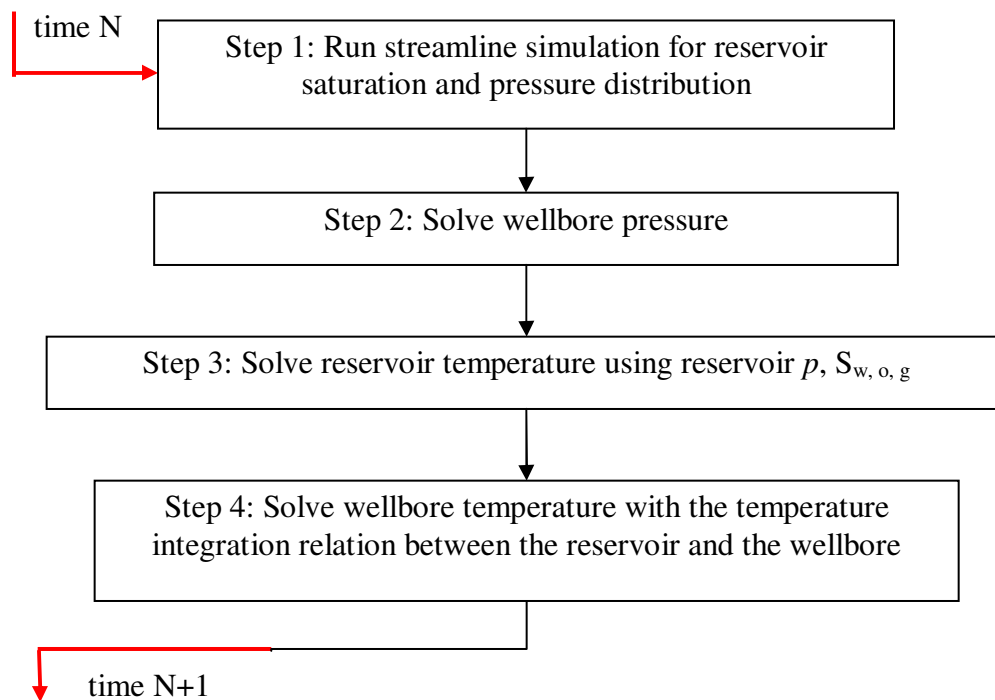
Fig. 2.4 Calculation procedure of forward model

At each time step for a transient problem, the model first calculates reservoir pressure and saturation. Then the wellbore pressure is solved. After that, use the pressure and saturation to solve the reservoir temperature. The temperature in source term, Eq. 2.36, will be explicitly calculated by using the information of the previous time step. With known reservoir pressure, saturation, and temperature fields, we solve the wellbore

temperature equation with the integrated temperature relation, Eq. 2.49. Thus, we can get a wellbore temperature distribution and move to next time step.

Before applying the model, we need to validate it. We compare the result of the new approach with an analytical solution. Yoshioka et al. (2005) derived an analytical solution for reservoir temperature distribution, where the reservoir and flow geometry are shown in Fig. 2.5. In his model, both flow and temperature in reservoir are steady state; at the external reservoir boundary, pressure is constant, and temperature is constant and equal to the geothermal temperature; heat conduction at z direction is ignored. Based on these assumptions, the reservoir temperature distribution can be analytical solved from the energy balance equation.
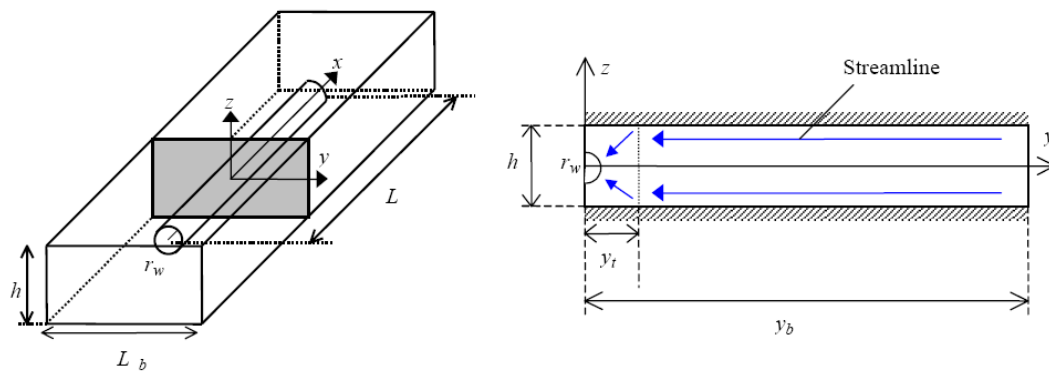
Fig. 2.5 Linear-radial flow geometry (Furui et al., 2003)

To compare with Yoshioka's model, a reservoir and horizontal well system is used. Single phase oil flow and single phase gas flow were compared respectively. The input data are listed in Table 2.1 and Table 2.2. Table 2.1 gives the fluid properties and Table 2.2 gives reservoir parameters used in the program validation.

Table 2.1 Fluid Properties in Program Validation

	Oil	Gas	Water
Density (lb/ft^3)	40	21	63
Viscosity (cp)	0.38	0.0175	0.48
Heat capacity (Btu/lb-^{0}F)	0.524	0.587	1.002
Thermal expansion coefficient $\times 10^4$ (1/^{0}F)	6.74	23.6	3.11
K_{Tt} (Btu/hr-ft-^{0}F)	2	1.3	2.5

Table 2.2 Reservoir Parameters in Program Validation

	Oil Case	Gas Case
Permeability, md	20	1
Reservoir width, ft	2000	2000
Thickness, ft	110	110
Pressure drawdown, psi	170	170
T at outer boundary, ^{0}F	180	180

The comparisons between the new model and the analytical model are shown in Fig. 2.6 and Fig. 2.7. The pressure drawdown for both oil and gas cases are set to the same value, 170 psi, therefore, pressure distributions for oil and gas are the same. The numerical pressure is in accordance with the analytical solution derived from Furui et al. (2003), and the calculated temperature profiles also agree with analytical results. The results validate the new model.
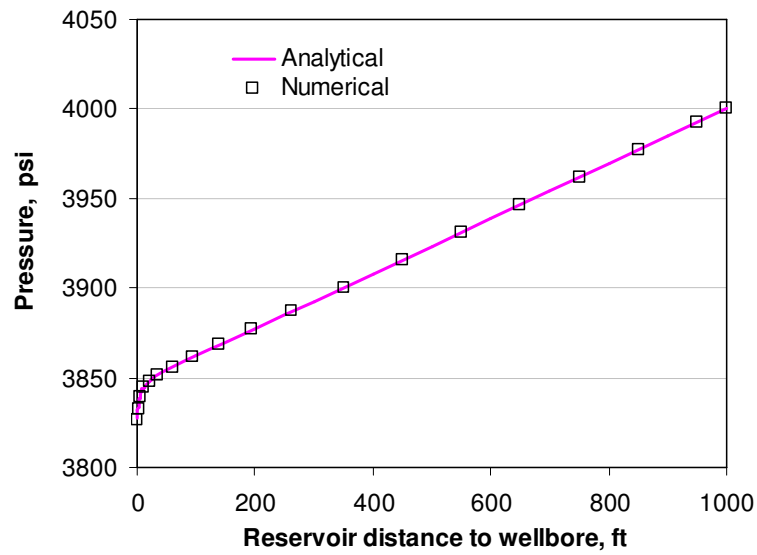
Fig. 2.6 Reservoir pressure distribution
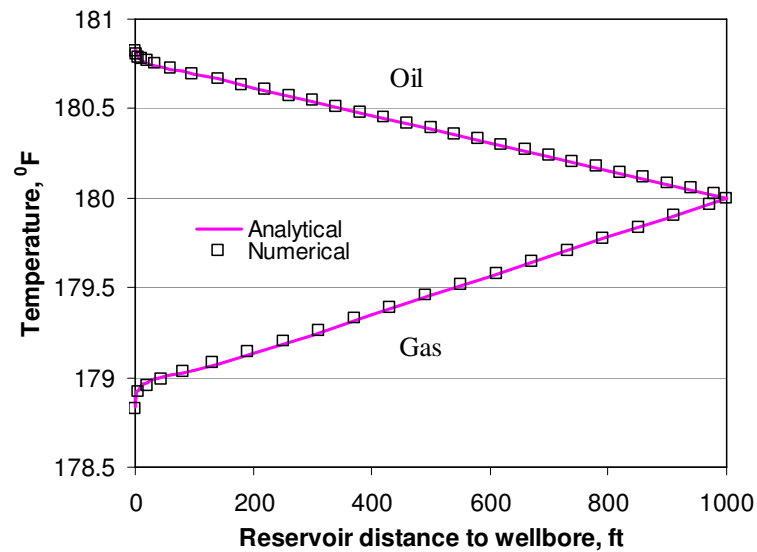
Fig. 2.7 Reservoir temperature distribution

CHAPTER III

INVERSION METHOD

The purpose of this study is to interpret downhole temperature and pressure data to flow conditions, which is an inversion problem. In general, to solve an inversion problem, an objective function is created and minimized. The objective function is a least-square function representing the difference between the observed data and the calculated data. The objective function can be written as:

$$\mathbf{f}(\mathbf{x}) = \frac{1}{2}\|\mathbf{d} - \mathbf{g}(\mathbf{x})\|^2 = \frac{1}{2}(\mathbf{d} - \mathbf{g}(\mathbf{x}))^T \mathbf{C}_m^{-1}(\mathbf{d} - \mathbf{g}(\mathbf{x})) \dots\dots\dots (3.1)$$

where $\mathbf{x}$ denotes the parameter, $\mathbf{d}$ is the observed data, and $\mathbf{g(x)}$ is the calculation result from the forward model, and $\mathbf{C}$ is the covariance matrix, which is a diagonal matrix storing the weights of each observed data.

In this work, temperature and pressure are the observed data. Therefore, the objective function is:

$$\mathbf{f}(\mathbf{x}) = D_T \sum_{j=1}^{j_1}\left(T^{cal} - T^{obs}\right)_j^2 + D_p \sum_{j=1}^{j_2}\left(p^{cal} - p^{obs}\right)_j^2 \dots\dots\dots (3.2)$$

where D_T and D_p represent the weights of temperature and pressure, j_1 and j_2 are the number of observed temperature and pressure data respectively. And the fraction 1/2 can be accounted into the weights, D_T and D_p.

Because temperature and pressure have different units, this difference in value of pressure and temperature can be adjusted to close to each one by the weights. When

temperature and pressure effects on the objective function are at the same level, and

$j_1 = j_2$, the relation of their weights can be approximated by (Yoshioka, 2007)

$$D_T = (1/K_{JT})^2 D_p = (\rho C_p / (\beta T - 1))^2 D_p \quad \text{.. (3.3)}$$

For example, for a single-phase oil reservoir, if the pressure weight D_p is set to 1, the

temperature weight D_T is about 6×10^{12} in SI unit. The weights will effect on the value

of the objective function, which may have influence on the convergence of inversion

with certain criteria. Therefore, it should be chosen carefully.

The forward model described before can help to understand the relation

between temperature behavior and fluid flow rate. We find that temperature feature

along a wellbore can identify sections with different inflow rates. If neglecting other

issues (this may cause error), the rate difference is a reflection of permeability

difference. With this assumption, we can choose reservoir permeability k as the

parameter $\mathbf{x}$ in the objective function.

Thus, we can apply inversion methods to minimize the objective function by

updating reservoir permeability k. Because the horizontal well temperature can be

obtained from the forward model for a given condition, when the temperature calculated

from the forward model agrees with the observed data. The objective function reaches a

minimum, and we conclude that the wellbore flow profile is identified under these

conditions.

Inversion methods can be either gradient based methods or stochastic based

methods. Generally, gradient based method is fast, but it may be stuck in local

minimum. Stochastic method can avoid local minimum problem because it search the solution in global parameter space. However, when parameter numbers are large, the computation is time consuming. In this study, we apply a standard gradient based method, the Levenberg-Marquardt (L-M) method (Sui et al., 2008a; Yoshioka et al., 2007a), and a stochastic method, the traditional Markov chain Monte Carlo (MCMC) method (Ma et al., 2008) to the inversion problem. Both of these two methods can successfully minimize the objective function.

3.1 LEVENBERG-MARQUARDT METHOD

Define the error or residual vector, $\mathbf{e}$, between observation $\mathbf{d}$ and model calculation $\mathbf{g}(\mathbf{x})$ as

$$\mathbf{e} = \mathbf{C}_m^{-1/2}(\mathbf{d} - \mathbf{g}(\mathbf{x})) \quad\text{.. (3.4)}$$

Then the objective function can be simplified as

$$\mathbf{f}(\mathbf{x}) = \frac{1}{2}\mathbf{e}^T\mathbf{e} \quad\text{... (3.5)}$$

For gradient based method, the objective function is minimized by updating the parameter vector $\mathbf{x}$ by adding a gradient-relative term at each step:

$$\mathbf{x}_{n+1} = \mathbf{x}_n + \delta\mathbf{x}_n \quad\text{... (3.6)}$$

The update rule for Levenberg-Marquardt method is:

$$\delta\mathbf{x}_n = -(\mathbf{H} + \lambda\mathbf{I})^{-1}\mathbf{w} = -(\mathbf{J}^T\mathbf{J} + \lambda\mathbf{I})^{-1}\mathbf{J}^T\mathbf{e} \quad\text{.. (3.7)}$$

where $\mathbf{w}$ is the gradient of $\mathbf{f}(\mathbf{x})$,

$$\mathbf{w} = \nabla \mathbf{f}(\mathbf{x}) = \mathbf{J}^T \mathbf{e} \quad\text{.. (3.8)}$$

$\mathbf{J}$ is the Jacobin matrix of vector $\mathbf{e}$,

$$\mathbf{J} = \nabla \mathbf{e} = \begin{bmatrix} \dfrac{\partial e_1}{\partial x_1} & \dfrac{\partial e_1}{\partial x_2} & \cdots & \dfrac{\partial e_1}{\partial x_n} \\ \dfrac{\partial e_2}{\partial x_1} & \dfrac{\partial e_2}{\partial x_2} & \cdots & \dfrac{\partial e_2}{\partial x_n} \\ \vdots & \vdots & \vdots & \vdots \\ \dfrac{\partial e_m}{\partial x_1} & \dfrac{\partial e_m}{\partial x_2} & \cdots & \dfrac{\partial e_m}{\partial x_n} \end{bmatrix} \quad\text{... (3.9)}$$

and $\mathbf{H}$ is the Hessian matrix of $\mathbf{f}(\mathbf{x})$:

$$\mathbf{H} = \mathbf{J}^T \mathbf{J} + \sum_{j=1}^{m} e_j \nabla^2 e_j \quad\text{.. (3.10)}$$

If the error or residual e_j is small, or $\nabla^2 e_j$ is small, $\mathbf{H}$ can be approximated as

$$\mathbf{H} = \mathbf{J}^T \mathbf{J} \quad\text{.. (3.11)}$$

The Jacobin matrix $\mathbf{J}$ can be obtained by

$$\mathbf{J} = \nabla \mathbf{e} = \nabla \left[\mathbf{C}_m^{-1/2} (\mathbf{d} - \mathbf{g}(\mathbf{x})) \right] = -\mathbf{C}_m^{-1/2} \cdot \nabla \mathbf{g}(\mathbf{x}) = -\mathbf{C}_m^{-1/2} \cdot \mathbf{G} \quad\text{.................................. (3.12)}$$

where $\mathbf{G}$ is the sensitivity matrix of forward model $\mathbf{g}$. So, it can be calculate from forward model by giving a small perturbation of $\mathbf{x}$. Permeability k is served as the parameter, the sensitivity calculation is:

$$\mathbf{G} = \nabla \mathbf{g}(\mathbf{x}) = \begin{bmatrix} \dfrac{\partial T_1}{\partial k_1} & \dfrac{\partial T_1}{\partial k_2} & \cdots & \dfrac{\partial T_1}{\partial k_n} \\ \vdots & \vdots & \vdots & \vdots \\ \dfrac{\partial T_{j1}}{\partial k_1} & \dfrac{\partial T_{j1}}{\partial k_2} & \cdots & \dfrac{\partial T_{j1}}{\partial k_n} \\ \dfrac{\partial p_1}{\partial k_1} & \dfrac{\partial p_1}{\partial k_2} & \cdots & \dfrac{\partial p_1}{\partial k_n} \\ \vdots & \vdots & \vdots & \vdots \\ \dfrac{\partial p_{j2}}{\partial k_1} & \dfrac{\partial p_{j2}}{\partial k_2} & \cdots & \dfrac{\partial p_{j2}}{\partial k_n} \end{bmatrix} \qquad (3.13)$$

Therefore, we can calculate the update parameter $\delta\mathbf{x}_n$ by

$$\delta\mathbf{x}_n = -(\mathbf{H} + \lambda\mathbf{I})^{-1}\mathbf{w} = -(\mathbf{G}^T\mathbf{C}_m^{-1}\mathbf{G} + \lambda\mathbf{I})^{-1}\mathbf{G}^T\mathbf{C}_m^{-1}(\mathbf{d} - \mathbf{g}(\mathbf{x})) \qquad (3.14)$$

For example, the lth component of $\mathbf{w}$ is:

$$w_l = \sum_{j=1}^{j1}\left((D_T)_j(T_j^{cal} - T_j^{obs})\frac{\partial T_j^{cal}}{\partial k_l}\right) + \sum_{j=1}^{j2}\left((D_p)_j(p_j^{cal} - p_j^{obs})\frac{\partial p_j^{cal}}{\partial k_l}\right) \qquad (3.15)$$

where temperature and pressure weight at different locations can be set to different values. Generally $(D_T)_j$ and $(D_p)_j$ are set as constant in this work.

The component of $\mathbf{H}$ at i^{th} row and l^{th} column is

$$(\mathbf{H})_{il} = \sum_{j=1}^{j1}\left((D_T)_j\frac{\partial T_j^{cal}}{\partial k_i}\frac{\partial T_j^{cal}}{\partial k_l}\right) + \sum_{j=1}^{j2}\left((D_p)_j\frac{\partial p_j^{cal}}{\partial k_i}\frac{\partial p_j^{cal}}{\partial k_l}\right) \qquad (3.16)$$

The sensitivity is calculated by

$$\frac{\partial T_j^{cal}}{\partial k_i} = \frac{T_j^{cal}(k_1,\cdots,k_i + \delta k_i,\cdots,k_N) - T_j^{cal}(k_1,\cdots,k_i + \delta k,\cdots,k_N)}{\delta k_i} \qquad (3.17)$$

We set the perturbation $\delta k_i \approx 0.05 k_i$. For a system with N parameters, we need calculate the forward model N times to obtain the sensitivity in one update step.

In Eq. 3.14, the optimum value of the damping factor λ will affect the update parameter. We can change λ to 10λ and $\lambda/10$ respectively, and then get three update parameters: $\delta\mathbf{x}(\lambda)$, $\delta\mathbf{x}(10\lambda)$, and $\delta\mathbf{x}(\lambda/10)$. The next step is to calculate the objective function based on these three update parameters, and choose the one with minimum objective function as the best update parameter. The initial λ can be estimated by the average eigenvalue of the Hessian matrix.

Therefore, starting from an initial guess $\mathbf{x}_0$, we can use Eq. 3.14 to calculate the update parameter $\delta\mathbf{x}$ iteratively. The iteration will stop when the objective function converges by using the following criteria:

$$\mathbf{f}(\mathbf{x}_n) - \mathbf{f}(\mathbf{x}_{n+1}) < \varepsilon_1 \quad\text{...}\quad (3.18)$$

or

$$\frac{\mathbf{f}(\mathbf{x}_n) - \mathbf{f}(\mathbf{x}_{n+1})}{\mathbf{f}(\mathbf{x}_n)} < \varepsilon_2 \quad\text{...}\quad (3.19)$$

where ε_1 and ε_2 are relative small residuals. Eq. 3.19 are more useful because ε_2 is dimensionless, and the effect of weights on the objective function is almost cancelled by division. Generally, ε_2 can be 0.001~0.01.

3.2   MARKOV CHAIN MONTE CARLO METHOD

Markov chain Monte Carlo (MCMC) method is generally used in sampling (Ma et al., 2008; Oliver et al., 1997). In this work, we use the traditional Metropolis-Hasting MCMC Algorithm to minimize the objective function. The procedure of this method is following these steps:

1. Guess an initial reservoir permeability distribution k_0.

2. At state n, for a given initial permeability distribution k_n, run the forward model, and get calculated temperature and pressure data.

3. Calculate the objective function $\mathbf{f}(k_n)$.

4. Generate k_{n+1} from a proposal distribution $q_d(k_{n+1} \mid k_n)$. In this work, we use uniform distribution to generate the new permeability.

5. Run forward model, get new pressure and temperature data, and calculate the objective function $\mathbf{f}(k_{n+1})$.

6. Use Metropolis-Hastings algorithm to judge the acceptance of k_{n+1}.

7. If the new permeability is accepted, store the new permeability as the next state and go to step 2, otherwise, go to step 4.

The Metropolis-Hastings (M-H) algorithm is applied in step 6 to decide the acceptance of any new generated permeability, i.e., the proposed permeability distribution, k_{n+1}, is accepted according to the probability:

$$\rho_{prob}(k_n, k_{n+1}) = \min\left(1, \frac{q_d(k_{n+1} \mid k_n) EXP(-\mathbf{f}(k_{n+1}))}{q_d(k_n \mid k_{n+1}) EXP(-\mathbf{f}(k_n))}\right) \quad\text{...................................... (3.20)}$$

After a series of sampling (known as burn-in), we collect samples $k_0, k_1, k_2, \ldots, k_n, k_{n+1}, \ldots$, which are possible solutions to the inverse problem.

The sampler method in step 4 will significantly affect the acceptance of the MCMC method. The independent sampler is a proposal that generates sampler from a uniform distribution without the bound to the current condition. This makes the

inversion process very slow. Therefore, we try to find some other sampler to increase the efficiency.

The random walk sampler is generated by perturbing the current model (Ma et al., 2008). Generally, the random walk sampler has a higher acceptance rate. The random walk sampler first generates a model from uniform distribution, and then uses the current model to constrain the new model:

$$k = k_n + \varepsilon \quad\text{...} (3.21)$$

The small perturbation ε is set about $\pm 0.1 k_n$. If a new model generated form the uniform distribution does not satisfy Eq. 3.21, we reject it and generate a new model until it agrees with the constraint.

Additionally, the generated permeability distribution may be also conditioned by temperature trend or temperature derivative, which can avoid some obvious impossible samples. In the MCMC method, the new model is accepted by using the M-H algorithm in Eq. 3.20. The value of the objective function will influence on the acceptance. Therefore, the value of temperature and pressure weights will affect the result. In this work, the temperature weight, D_T, can be set to 200~2000, and the pressure weight can be estimated by Eq. 3.3.

3.3   FEASIBILITY OF INVERSION OF TEMPERATURE, PRESSURE AND FLOW

A simple synthetic case is used to exam the validation of the inversion program. Fig. 3.1 shows the geometry of this case. Assume the reservoir is separated to two zones, an oil

zone and a water zone. The horizontal well is located at the center of the reservoir, and it is fully penetrated. Table 3.1 is the reservoir input. The reservoir boundaries at y direction are set as constant pressure boundary. Other reservoir boundaries are set as no flow boundary. The initial temperature in reservoir is geothermal distributed temperature.   Table 3.2 lists the fluid and rock properties.
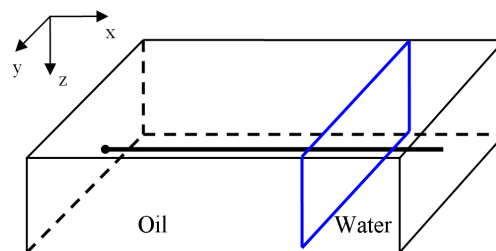
Fig. 3.1 Reservoir geometry information for validation case

Table 3.1 Reservoir and Well Parameters in Program Validation

Reservoir		Wellbore	
Drainage area, ft×ft	3000×2000	Depth of the wellbore, ft	6045
Thickness, ft	90	Length of wellbore, ft	3000
Depth of top, ft	6000	Liquid production rate, bbl/d	10000
Porosity	0.2	Wellbore diameter, ft	0.75
Permeability, k_h ($k_h=10k_v$), md		Wellbore location in y-direction, ft	1000
Oil zone	100		
Water zone	25		
Initial temperature at 6000 ft, ^{0}F	180	Casing diameter, in.	6
Geothermal gradient, ^{0}F/ft	0.01	Casing roughness	0.0005

Table 3.2 Fluid and Rock Properties

	Oil	Water	Rock
Density (lb/ft^3)	50	63	165
Viscosity (cp)	1	0.48	
Heat capacity (Btu/lb-^{0}F)	0.516	1.002	0.22
Thermal expansion coefficient $\times 10^4$ (1/^{0}F)	6.79	3.11	
Total thermal conductivity, K_{Tt} (Btu/hr-ft-^{0}F)		2.0	

Using this input data, the temperature, pressure, and flow rates can be calculated from the forward model. Fig. 3.2 shows the pressure, Fig. 3.3 gives the temperature, and Fig. 3.4 shows the oil and water flow rate distribution. They are referred as observed data, which are marked by triangles in these Figures.

Once the observed data are generated from the forward calculation, the inversion program is applied. Here it adopts MCMC method with random walk sampler. Assume that we already know the locations of oil zone and water zone, the unknown parameters are the permeabilities in the oil zone and the water zone.

Starting from a homogenous initial guess, the inversion program uses 50 md for the entire reservoir permeability. The calculated pressure and temperature at initial condition are different from the observed data. The inverted pressure and temperature which satisfy convergence criteria are marked as lines in Fig. 3.2 and Fig. 3.3. The inverted permeability at matching condition is shown in Fig. 3.5. The corresponding

flow rates of oil and water are close to the observed data, as shown in Fig. 3.4. The results indicate that the inversion program can be used for further study.
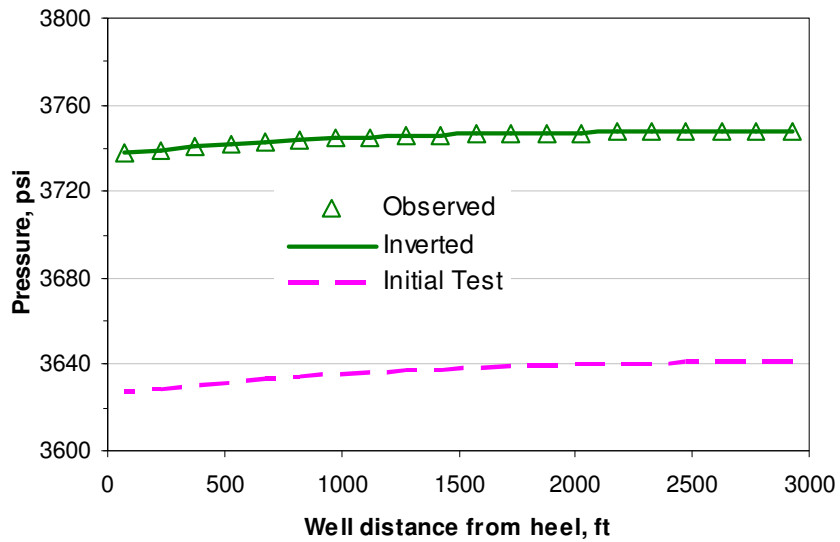
Fig. 3.2 Observed and inverted pressure data at 60 days
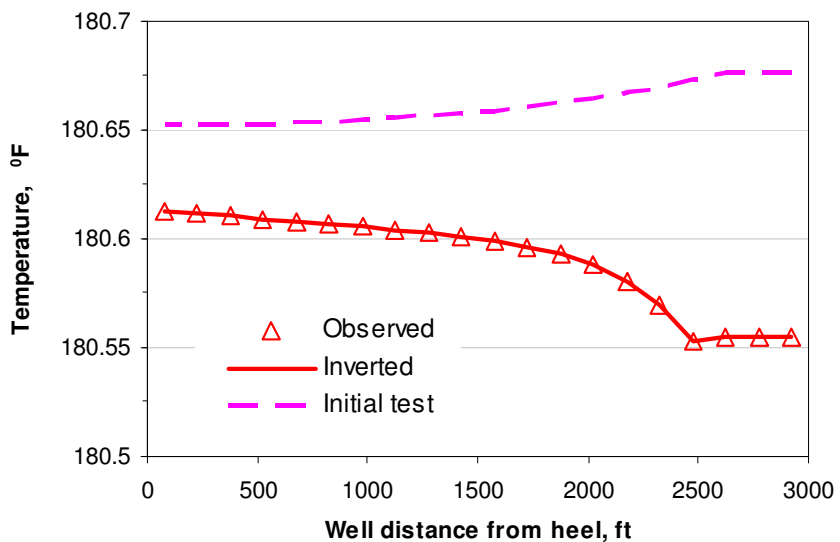
Fig. 3.3 Observed and inverted temperature data at 60 days
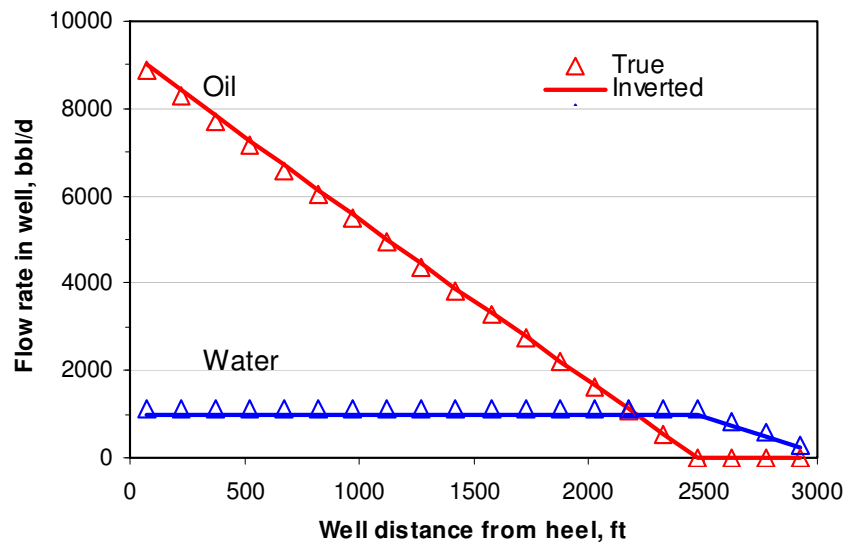
Fig. 3.4 Observed and inverted flow rates of validation case
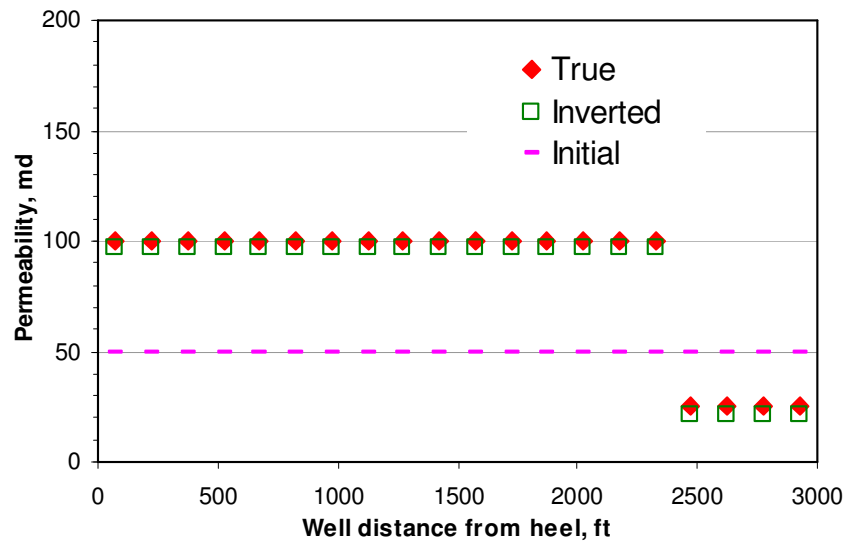
Fig. 3.5 Inverted permeability distribution of validation case

CHAPTER IV

RESULTS OF TEMPERATURE INTERPRETATION MODEL

In this chapter, examples will be used to show how the new model can be applied to the problems at field conditions. We will show the result of forward model first, and then the inversion process. The examples include two cases of water breakthrough diagnosis. The first example is a bottom water driving case, and the second one is a water injection case.

4.1   EXAMPLE 1: BOTTOM WATER DRIVING

The first synthetic example is bottom-aquifer drive case. The example reveals the relation between temperature and flow rate, therefore builds the foundation of the inversion process.

4.1.1   Forward Model Results

One of the biggest problems of bottom-aquifer drive formation is water coning. The problem becomes more severe when reservoir permeability heterogeneity is involved. Fig. 4.1 shows the schematic of the example. The physical model is a rectangular shaped oil reservoir. There is an infinite water support from the bottom aquifer. The horizontal well is located 35 ft from the top boundary of 100-ft payzone (Fig. 4.2b). Fig. 4.2 shows the permeability distribution and relative permeability curve use in this water-oil two-phase flow example. The horizontal permeability is 10 times of the vertical permeability.

The reservoir permeability varies along the wellbore. It has a lower permeability zone (10 md) from 600 to 1200 ft in the x-direction, and a higher permeability zone (500 md) from 1800 to 2100 ft. The rest of the reservoir has a permeability of 50 md.

a. 3D geometry   b. front view geometry
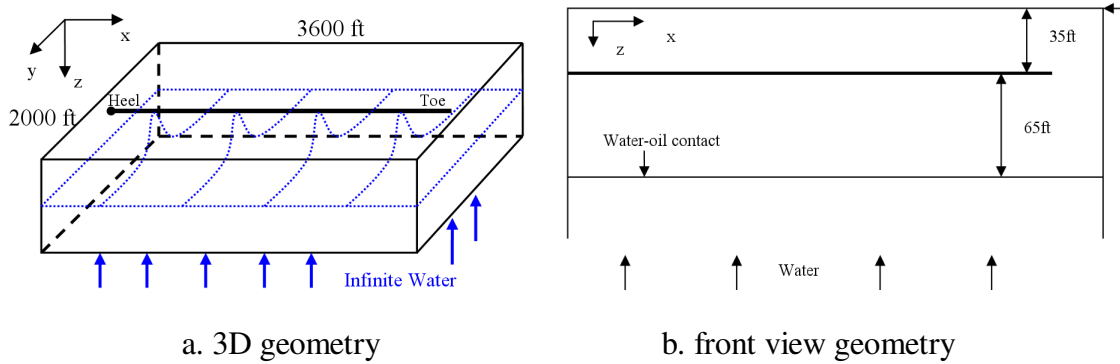
Fig. 4.1 Reservoir geometry information of bottom water driving case

a. grid and permeability distribution   b. relative permeability
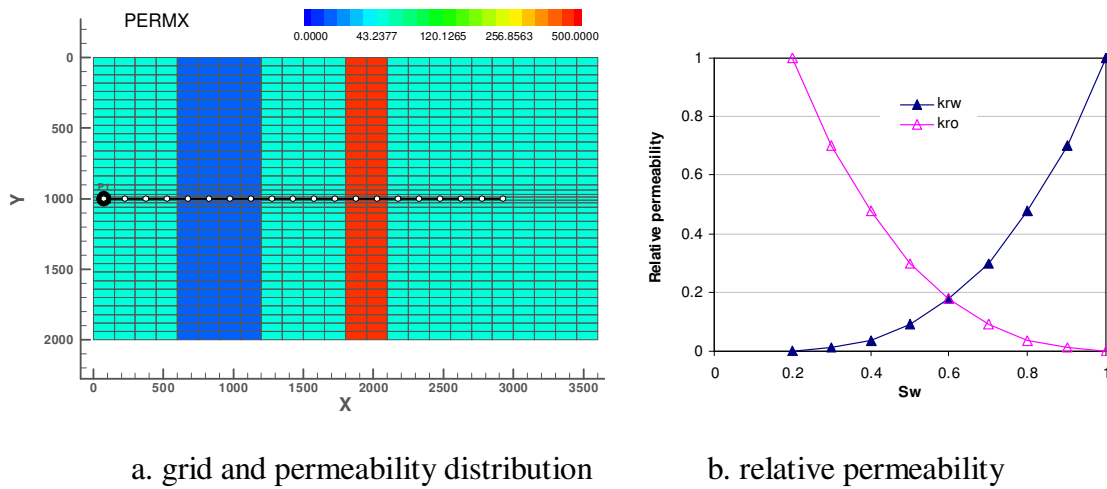
Fig. 4.2 Reservoir permeability distribution and relative permeability curve

Table 4.1 lists the formation and wellbore information, and fluid properties at reference temperature (180 ^{0}F) and pressure (4000 psi) is listed in Table 3.2. The initial temperature at the top surface of the formation is 180 ^{0}F.

Table 4.1 Input for Reservoir and Wellbore of Water Driving Example

Reservoir		Wellbore	
Drainage area, ft×ft	3600×2000	Depth of the wellbore, ft	6035
Thickness, ft	100	Length of wellbore, ft	3000
Depth of top, ft	6000	Liquid production rate, bbl/d	10000
Water oil contact, ft	6100	Wellbore diameter, ft	0.75
Porosity	0.2	Casing diameter, in.	6
Permeability, md	10,50,500	Casing roughness	0.001
Initial temperature at 6000 ft, ^{0}F	180	Wellbore location in y-direction, ft	1000
Geothermal gradient, ^{0}F/ft	0.01		

For the given condition, we use the forward model to predict the oil and water flow rates and the temperature and pressure distributions. Fig. 4.3 through Fig. 4.6 show the calculated results at the wellbore. Fig. 4.3 is the oil inflow rate distribution, Fig. 4.4 is the water inflow rate distribution, Fig. 4.5 is the wellbore temperature, and Fig. 4.6 is the wellbore pressure. Because of the heterogeneity in the permeability field, we observe a non-uniformed temperature along the wellbore, as seen in Fig. 4.5. As production time increase, the anomalous feature on the temperature curve becomes more pronounced. Naturally, when the permeability is high, more fluid with higher temperature enters the

wellbore from the bottom compared with low permeability locations. This higher temperature is also caused by more frictional heating (Joule-Thomson effect) due to the higher flow rate. When water breakthrough into the wellbore, it will contribute a cancelling effect to higher temperature because of the higher heat capacity compared with oil. These features provide us the information to identify the water entry in the inverse model.

The pressure distribution in Fig. 4.6 shows the pressure drop in the well caused by friction. From the toe moving towards the heel, pressure decreases gradually. When passing the high permeability zone, higher flow rate yields higher frictional pressure drop, marking the pressure curve with a visible slope change. However, unlike the temperature curve in Fig. 4.5, this slope changes is too small to be useful quantitative information for flow distribution, and even though we may see the start of the high-perm zone, the end of the high-perm zone is almost undetectable.
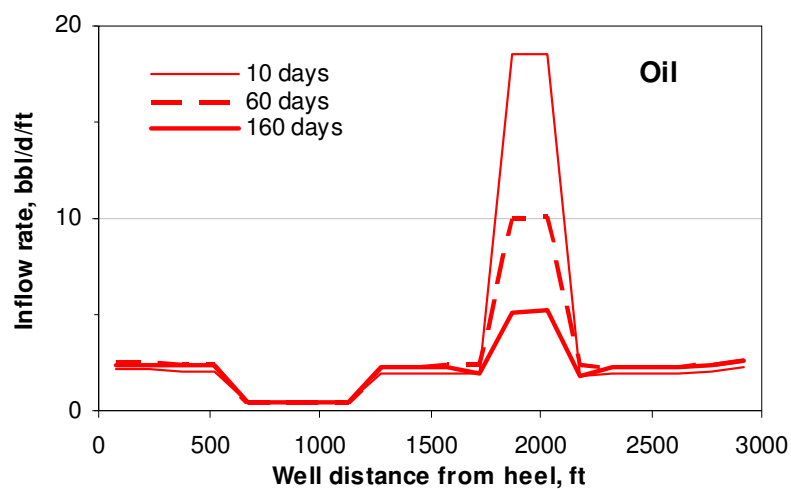
Fig. 4.3 Oil inflow rate distribution
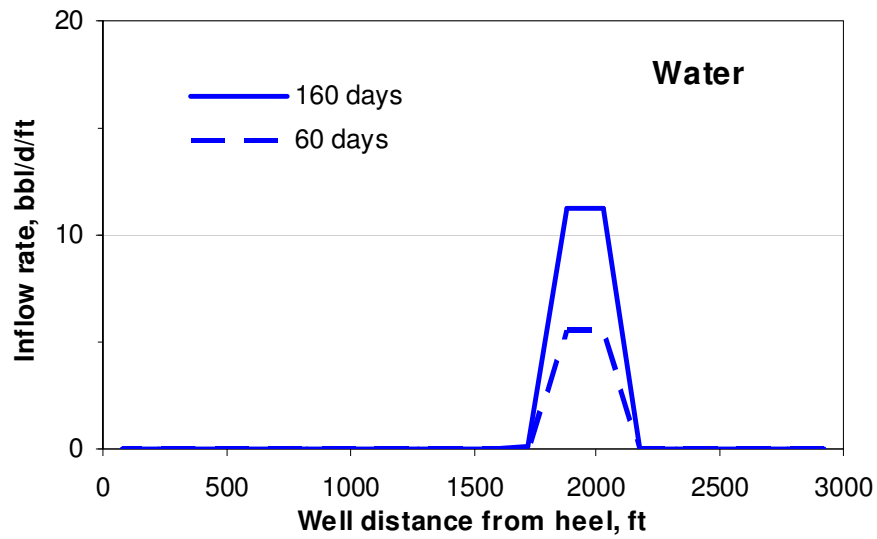
Fig. 4.4 Water inflow rate distribution
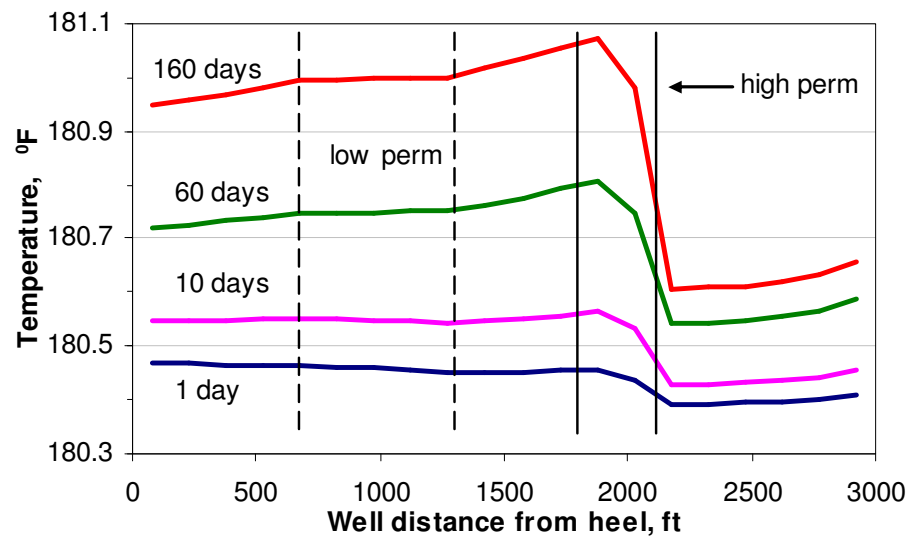
Fig. 4.5 Temperature distribution in wellbore
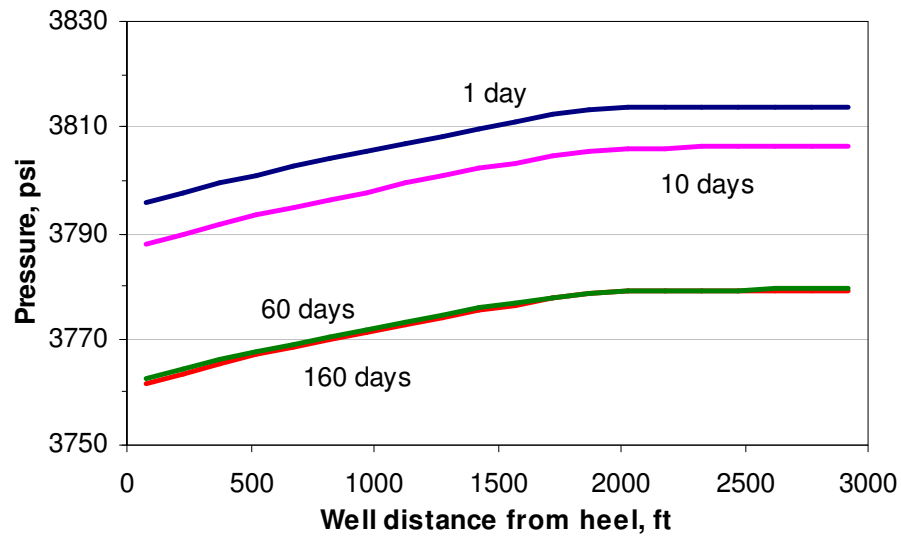
Fig. 4.6 Pressure distribution in wellbore

Although the temperature curve can reflect the high-permeability zone well, it hardly responds to the low-permeability zone (10 md), especially at early time. We calculate the temperature derivative along wellbore, as shown in Fig. 4.7. The positive temperature derivative indicates hotter fluid entries the well, negative temperature derivative means colder fluid comes into the well and their value is related to the flow rate. Temperature derivative can be used to identify the reservoir permeability change.
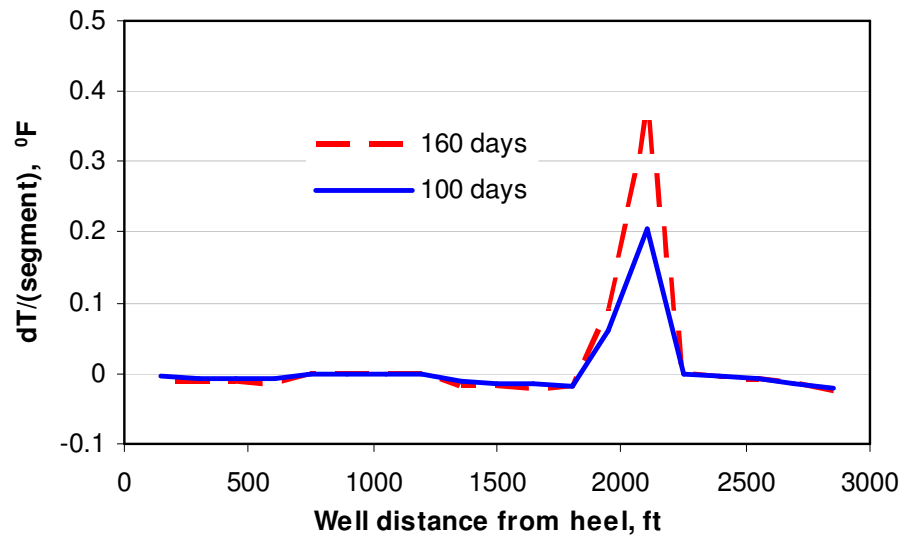
Fig. 4.7 Temperature derivative in wellbore

One advantage of the new model compared with the previous model by Yoshioka et al. (2007b) is that the reservoir temperature, pressure and flow are simulated as a function of time. This transient flow condition provides additional information such as derivatives and helps us to interpret flow profile from temperature and pressure data more accurately. We examine the transient wellbore temperature at two locations, inside the water zone (2025 ft) and outside the water zone (2625 ft) and the water cut as a function of time (shown in Fig. 4.8, temperature as a function of time). The interesting result is that small temperature drop occurs on the temperature curve when water breaks in. The explanation is that the arriving water temperature at this time is lower than the oil temperature because of the difference in heat capacity of these two fluids. Therefore, when the water breaks through, the arriving temperature will decrease. This feature can

help us to locate water breakthrough location and time. Noticed that this temperature

drop is very small, it may require certain sensor resolution to identify the change.
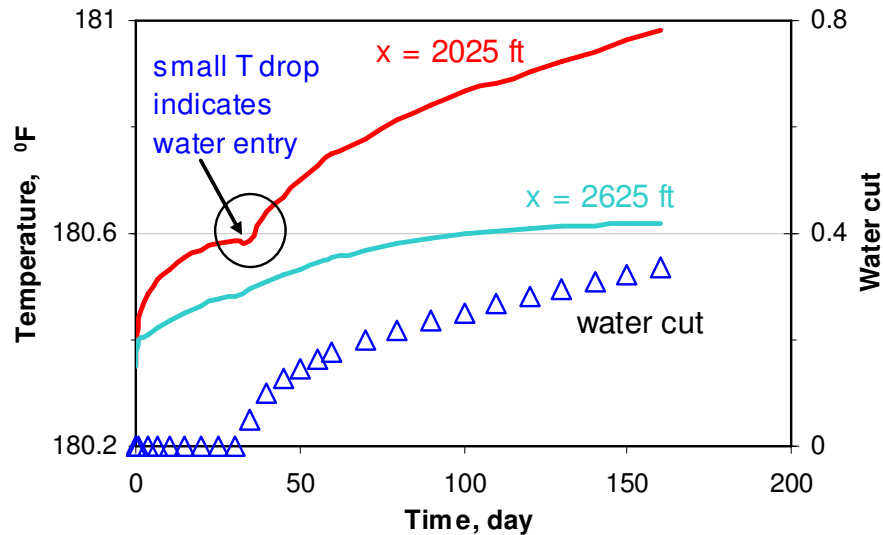
Fig. 4.8 Water cut history and transient temperature at two locations

The transient wellbore temperature distribution as a function of time is shown

in Fig. 4.9, and the transient arriving temperature distribution is shown in Fig. 4.10.

Temperature increases very fast at early time and becomes slower at later time. It is

because that Joule-Thomson effect domains the temperature change at earlier time. One

explanation is that pressure change is significant at early time; as well as the flow near

wellbore is mainly radial, so the temperature change caused by the Joule-Thomson effect

is fastest at early time. At late time, temperature change caused by Joule-Thomson effect

is slower, but the vertical flow will bring hot fluid from the bottom. The range where the

flow rate is higher will have more obvious temperature increase.

Additionally, the transient arriving temperature (Fig. 4.10) can reflect each different permeability range much better than the wellbore temperature. This temperature is the fluid temperature before mixing with fluids in wellbore, so it keeps more original reservoir geology information.
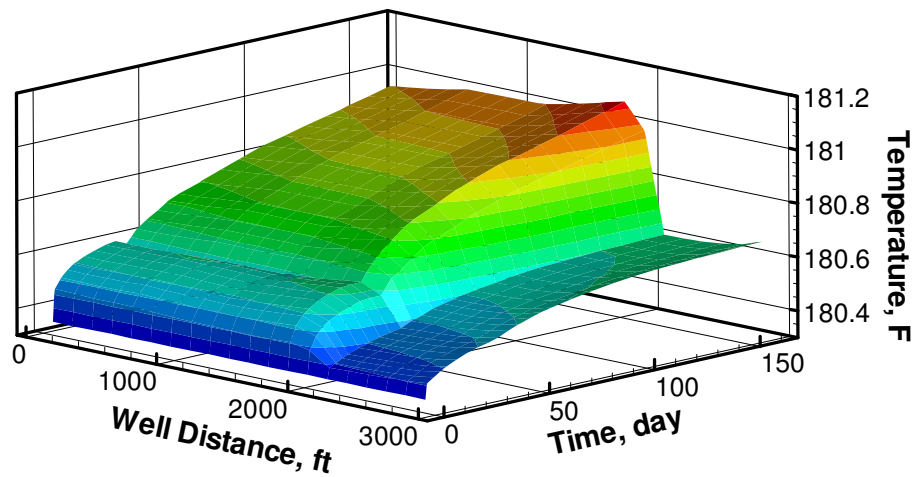
Fig. 4.9 Transient wellbore temperature distribution
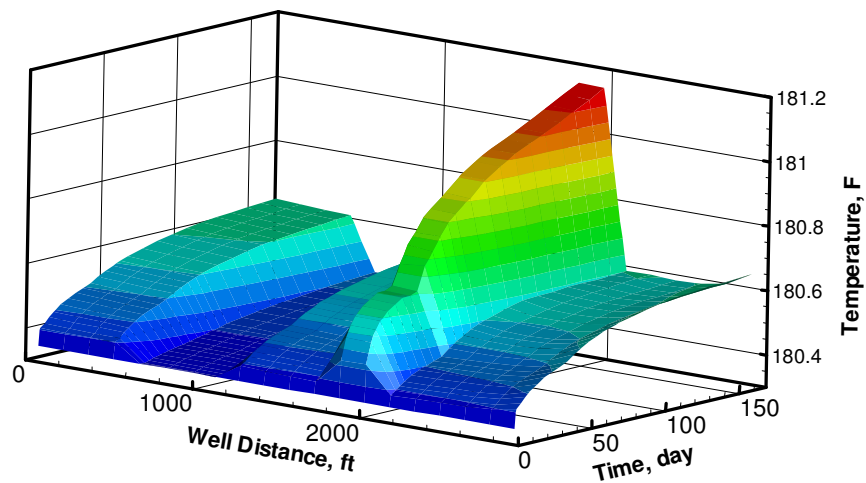
Fig. 4.10 Transient arriving temperature distribution

4.1.2 Inversion Results

Based on the forward model, inversion methods can be applied to interpret downhole measurements, temperature and pressure data, to flow conditions using the same example in the previous section of forward model results. Fig. 4.11 is the top view of the reservoir and wellbore geometry. The forward-model-calculated data presented in Fig. 4.5 will be referred as observed data (corresponding to the measured data in the field). Suppose we have observed temperature and pressure data shown in Fig. 4.5 and Fig. 4.6 from DTS or production logging, and we choose the data at 160 days as the observed data for interpretation. The objective is to interpret the flow profile as shown in Fig. 4.3 and Fig. 4.4 by the inverse model.

To start the process, we analyze the observed temperature data, as marked in Fig. 4.12 as the triangles, where the temperature derivative is also plotted as the solid line. Initially, we assign a uniform permeability of 65 md in the entire reservoir. With this permeability field, we calculate flow rates, wellbore pressure, and temperature by the forward model. With the initial guess, the calculated temperature is plotted against the observed data in Fig. 4.12 as the dashed line. Comparing this calculated temperature and the observed data, we know that the permeability from 2100 to 3000 ft should be close to 65 md, and permeability from 1800 to 2100 ft should be higher than 65 md. The calculated temperature with assumed permeability of 65 md is much lower than the observed temperature, indicating less warm fluid entering the wellbore at this location. The details also can be confirmed by the temperature derivative, which also detects a

slightly low permeability range from 600 to 1200 ft because the slope has smallest absolute value.

Because the wellbore is not fully penetrated in the reservoir for this case, temperature data along the horizontal wellbore is only measured from 0 to 3000 ft. For the unknown permeability from 3000 to 3600 ft, we assume that it is the same as the permeability at the range from 2100 to 3000 ft.

Based on this analysis of the observed temperature data and its derivative, we separate the reservoir to five segments: from 0 to 600 ft is zone 1, 600 to 1200 ft as zone 2, 1200 to 1800 ft as zone 3, 1800 to 2100 ft as zone 4, and 2100 to 3600 ft as zone 5. Each zone has a permeability value as the parameter for inversion. Now we can use either Levenberg-Marquardt (L-M) method or MCMC method to minimize the objective function by finding a satisfied permeability field.
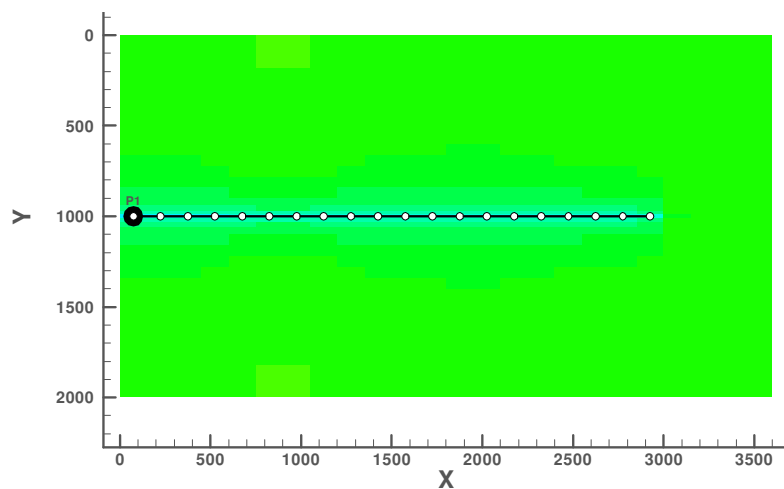
Fig. 4.11 Top view of reservoir and wellbore
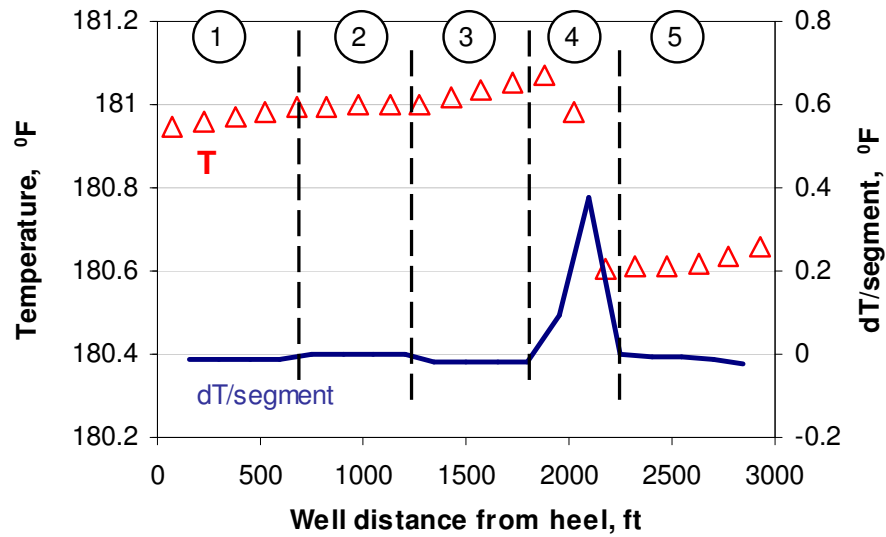
Fig. 4.12 Separate reservoir to sections by temperature data

L-M Method Inverted Results

We use two different permeability distributions as initial guess for the inversion process. One is a homogenous initial guess, which we assign a uniform permeability of 100 md to the entire reservoir, and another one is a 2-value initial guess, which are 200 md from 1800 to 2100 ft and 100 md for other ranges. Fig. 4.13 shows that the objective function decreases vs. iteration number during the inversion process. The objective function at these two initial conditions becomes converged (the objective function approaches a constant) when the program iterates about 30 times. For the homogenous initial guess, the calculated result does not perfectly fit the observed data. But for the 2-value initial, the objective function is close to the zero, which means that calculated result fits the observed data very well. Fig. 4.13 reveals that the inversion result of L-M method is depending on the initial conditions.
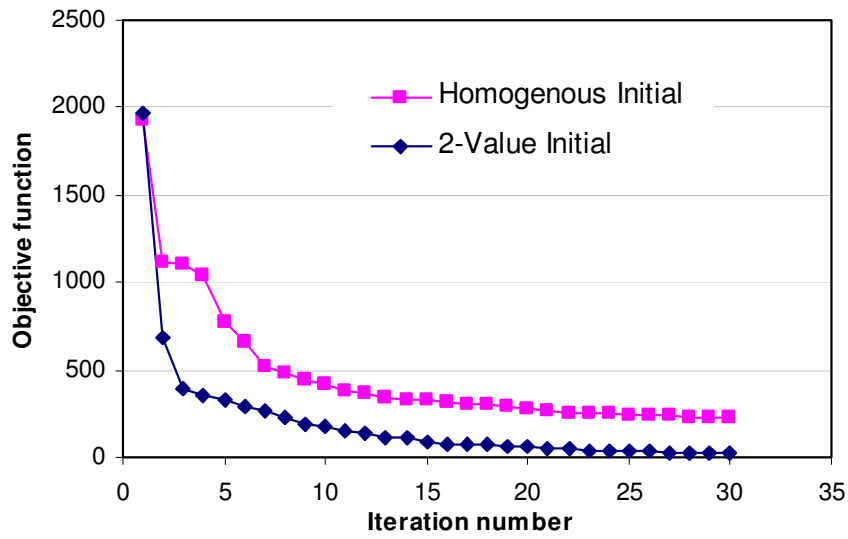
Fig. 4.13 Objective function vs. iteration number at two initial conditions

Homogenous Initial Permeability Result

The inverted result with a uniform permeability of 100 md to the entire reservoir as initial guess for the L-M method is showed in Fig. 4.14 and Fig. 4.15. Fig. 4.14 is the forward-model-calculated temperature (inverted temperature) when the objective function gets convergence. Fig. 4.15 is the inverted pressure. Compared with the temperature calculated from the homogenous initial guess, the inverted temperature is closer to the observed data. It follows the trend of the observed data, although there is a certain error at the sections from 0 to 2000 ft.

However, compared with the initial guess, the inverted pressure does not converge to the observed data even when the objective function converges. This difference is the reason that objective function is still big.
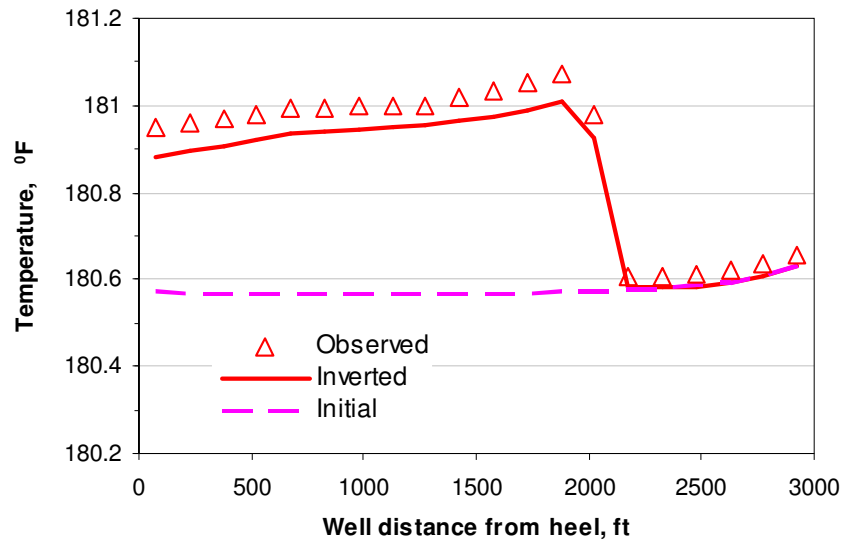
Fig. 4.14 Matched temperature data from L-M method, homogenous initial
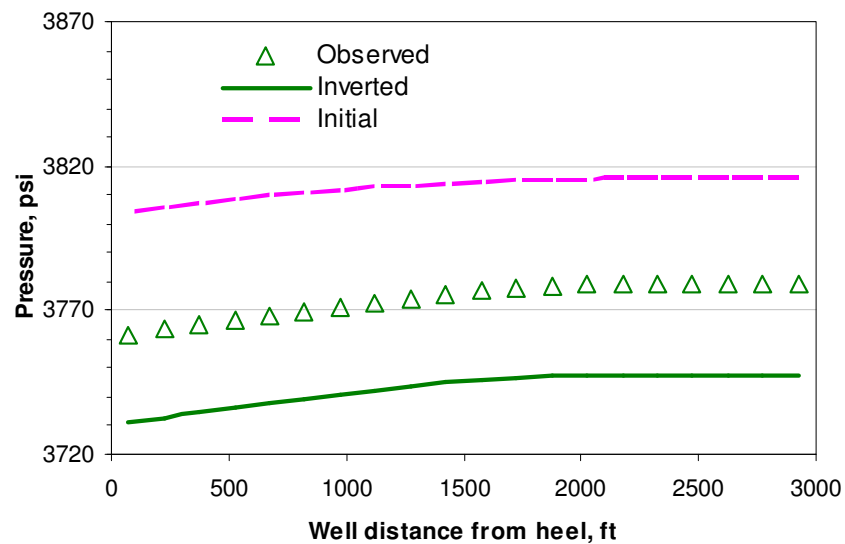
Fig. 4.15 Matched pressure data from L-M method, homogenous initial

Once the inversion process stops, it means that the program finds a permeability distribution which makes the objective function achieved a minimum, i.e., the forward-

model-calculated temperature and pressure at this permeability distribution match the observed data. We plot the inverted flow rate profiles of oil and water at this condition in Fig. 4.16, and the inverted permeability distribution is shown in Fig. 4.17. The inverted oil rate profile is acceptable, but the water rate profiles have a certain error, and the water entry location is not correct. The inverted result requires improvement because the objective function is still a significant number.
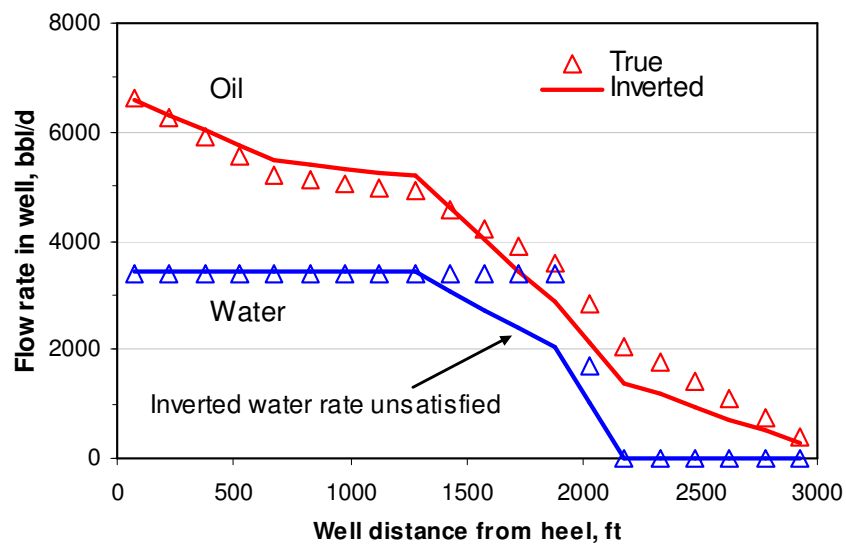
Fig. 4.16 Inverted oil and water flow rate profiles from L-M method, homogenous initial
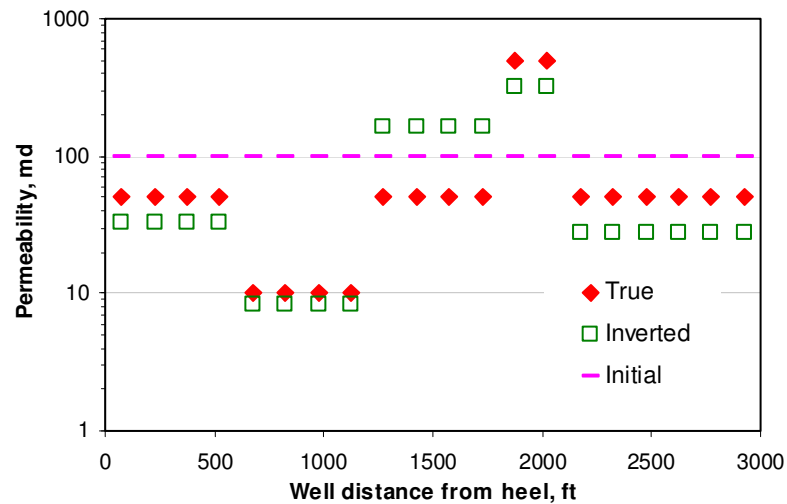
Fig. 4.17 Inverted permeability distribution from L-M method, homogenous initial

2-Value Initial Permeability Result

The inverted result when we assign 2 permeability values along the wellbore to the reservoir as initial guess is shown in Fig. 4.18 and Fig. 4.19. The permeability distribution is that 200 md from 1800 to 2100 ft and 100 md for other ranges. Fig. 4.18 is the forward-model-calculated temperature when the objective function gets converged, and Fig. 4.19 is the calculated pressure. The most obvious improvement is that the pressure data matching is better than the result in Fig. 4.15. The objective function at this initial condition becomes a small number after the iteration of the inversion process, which means the calculated temperature and pressure match the observation very well.
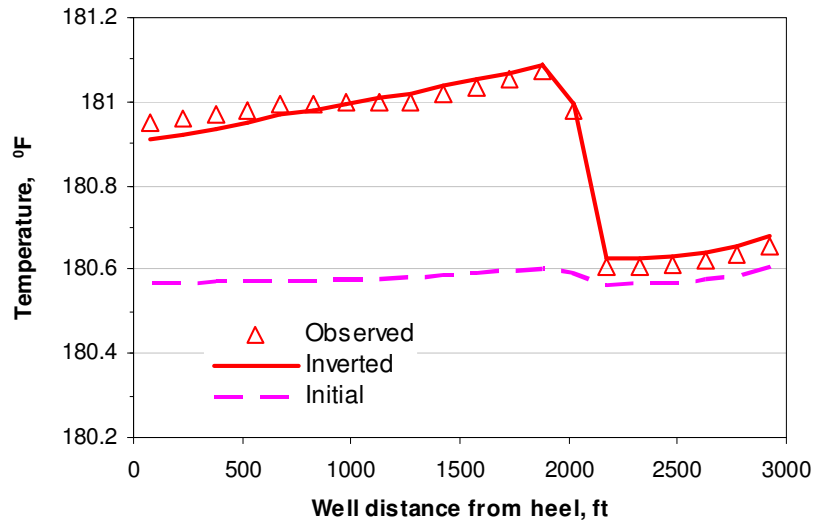
Fig. 4.18 Matched temperature data from L-M method, 2-vlue initial
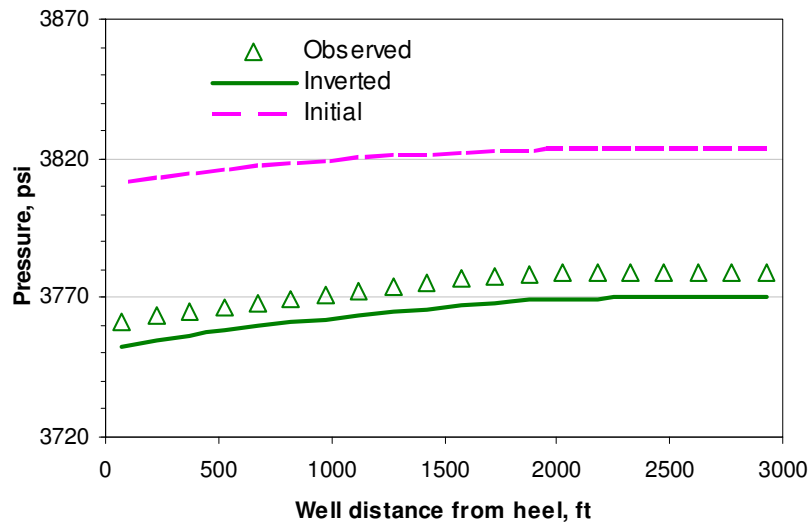
Fig. 4.19 Matched pressure data from L-M method, 2-vlue initial

At this condition that temperature and pressure matched the observation, the inverted oil and water flow rate profiles are showed in Fig. 4.20. Compared with the

result in Fig. 4.16, this result is improved, and the water entry location is found correctly. Fig. 4.21 shows the inverted permeability distribution which is very close to the true data at zone 1 (0 to 500 ft), zone 4 (1800 to 2100 ft), and zone 5 (2100 to 3600 ft). Because these sections dominate the reservoir flowing, the error at other sections becomes small and it is acceptable.
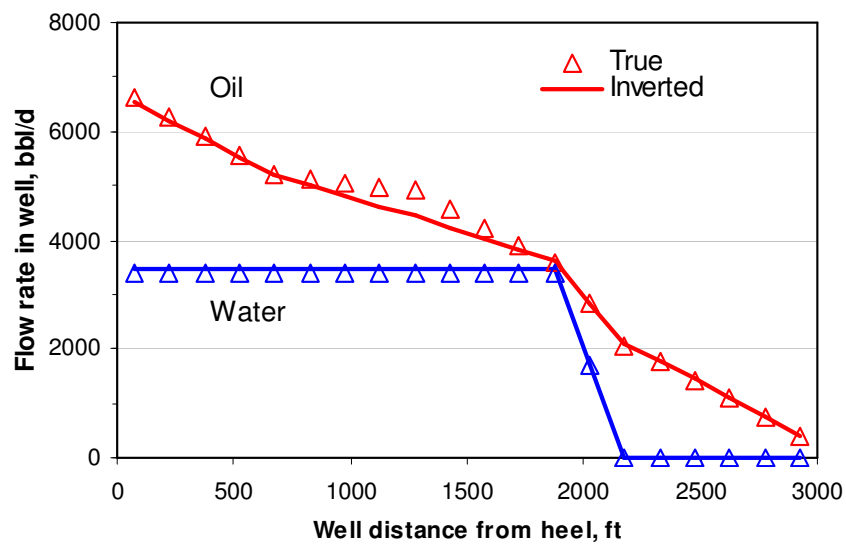
Fig. 4.20 Inverted oil and water flow rate profiles from L-M method, 2-vlue initial
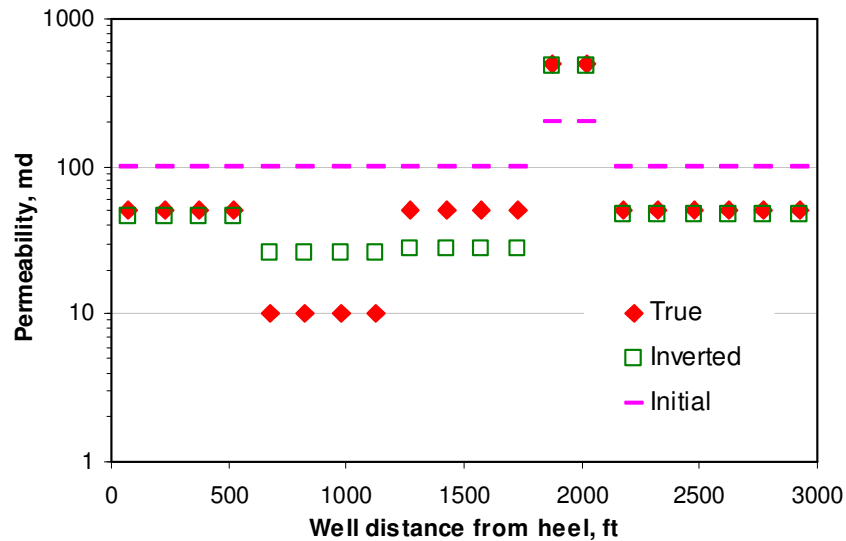
Fig. 4.21 Inverted permeability distribution from L-M method, 2-vlue initial

MCMC Inverted Results

In this section, we use MCMC to minimize the objective function. According to the previous analysis of the temperature data, the reservoir is separated to five segments: zone 1 to zone 5. The permeability in each zone is the unknown parameter which needs to be determined from inversion.

For the MCMC method, we will randomly search the permeability in the global space. However, because we already diagnose that the range from 1800 to 2100 ft has obviously higher permeability, the searching range can be conditioned. In this work, we search the permeability from 100 to 1000 md for the high permeability range (1800 to 2100 ft) and 10 to 100 md for all other zones. Because the low permeability section (600 to 1200 ft) is detected, the program will reject any permeability generated here with higher value, which increases the efficiency of convergence.

The convergence of objective function using MCMC method is shown in Fig. 4.22. We only plot the accepted number during the inversion problem. The independent sampler, which independently generates k_{n+1}, has very low acceptance, and it is time consuming. The random walk sampler, which is constrained by current model in Eq. 3.21, has higher acceptance, and it gets satisfied result faster.
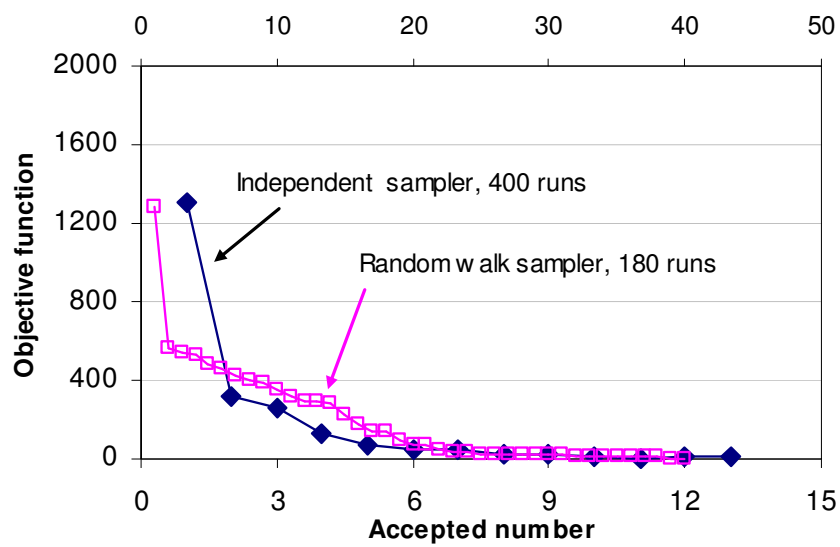
Fig. 4.22 Objective function converges

At the convergence condition, Fig. 4.23 and Fig. 4.24 show that the inverted temperature and pressure match well with the observed data, implying that flow conditions are close to the true conditions.
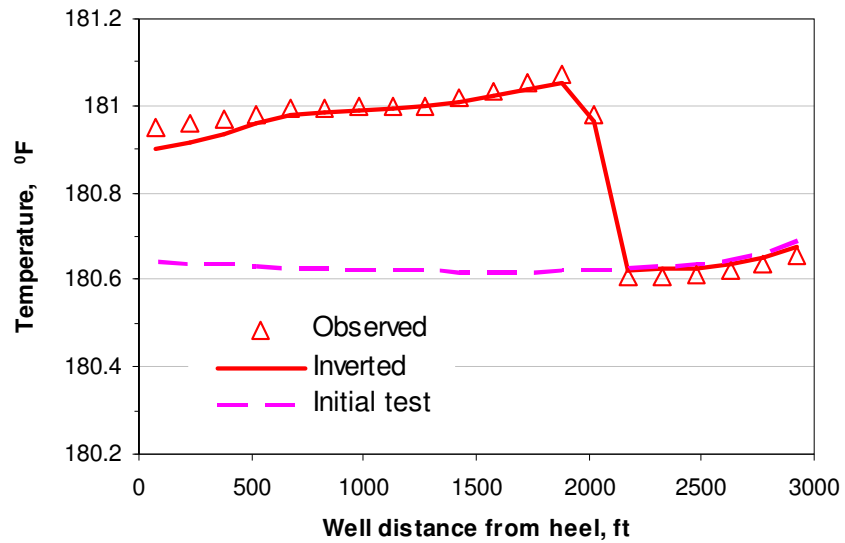
Fig. 4.23 Matched temperature data from MCMC method
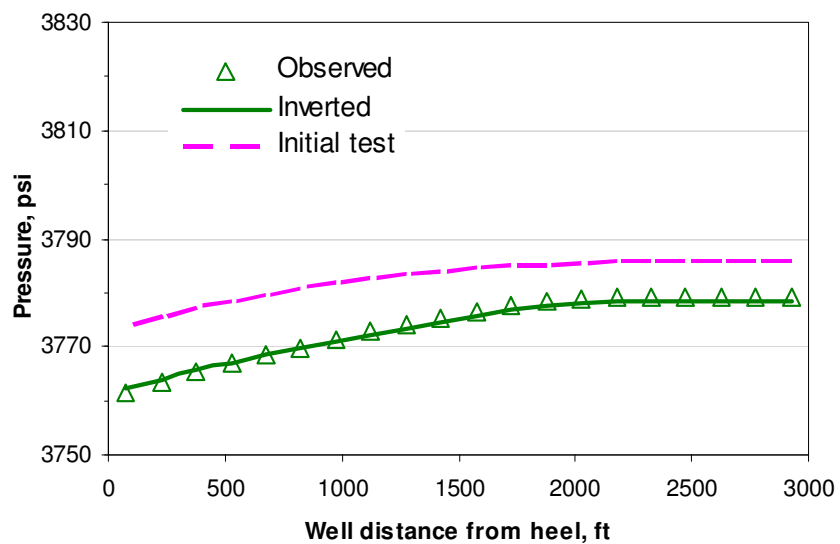
Fig. 4.24 Matched pressure data from MCMC method

As the result, we plot inverted flow profiles in Fig. 4.25 and inverted permeability distribution in Fig. 4.26. Inverted flow profiles are acceptable. It identifies

the water entry location correctly, and estimates closely the amount of water produced at the location. The inverted permeability matches the high permeability section very well. Because this is the major inflow section, the inverted flow rates match well with the observation.

The MCMC method with independent sampler has a fixed run number and has a slow convergence speed and low acceptance ratio (13 acceptances in 400 runs). The random walk sampler has a much higher acceptance ratio (39 acceptances in 180 runs). This stochastic method has the advantages that it does not depend on the initial guess and it can avoid the local minimum problem. However, the sampler size could be higher necessary. Simulation cannot stop before finishing sample the whole population.
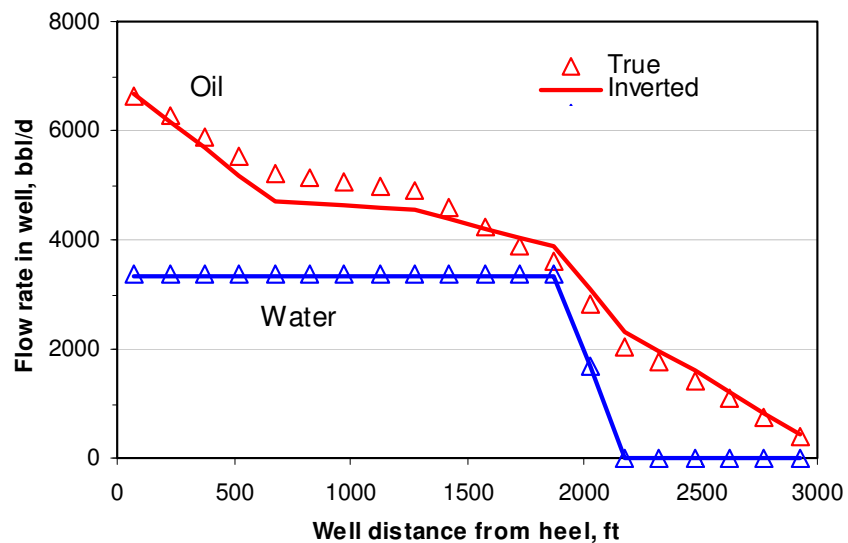
Fig. 4.25 Inverted oil and water flow rate profiles from MCMC method
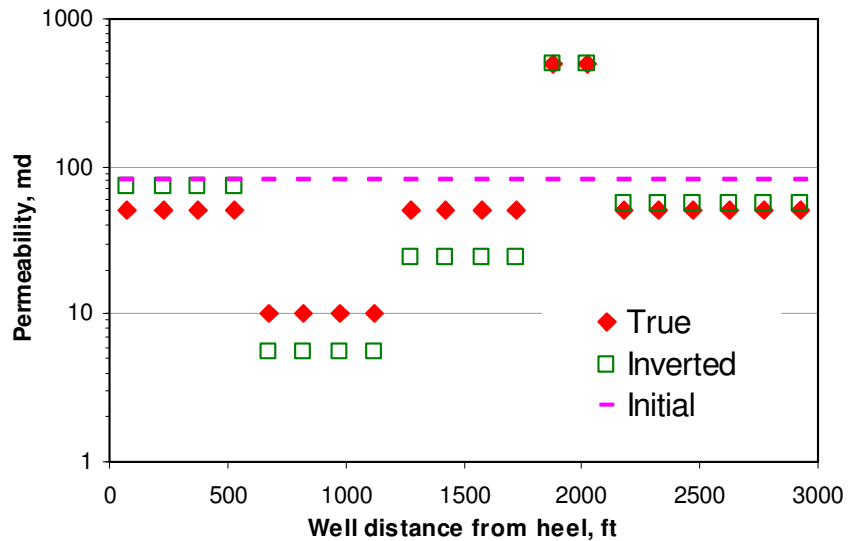
Fig. 4.26 Inverted permeability distribution from MCMC method

The gradient based method, the Levenberg-Marquart (L-M) method, depends on the initial condition and might be stuck in the local minimum. According to our test on this synthetic example, with a good initial guess, the L-M method has a quicker converging speed than MCMC method. But at some initial situations, it cannot obtain a satisfied result.

Either L-M method or MCMC method can be used. In this study, MCMC method is used for the following synthetic cases and field applications.

4.2   EXAMPLE 2: WATER INJECTION

Temperature data can also be used to identify water entry in water flooding cases. This example is applied to a 2D permeability field to illustrate that the inversion procedure can be used in the complex permeability situations.

4.2.1 Forward Model Results

For a water-injection system, Fig. 4.27 shows the reservoir geometry and the well locations. The reservoir has a horizontal injection well and a horizontal producing well. They are parallel and locate at the middle of the pay zone in vertical direction.

Table 4.2 gives the reservoir and production well information. The injection well has a constant bottomhole pressure, 4000 psi, locates at 1995 ft in the y direction, and the pressure drop in injection well is ignored. The injected water has a constant temperature of 100 ^{0}F. Temperature effect on pressure and saturation solution is neglected. The 2D permeability distribution for this case is shown in Fig. 4.28.
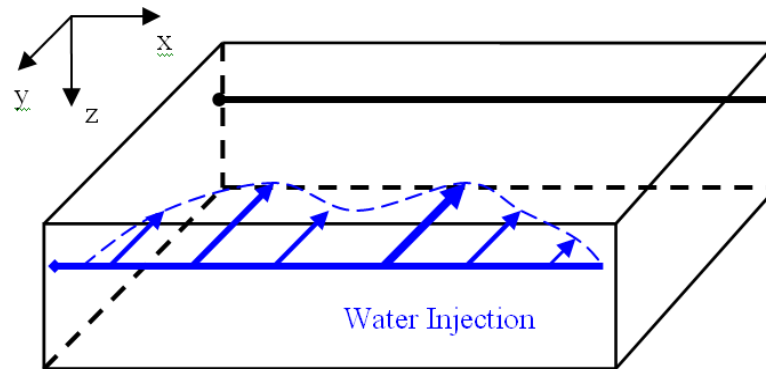
Fig. 4.27 Reservoir geometry and well locations
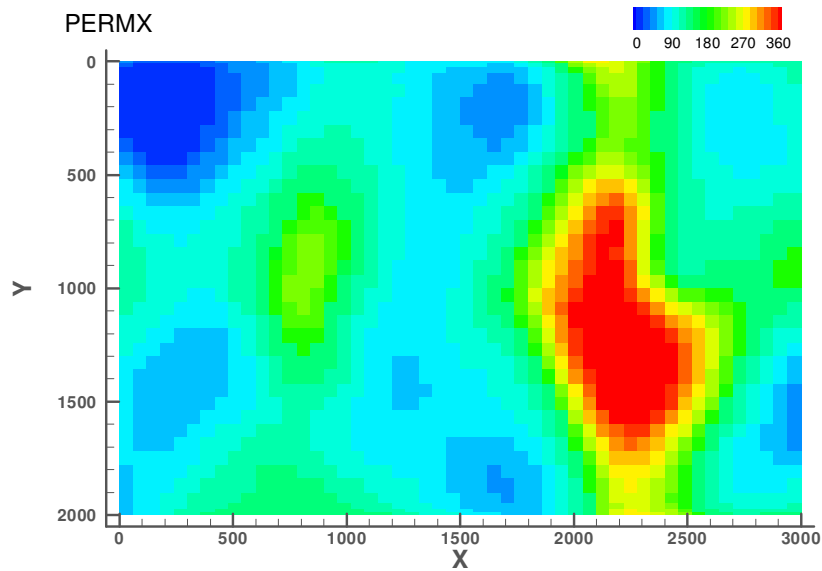
Fig. 4.28 2D permeability distribution

Table 4.2 Input for Reservoir and Wellbore of Water Injection Example

Reservoir		Production Wellbore	
Drainage area, ft×ft	3000×2000	Depth of the wellbore, ft	6025
Thickness, ft	50	Length of wellbore, ft	3000
Depth of top, ft	6000	Liquid production rate, bbl/d	6000
Porosity	0.2	Wellbore diameter, ft	0.75
Initial temperature at 6000 ft, ^{0}F	180	Casing roughness	0.001
Geothermal gradient, ^{0}F/ft	0.01	Casing diameter, in.	4.5

The oil flow rate profiles at 300, 600 and 900 days are shown in Fig. 4.29, and the water flow rate profiles are shown in Fig. 4.30. The 2D heterogeneous permeability causes a non-linear flow rate distribution in the wellbore.
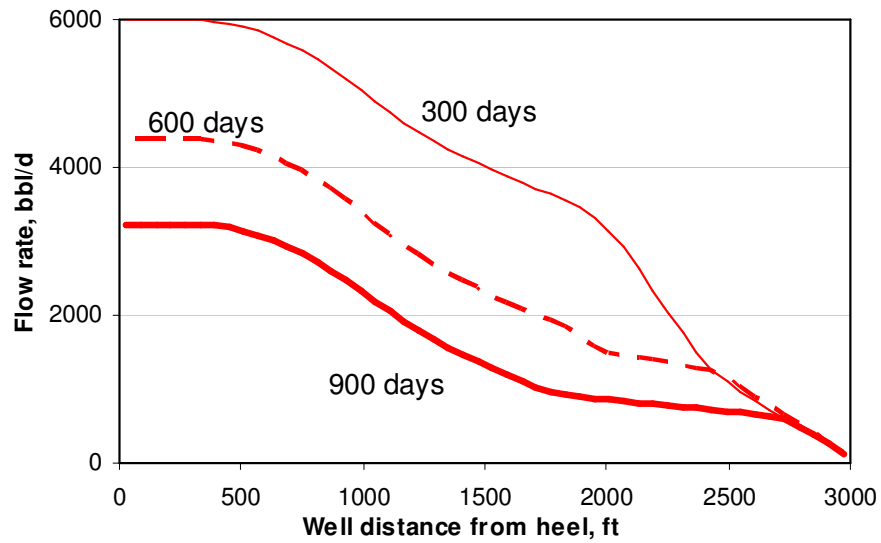
Fig. 4.29 Oil flow rate profiles in tubing
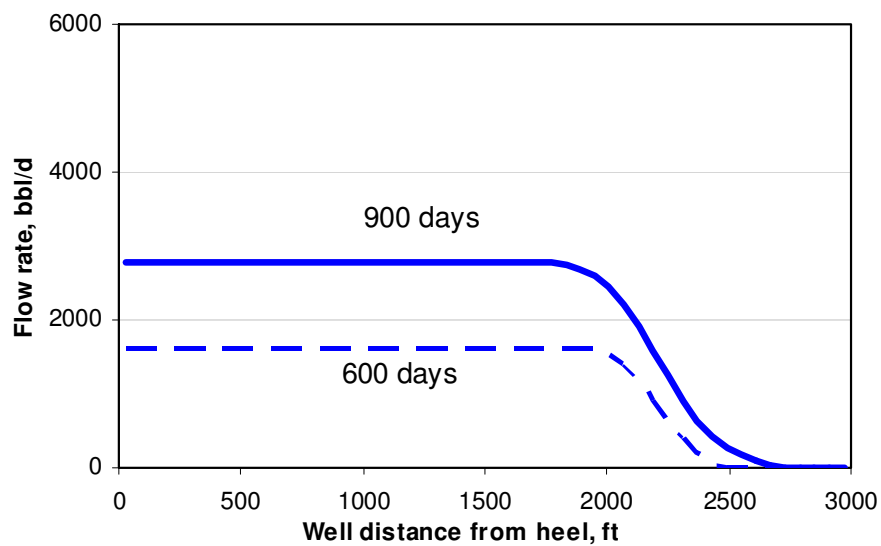
Fig. 4.30 Water flow rate profiles in tubing

The wellbore temperature distribution is shown in Fig. 4.31, and the wellbore pressure distribution is shown in Fig. 4.32. The temperature curves still have the increase

range which can identify the high inflow rate section. However, because the permeability distribution in this case has smooth transition between high permeability and low permeability sections, the temperature curve also becomes smoother compared with the result of Example 1 in Fig. 4.5.

For pressure curves, because the inflow rate at high permeability section is lower than the one of Example 1, the visible slope change of pressure curves is diminished. It is more difficult to use pressure curves to detect the start of the high permeability section.

Although the injected water is 100 ^{0}F and water break-through happens before 600 days, we do not observe a significant temperature decrease caused by the cold injected water at 600 or 900 days. This is because we assume the fluids and the formation have the same temperature in each time step. The initial temperature of the formation is 180 ^{0}F. The injected water will be heated when it flows through the reservoir. If we keep the simulation for a long production time, we can observe this temperature decrease caused by the cold injected water.
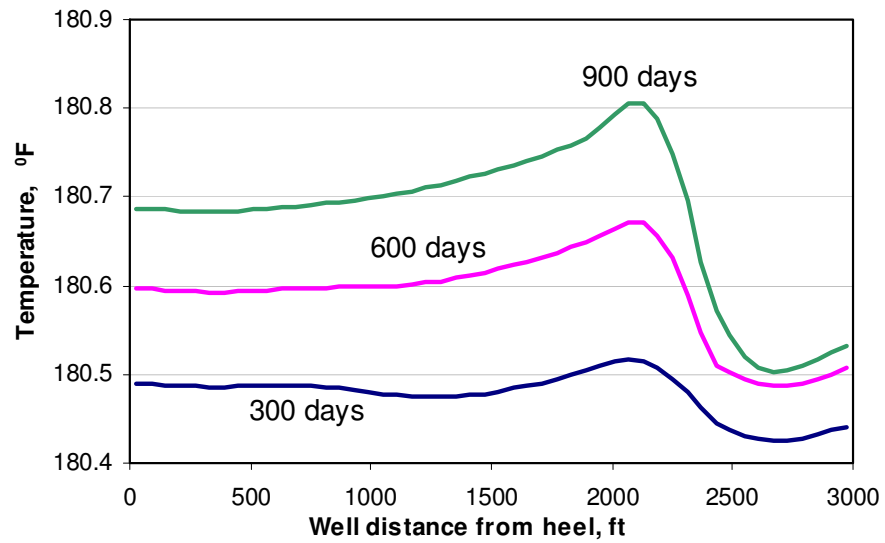
Fig. 4.31 Wellbore temperature distribution
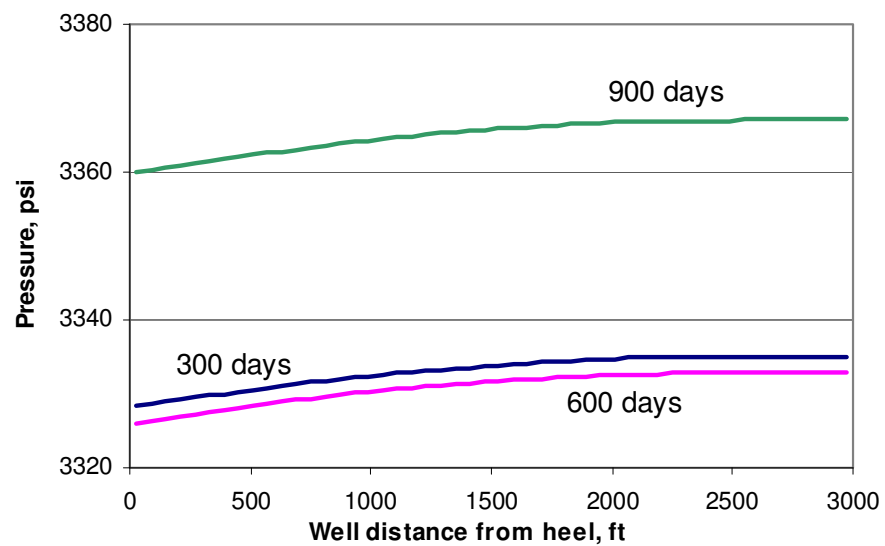
Fig. 4.32 Wellbore pressure distribution

4.2.2 Inversion Results

The inversion procedure is applied to this example. Suppose that only temperature is measured, as shown in Fig. 4.31. To start with, the reservoir is subdivided to several sections according to the temperature trend or temperature derivative. Fig. 4.33 shows reservoir sections inferred based on the temperature data. In each section, the permeability is assigned a constant value. The permeabilities are considered unknown variables that need to be determined from the inversion process. Because the measured temperature is only along the horizontal well (x direction), the estimated reservoir permeability distribution is aligned along the well as shown in Fig. 4.33.
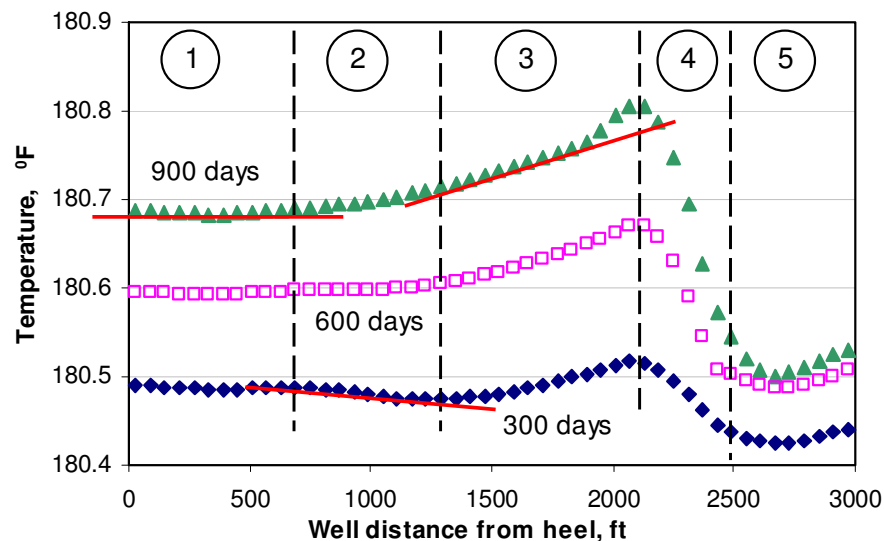
Fig. 4.33 Separate reservoir to sections by temperature data

First, the horizontal well temperature is calculated from the forward model by adjusting the permeability value in each section, until the calculated temperature match

the observed data, as in Fig. 4.34. The inverted permeability at this temperature matching condition is shown in Fig. 4.35, which is the contour of the true permeability distribution. Although the temperature does not match perfectly, the simulated results follow the trend of the observed data. The contour comparison in Fig. 4.35 indicates that the temperature inverted permeability agrees with the true permeability qualitatively.
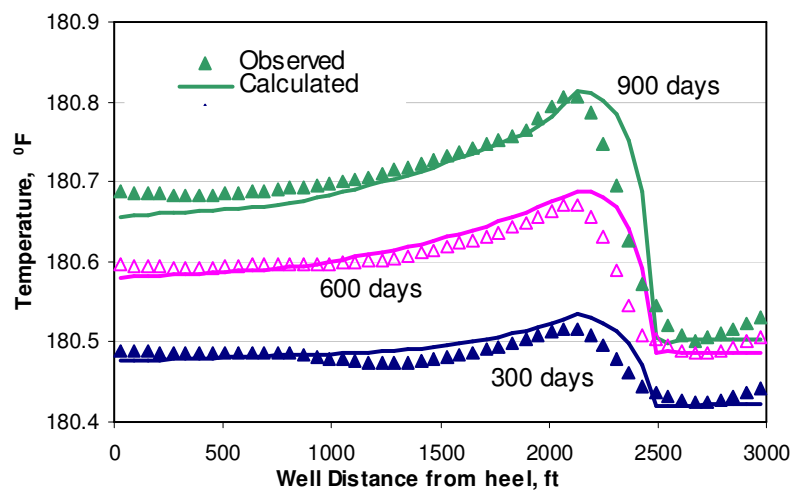
Fig. 4.34 Matched temperature data of water injection example
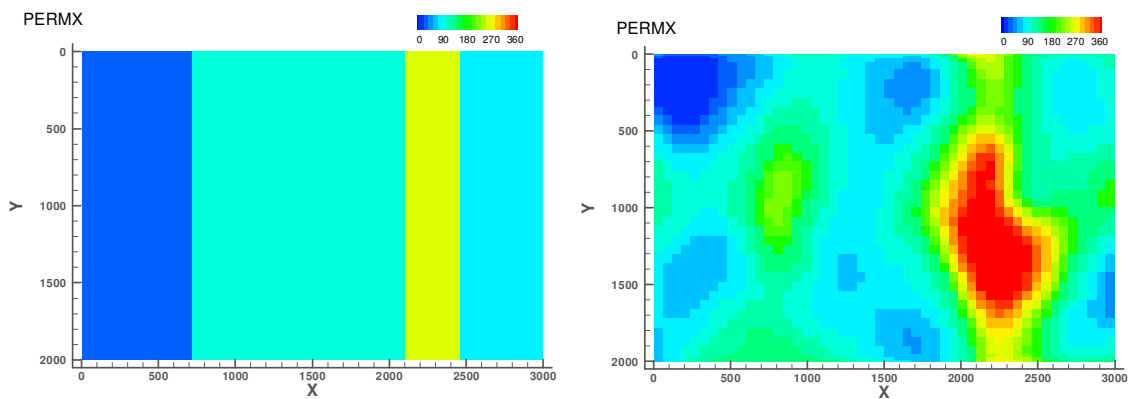
Fig. 4.35 Temperature inverted perm vs. true perm, contour

Based on the temperature inverted permeability distribution, we also obtain flow rate profiles for oil and water along the horizontal well at time 900 days in Fig. 4.36. The interpreted result of flow rate profiles is acceptable. The water entry location is detected correctly, and the water and oil flow rate distributions are close to the reference case.
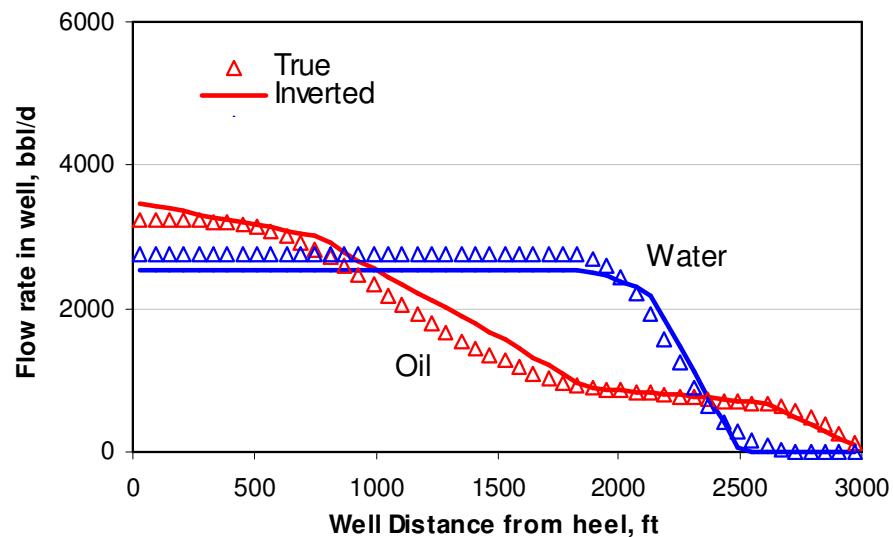
Fig. 4.36 Inverted water and oil flow rate profiles of water injection example

The arithmetic, geometric and harmonic means of inverted regions of the true permeability distribution is calculated, and compared with the temperature-inverted permeability, as shown in Fig. 4.37. The results indicate that the 1D temperature inverted permeability, indeed, captures the basic characteristics of the true permeability field, such as the low and the high permeability ranges.

The water-cut history calculated from the temperature inverted permeability distribution is shown in Fig. 4.38. The simulated water-cut history follows the trend of

the observed data, but still shows significant mismatch. We can also see that the inverted temperature at the high permeability section increases faster than the observed data. Some of these discrepancies arise from the fact that the inverted permeability is only 1D, which is an approximation of a 2D true permeability. An improved work including production history information will be presented in Chapter V.
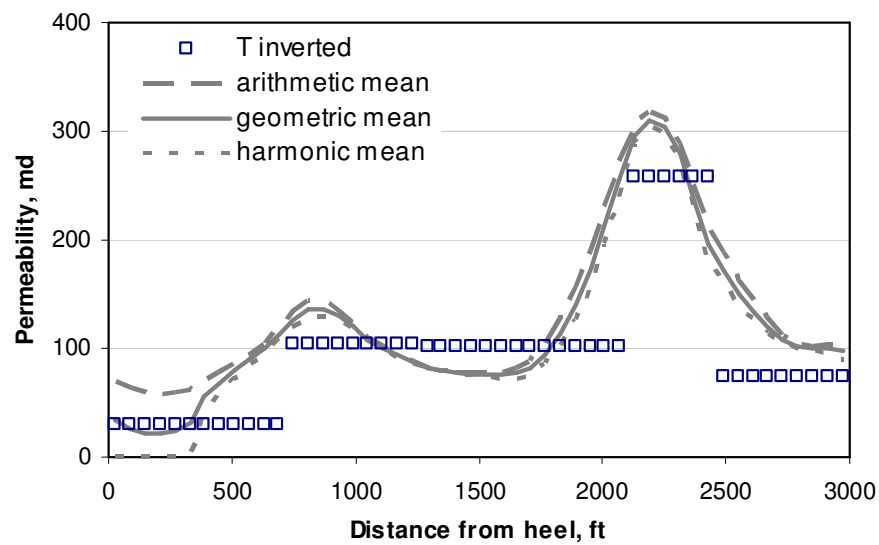
Fig. 4.37 Temperature inverted perm value vs. true perm average at y direction
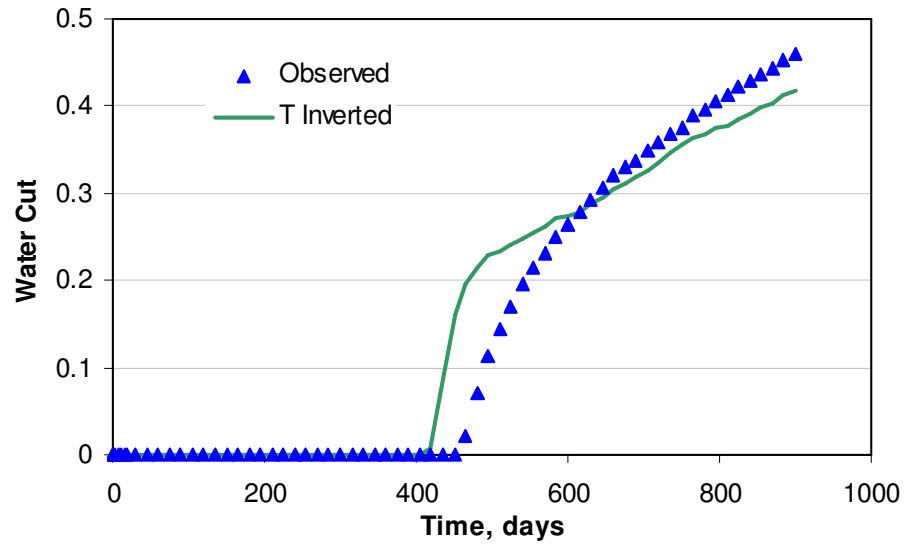
Fig. 4.38 Inverted water cut vs. observation

CHAPTER V

APPLICATIONS OF DOWNHOLE TEMPERATURE AND PRESSURE

MEASUREMENT

Three applications are presented in this chapter. Locating water or gas entry, optimizing production in ICV equipped wells, and increasing resolution of reservoir characterization by temperature information. The first application, locating gas or water entry in oil producing wells, is a detailed expansion of the synthetic examples showed in Chapter IV, here we apply the new method to some field cases.

In the second application, a procedure is provided to use temperature feedback to control Inflow Control Valve (ICV) in horizontal well. After a series operation, the fluid inflow rate along horizontal well is regulated by ICVs based on temperature feedback. At this inflow rate condition, performance of horizontal well will be optimized.

The last application uses temperature measurement to assist reservoir characterization and optimization. The temperature inversion only provided a coarse-scale permeability distribution. Based on this temperature inverted permeability, and coupling with a history matching method, the coarse permeability field is downscaled to a fine permeability field, which includes both temperature and production history information.

5.1   LOCATING GAS OR WATER ENTRY IN PRODUCING WELLS

5.1.1   Gas Entry in Oil Well

Gas entry in oil producing wells sometimes is detrimental. Problems mainly caused by higher mobility of gas compared with oil. This can result choking back oil rate, tubing limited production or surface facility limited production. This example is an oil/gas two phase reservoir on the North Slope of Alaska. It is based on the published data by Brady et al. (1998).

The reservoir has a strong gas cap. A horizontal well is placed 80 ft below the gas-oil contact. It is assume the formation thickness is 100 ft, width is 1400 ft, and the horizontal well is at the center of the width direction. The horizontal well was drilled with 8.5" bit and completed with a 5.5" cement liner. And the casing ID is 4". The horizontal section is from 400 to 1900 ft of measured depth, which is also the producing zone. The well was producing 2250 STB/d with a GOR of 2700 scf/STB when the production logging was operated. The oil formation volume factor is about 1.2 bbl/STB, and the gas formation volume factor is about 0.00848 rcf/SCF, which are estimated from the origin paper.

The original paper does not provide clear pressure data. We assume the well was operated at a constant pressure, 1800 psi (p_{wf}), at the heel of the horizontal well. This information is estimated from other examples in North Slope of Alaska (Frankenburg et al., 2000). We set a 35 ft gas cap above the gas-oil contact, which has a constant pressure of 2800 psi at the top boundary.

The fluid properties are estimated from the information about fluid at Prudhoe Bay (Jerauld, 1997). Gas-oil relative permeability is also based on this source (Jerauld, 1997; Johnson et al., 1959). Table 5.1 lists some basic information we used in the inversion process for the reservoir and wellbore system. The gas density will change significantly when the pressure change is big, and they are calculated by empirical relations (Dranchuk and Abou-Kassem, 1975).

Table 5.1 Input for Reservoir and Wellbore of Gas Entry in Oil Well Example

Reservoir		Wellbore	
Drainage area, ft×ft	1600×1400	Well heel depth, ft	5615
Formation Thickness, ft	100	Horizontal well length, ft	1500
Gas-oil contact, ft	5535	Wellbore diameter, ft	0.708
Porosity	0.2	Wellbore location at drainage width, ft	700
Top initial temperature, ^{0}F	177.5		
Geothermal gradient, ^{0}F/ft	0.015	Pressure at heel, psi	1800
Average k_h (k_h=10k_v), md	8	Cement liner, in.	5.5
Oil viscosity, cp	1.2	Casing ID, in.	4
Gas viscosity (3500 psi), cp	0.0265	Roughness	0.001

First, we analyze the temperature data and its derivative, as shown in Fig. 5.1. The temperature has an obvious low trend near 750 ft, indicating that gas enters into the wellbore at this location, because gas has significant Joule-Thomson cooling effect. To make gas enter into the wellbore at temperature decrease range, the reservoir permeability at this location is assumed higher than the rest of well sections.

According to the analysis above, we assumed the reservoir can be segmented to six sections with different permeability: 400 to 650 ft (zone 1), 650 to 735 ft (zone 2), 735 to 755 ft (zone 3), 755 to 775 ft (zone 4), 775 to 850 ft (zone 5), and 850 to 2000 ft (zone 6). Each zone has its own permeability value. The permeability in zone 3 (735 to 755 ft) is the highest. The grids used in zone 1 to 6 are 50-ft, 25-ft, 10-ft, 25-ft, 50-ft and 100-ft respectively.
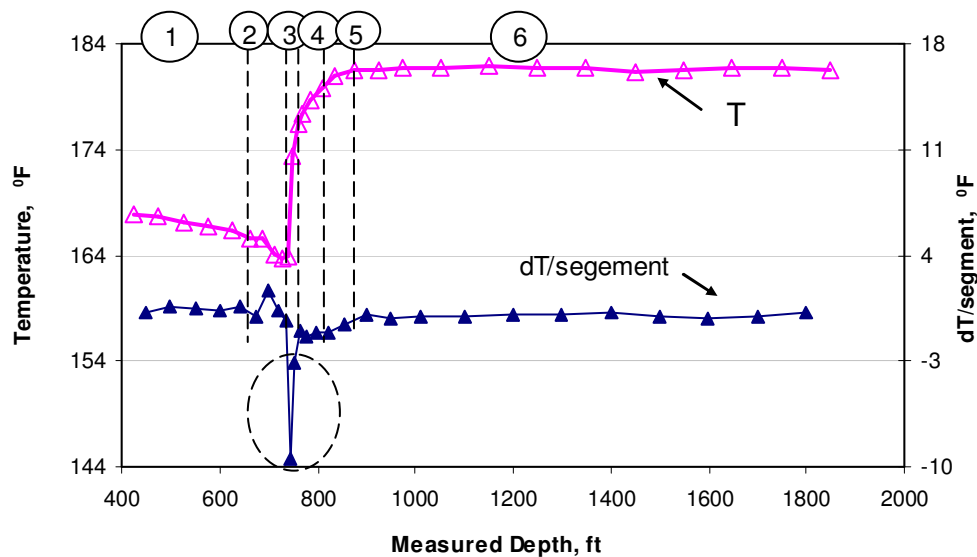
Fig. 5.1 Analysis on measured temperature

The inversion model was used then to find a permeability distribution that creates a flow distribution along the wellbore. When the temperature calculated from the generated flow distribution matches the measured temperature, the inversion is completed. Fig. 5.2 shows the inverted temperature results.
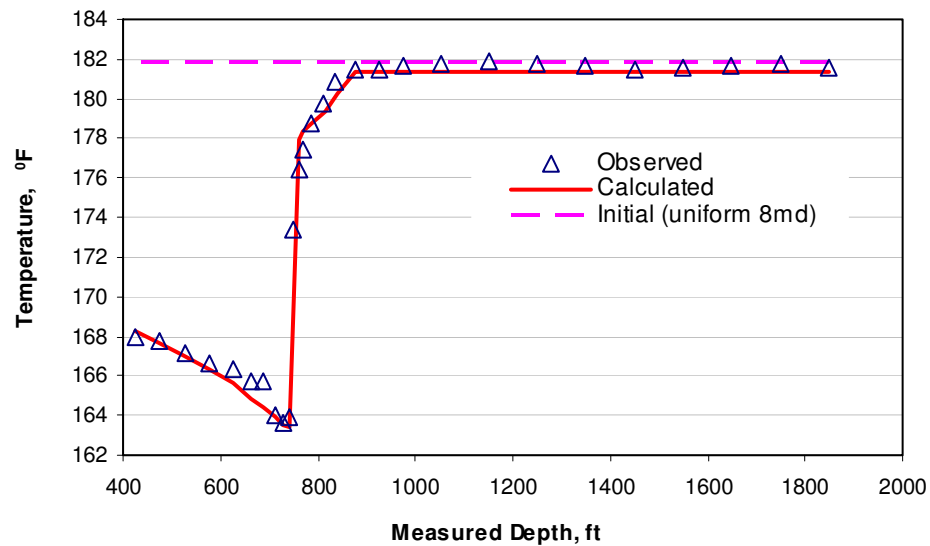
Fig. 5.2 Calculated temperature matches the measured data

When the temperature matches, we consider that the corresponding downhole flow distribution at this condition should be the true rate. Fig. 5.3 shows the inverted gas flow rate compared with the spinner measurement from production logging, and includes the oil-rate comparison between our interpretation result and Brady et al.'s result. Fig. 5.4 is the inverted permeability distribution at the temperature matching condition. The gas entry location detected by the new model agrees with the spinner interpretation result, however, the interpreted gas rate by the new model has a sharper decline in zone 3 (735 to 755 ft) compared with the spinner interpretation.
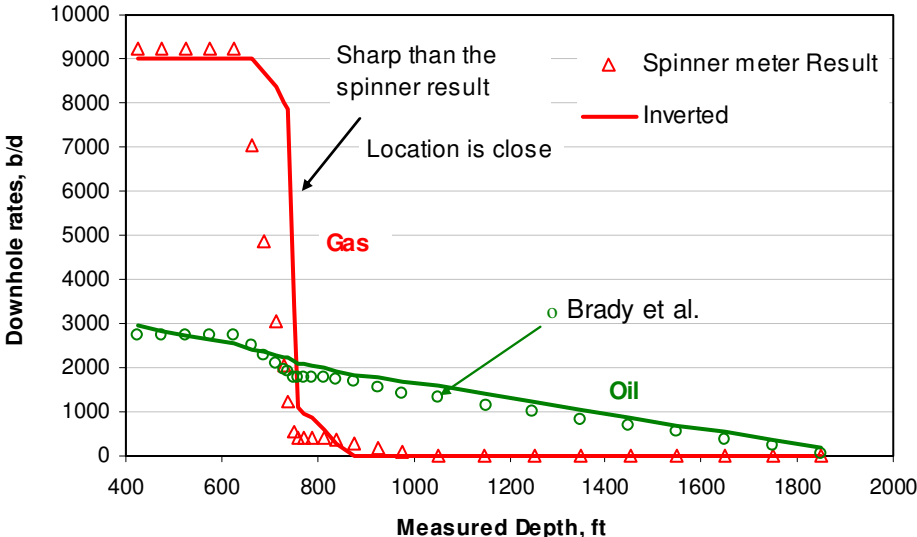
Fig. 5.3 Model interpretation result vs. spinner measurement
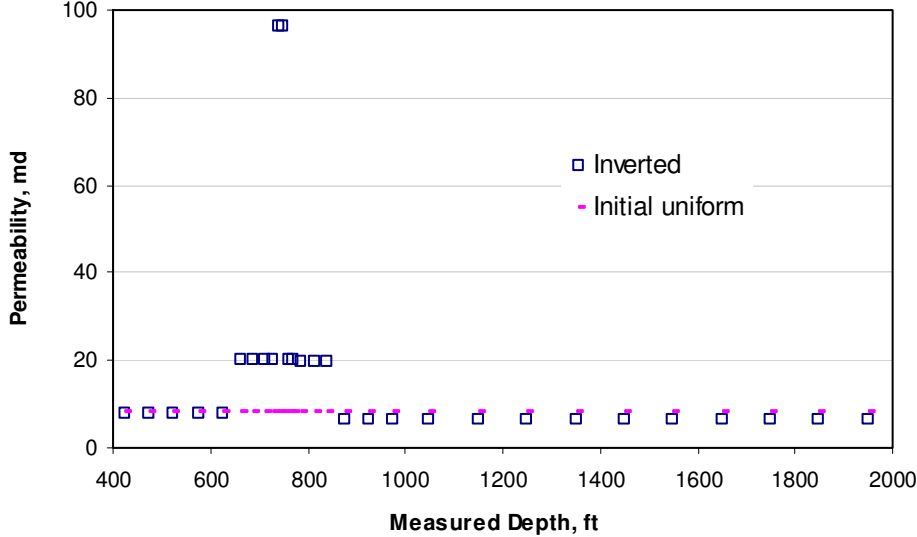
Fig. 5.4 Inverted permeability distribution of gas entry oil well example

5.1.2   Water Entry in Oil Well

Water production is one of the biggest production problems today around the world. Detecting water entry in a horizontal well is critical important in horizontal well production. This example shows how to use the new method to interpret water entry more precisely from temperature data.

The example is located in the Wandoo field, the North West Shelf of Australia (Carnegie et al., 1998). Temperature and pressure data were measured by production logging, which provided oil and water rates. Fig. 5.5 shows the field measured data.
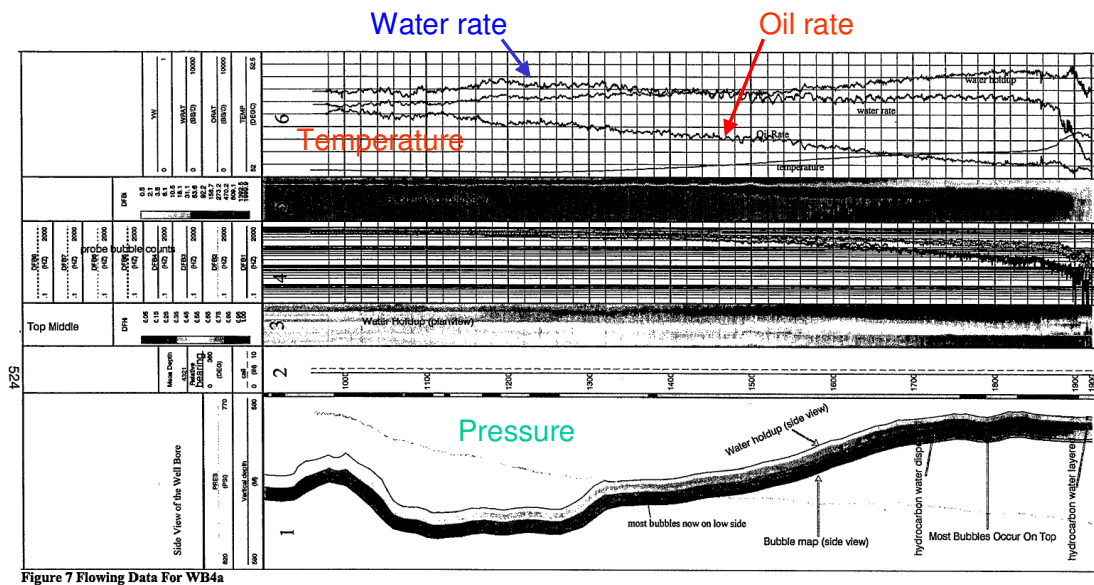
Fig. 5.5 Field measured temperature, pressure and flow rates (Carnegie et al., 1998)

The formation is about 22 m thick and the oil zone is between a small overlying gas cap and a strong aquifer. The gas-oil contact is at 577.3 m and the oil-water contact

is at 599.1 m. The gravity of the oil is 19^0 API with an in-situ viscosity of over 15 cp, and the reservoir permeability ranges from 500 to 10,000 md. We use the range of measured depth from 970 to 1930 m as the production zone in the model.

The horizontal well is located at about 585 m vertical depth. The length of the well is about 1000 m, and the change of its true depth is less than 7 m. It is very close to truly horizontal. The well was completed with pre-perforated liner and has a 9 5/8'' casing cemented into 12.25'' open hole. Because the formation width is not provided in the paper, we assumed the reservoir width to be 667 m, and the horizontal well is located at its center. At the surface, the observed surface flow rates were 3490 STB/d of oil, and 7265 STB/d of water at the time of production logging. The measured oil rate at the heel of the horizontal well was about 5080 bbl/d. The difference of oil rate at surface and downhole may be caused by the measured error of oil hold-up. In the inversion process, for the horizontal well, we set a constant liquid flow rate of 10800 STB/d as the inner boundary condition for pressure and saturation simulation.

Table 5.2 lists some basic input we used in this inversion process for the reservoir and wellbore. Other thermal dynamic properties used here are the same as Table 3.2.

Table 5.2 Input for Reservoir and Wellbore of Water Entry Oil Well Example

Reservoir		Wellbore	
Drainage area, m×m	960×667	Depth of the wellbore, m	585
Thickness, m	22	Horizontal well length, m	960
Top depth, m	577.3	Wellbore location at drainage width, m	333.5
Water oil contact, m	599.1	Liquid production rate, bbl/d	10800
Porosity	0.2	Wellbore diameter, ft	1.021
Temperature at 575.8 m, ^{0}F	124.7		
Geothermal gradient, ^{0}F/ft	0.01	Casing ID, in.	9.625
Oil viscosity, cp	15	Casing roughness	0.001
Water viscosity, cp	0.55		

First, based on the observation of temperature data trend, we assumed the reservoir can be segmented to six sections by permeability: zone 1 (970 to 1270 m), zone 2 (1270 to 1730 m), zone 3 (1730 to 1850 m), zone 4 (1850 to 1890 m), zone 5 (1890 to 1910 m), and zone 6 (1910 to 1930 m). The permeability in zone 5 should be the highest because the highest measured temperature is located here. The permeability in zone 6 is the second highest. Fig. 5.6 shows the measured temperature data with six segments.
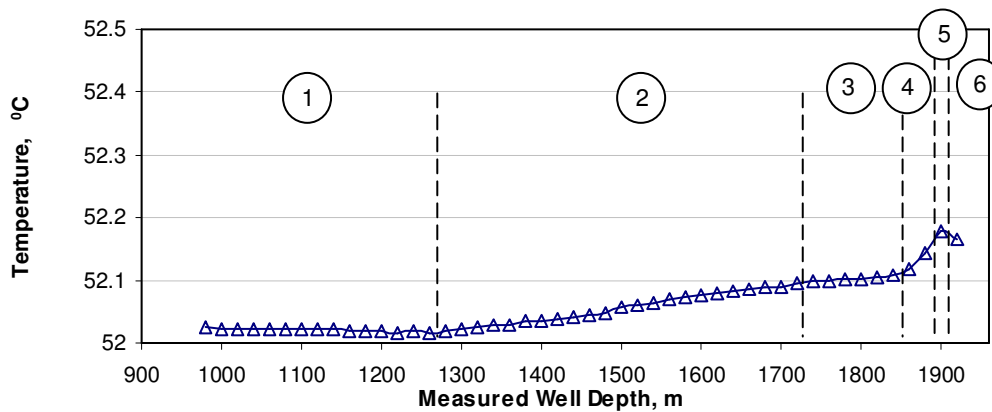
Fig. 5.6 Use measured temperature to separate reservoir for inversion

The inversion program was applied until the objective function reaches the satisfied minimum, which means the forward-model-calculated temperature and pressure match the measured data. Fig. 5.7 shows the measured, the inverted, and the initial guess of the temperature profiles, and Fig. 5.8 is the result of pressure. It is obvious that reservoir permeability is not uniform. After the inversion process, the temperature matches well, and the inverted pressure is closer to the observed data than the initial guess.
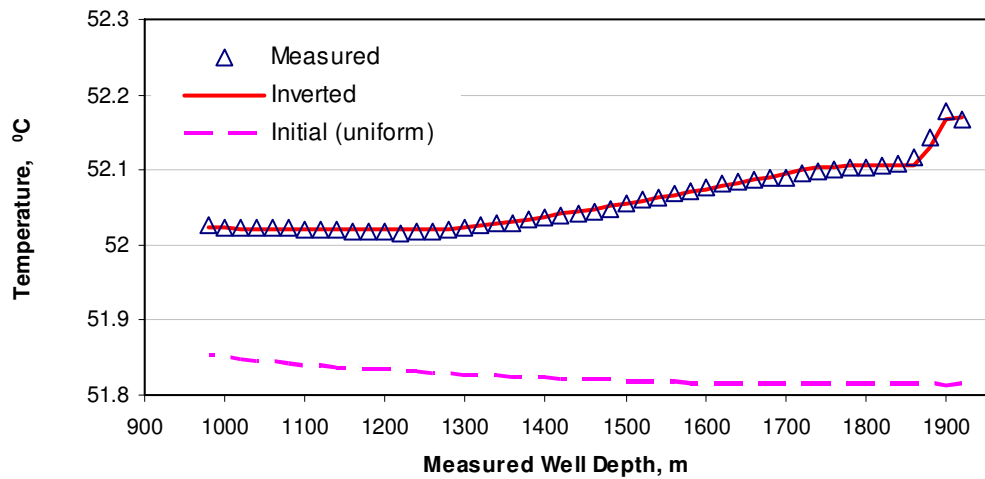
Fig. 5.7 Match measured temperature data of water entry oil well example
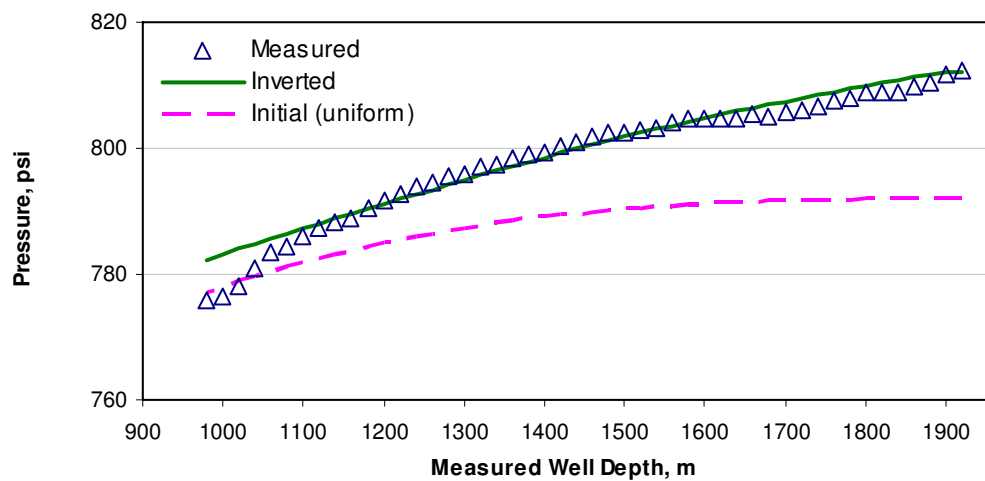
Fig. 5.8 Match measured pressure data of water entry oil well example

The inverted permeability at the temperature and pressure matching condition is given in Fig. 5.9. The permeability at the toe of the horizontal wellbore is about 10~100 times higher than the permeability at other sections. According to Carnegie et al. (1998),

the toe of this well intersects the high permeability sand. The inverted result coincides with this point.
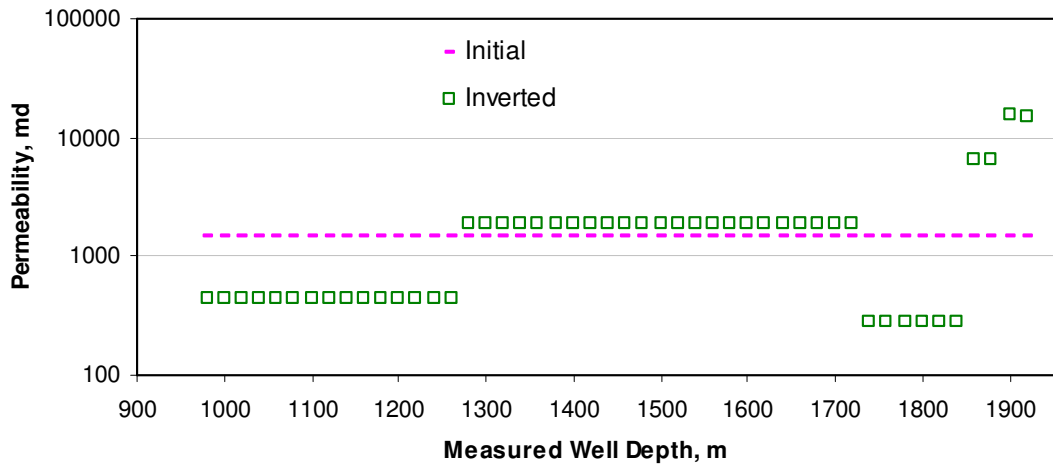
Fig. 5.9 Inverted permeability distribution of water entry oil well example

The interpretation result of oil flow rate is shown in Fig. 5.10, and Fig. 5.11 is the result for water. The inverted flow rate profiles agree with the measured data from production logging. Because almost 95% water comes from the toe of the wellbore, which is only 80 m, and the oil rate here is not very high, we may want to shut in this section to avoid high water cut.
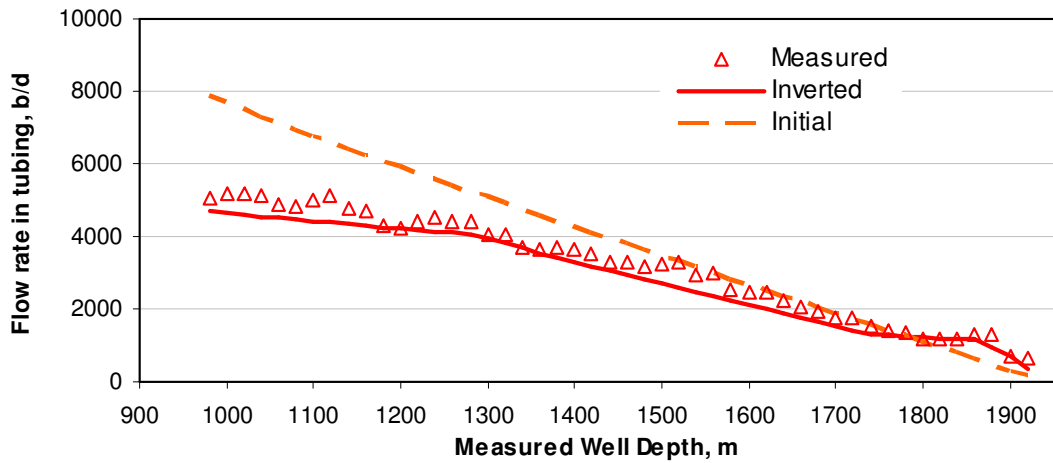
Fig. 5.10 Model interpretation compared with production logging measurement, oil
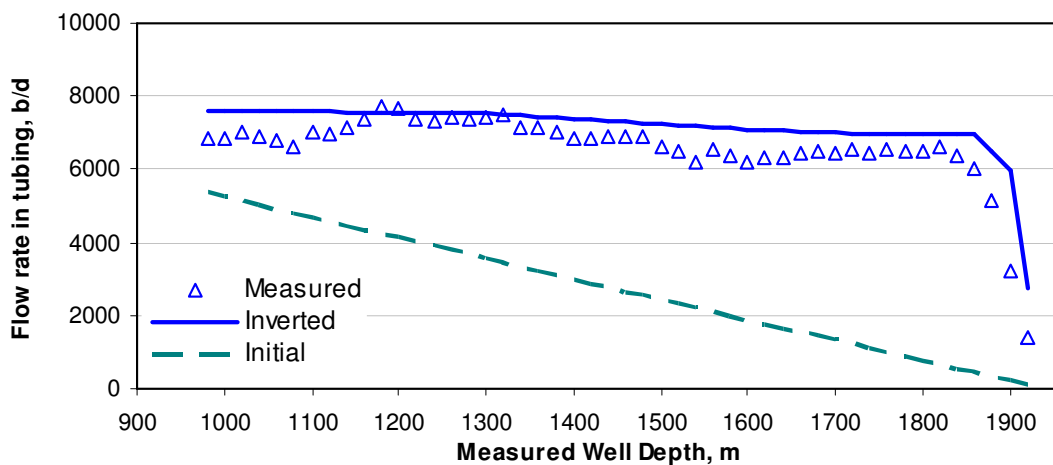
Fig. 5.11 Model interpretation compared with production logging measurement, water

5.1.3 Heavy Oil Well with Water Bottom

This example shows an oil producing well in the Zuata (Sincor) Field, Venezuela, which is an extra heavy oil environment (Foucault et al., 2004). The formation is about 75 ft thick. A high permeability zone of about 670 m with a permeability of 19 Darcy is the

target zone to produce heavy oil, and the measured depth of this zone is from 1244 to 1915 m. The reservoir has a bottom water-aquifer, and the well is set at 60 ft from the bottom boundary of payzone. The reference pressure is 570 psi at the depth of the horizontal well location. The horizontal well was completed with a 7" liner. Table 5.3 lists the reservoir and well information we used in the model as input. They are collected from the original paper (Foucault et al.). Other thermal dynamic properties used here are the same as Table 3.2. The temperature data was collected by downhole fiber optic sensors.

We assumed a reservoir width of 667 m. The horizontal well is located at the center of width. The temperature data was collected when the well was produced about 3 months, and it is shown in Fig. 5.12 as the curve with noise from 644 to 1800 m, which includes vertical part of the well and no-producing zone. According to the temperature data, we assumed the reservoir can be separated to three zones by permeability: zone 1 (1244 to 1750 m), zone 2 (1750 to 1800 m), and zone 3 (1800 to 1915 m). Each zone has different permeability value and the permeability in 1750 to 1800 m is the highest. In the forward model, the well produced 1000 stb/d at first 20 days, and then shut in for 60 days. After that, the well produced a constant liquid rate of 2400 stb/d.

Table 5.3 Input for Reservoir and Wellbore of Heavy Oil Well Example

Reservoir			Wellbore	
Reservoir Length, ft	2200		Diameter, ft	1
Reservoir Width, ft	2000		Length of wells, ft	2200
Formation Thickness, ft	75		Tubing diameter, in.	8
Temperature at formation top, ^{0}F	122.8		Tubing roughness	0.001
Geothermal gradient, ^{0}F/ft	0.0157		Well distance to top, ft	
Average k_h (k_h=10k_v), Darcy	19		0~1450 ft section	15
Oil viscosity, cp	2000		1450~2200 ft section	25
Water viscosity, cp	0.8			

Because we do not have the numerical value of the observed temperature data and the raw data contains noise, we use the forward model to match the raw data by manually changing the permeabilities. Fig. 5.12 is the matched temperature data from forward model calculation and the observed raw data. The matched temperature curve has the same trend as the observed data, and its value is also close to the observed data. The inverted permeability for the three sections is 19 Darcy, 46 Darcy, and 11 Darcy respectively, showed in Fig. 5.13.
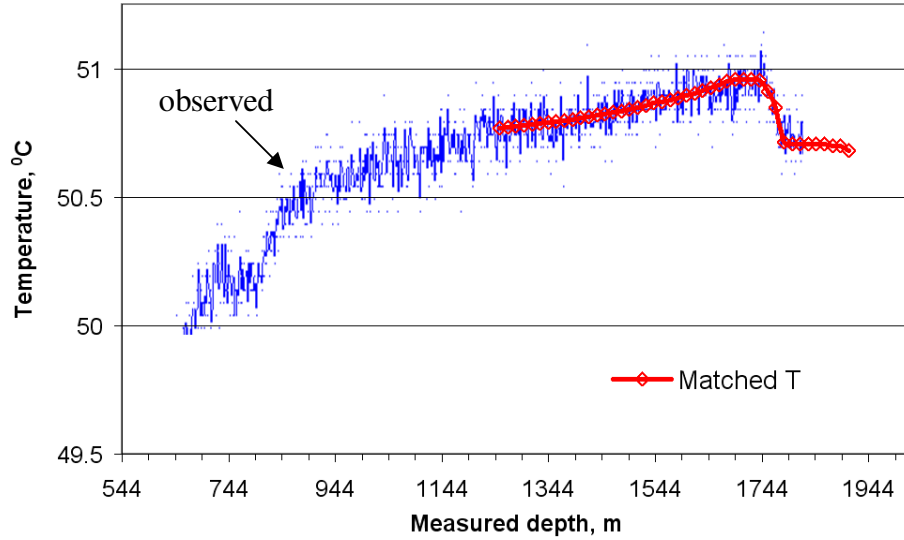
Fig. 5.12 Match measured DTS temperature data
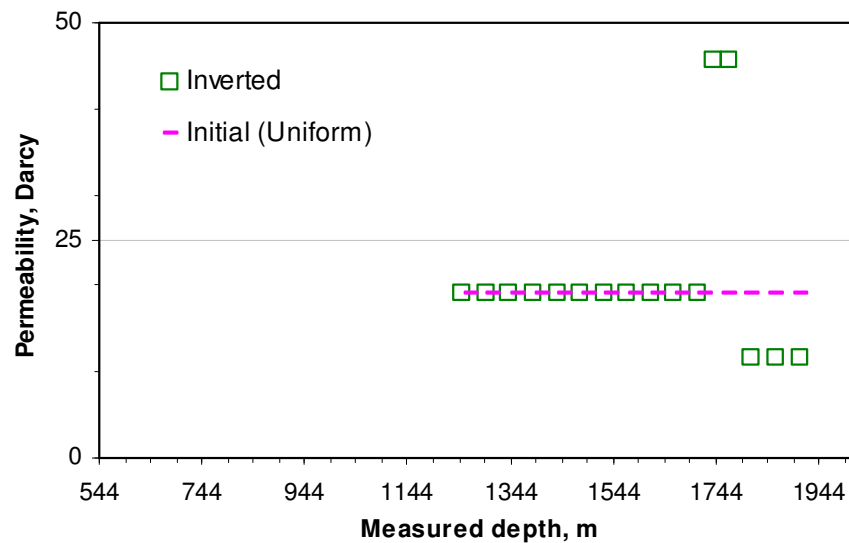
Fig. 5.13 Inverted permeability distribution of heavy oil well example

In this case, we do not know downhole flow distribution, but the production history at surface was provided. With the inverted permeability distribution, we also successfully match the production history. Fig. 5.14 shows that the forward calculated

result follows the trend of measurement, which indicates that the inverted permeability is acceptable. Then we use this permeability to obtain oil and water flow profiles along the wellbore, as shown in Fig. 5.15. Water comes into the well along the entire wellbore, but it has a higher water inflow rate in the section of 1750 to 1800 m than other sections of the well.
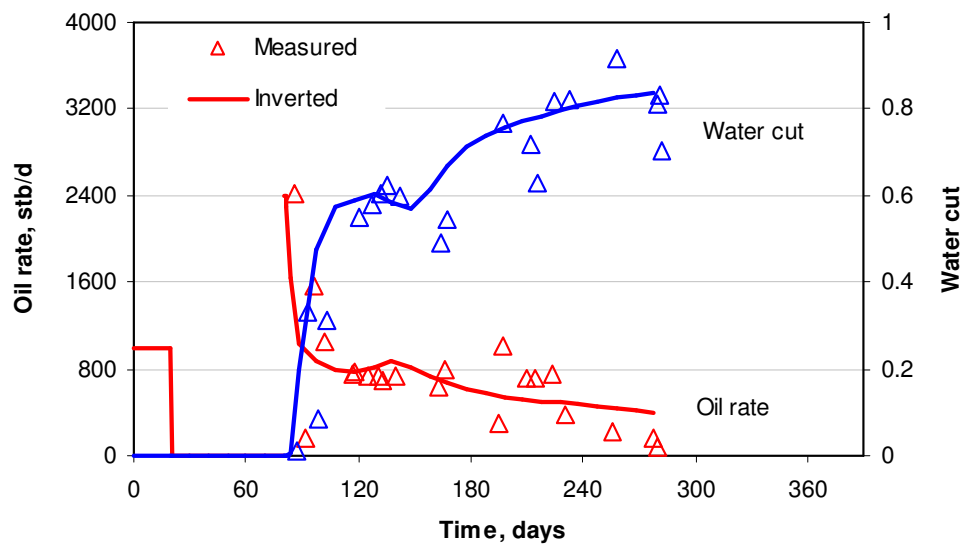
Fig. 5.14 Inverted production history follows the trend of measurement
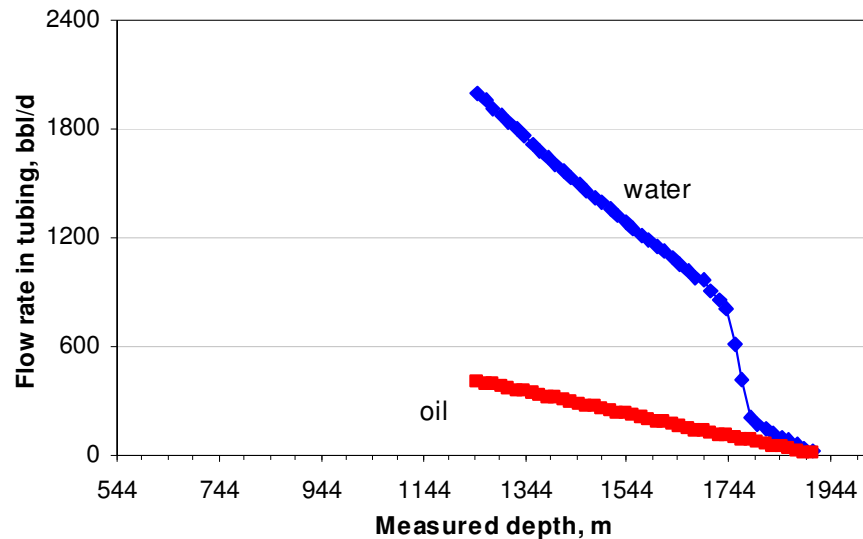
Fig. 5.15 Inverted flow rate profiles of oil and water

5.1.4 Water Entry in Gas Producing Well

This example diagnoses water entries in a gas well in Barnett shale. The reservoir has extremely low matrix permeability from 0.00005 to 0.001 md, and its initial pressure is about 3000 psi. The reservoir has no water aquifer. The horizontal well was hydraulically fractured, and some water remained in the fractures. The horizontal well was shut in for several years. It was re-opened after a long time shut in, and then production logging was run to identify the gas and water entry locations in the well. Fig. 5.16 gives the measured temperature, and flow meter data. Pressure, well trajectory and perforated locations are plotted in Fig. 5.17. At the surface, the gas flow rate of this well is about 300 Mscf/d, and the water production rate is about 100 stb/d. The flow meter measurement has suddenly decrease and increase at some location, and its trend is complex. This is not a good response for interpretation. However, the measured

temperature data has obvious increasing and decreasing trends along the wellbore. Generally, because of the pressure drop from reservoir to wellbore, the Joule-Thomson effect will cause water temperature to increase, and gas temperature to decrease. Therefore, according to the temperature trend in Fig. 5.16, we assume water comes into the well at locations where temperature increases sharply, and gas enters into the well mainly through locations where temperature decreases quickly.

Because the reservoir permeability is extremely low, the major entries of fluids from reservoir to wellbore are from fractures. To use the model, we separate the reservoir to a uniform size grid (50 ft) at horizontal well direction. It is hard to simulate the exact fracture size by this model. Therefore, we assume high permeability for grids where temperature has significant variation. These grids are assumed to include some fractures, and the fracture effect is estimated by these equivalent high permeability values. Because of the fracture, the difference of low and high permeability might be very significant. So the porosity we used for low permeability sections is 0.04, and for high permeability sections, it is 0.1. In addition, the well is perforated in almost each grid.

From the measured temperature data, we can identify water entry locations. Because the water comes from the remaining fluid after the hydraulic fracturing, we assume the initial water saturation is close to 1.0 at these pre-identified locations in reservoir. The reservoir top and bottom are no-flow condition, and the reservoir boundary is assumed to be constant pressure.
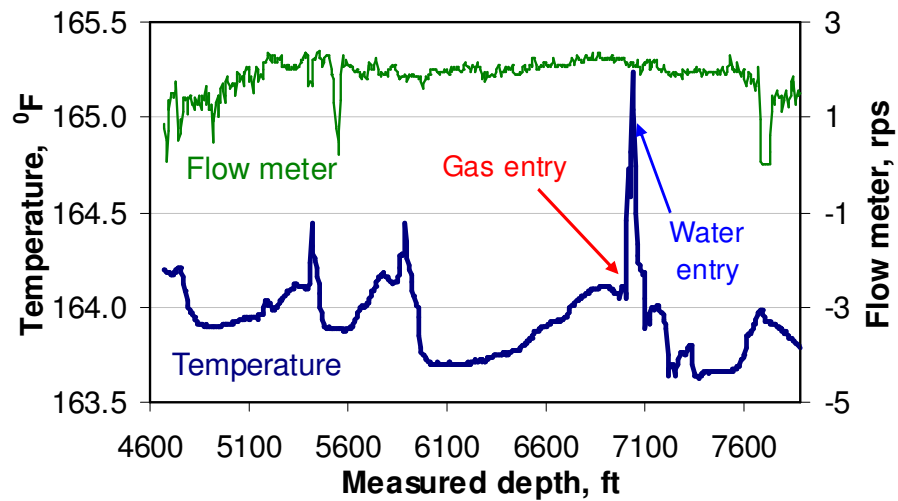
Fig. 5.16 Measured temperature and flow meter data
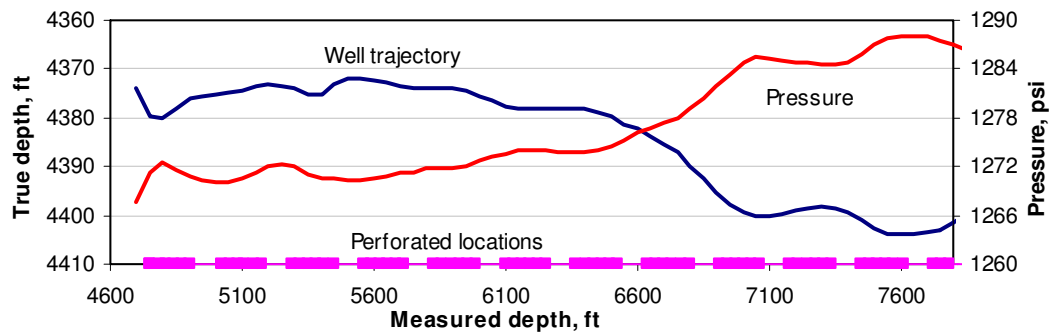
Fig. 5.17 Measured pressure, well trajectory and perforated locations

The wellbore has about 30 ft change at depth direction (Fig. 5.17). It is very small compared with the 3000 ft length of wellbore, but it causes that the geothermal temperature changes along well trajectory. In this work, we assume that the well is located at the depth of 4380 ft, which will simplify the model but cause a certain error. On the other hand, pressure distribution has very similar trend as the well trajectory,

which indicates that if we assume the well vertical depth is constant, we may not correctly calculate the trend of the wellbore pressure as the measurement, and it will makes the convergence of inversion more complex when the measured pressure is also taken into account in the objective function. Thus, we only use temperature in the objective function, and we assume a constant pressure, 1267 psi, at the heel of the horizontal well during the production. Instead of total surface fluid rate, pressure becomes the inner boundary condition for the reservoir pressure and saturation simulation. Table 5.4 provides the basic input data we used in the inversion process for reservoir and wellbore.

Table 5.4 Input for Reservoir and Wellbore of Water Entry Gas Well Example

Reservoir		Wellbore	
Drainage area, ft×ft	3350×2000	Depth of the wellbore, ft	4380
Formation Thickness, ft	160	Horizontal well length, ft	3150
Top depth, ft	4310	Wellbore diameter, ft	0.375
Porosity	0.04, 0.1	Wellbore location at	
Initial temperature at 4310 ft, ^{0}F	162.8	drainage width, ft	1000
Geothermal gradient, ^{0}F/ft	0.015	Pressure at heel, psi	1267
Average k_h (k_h=10k_v), md	0.0005		
Water viscosity, cp	0.52	Tubing ID, in.	2.375
Gas viscosity, cp	0.045	Roughness	0.0001

Using the input data, we can run the interpretation model. Fig. 5.18 shows the model calculated temperature and the measured data. The simulated temperature follows

the trend of the observation. The major changes on the observed temperature curved are captured by the forward-calculated-model. It means that the reservoir characterization and water-gas distribution may be close to the true situation.
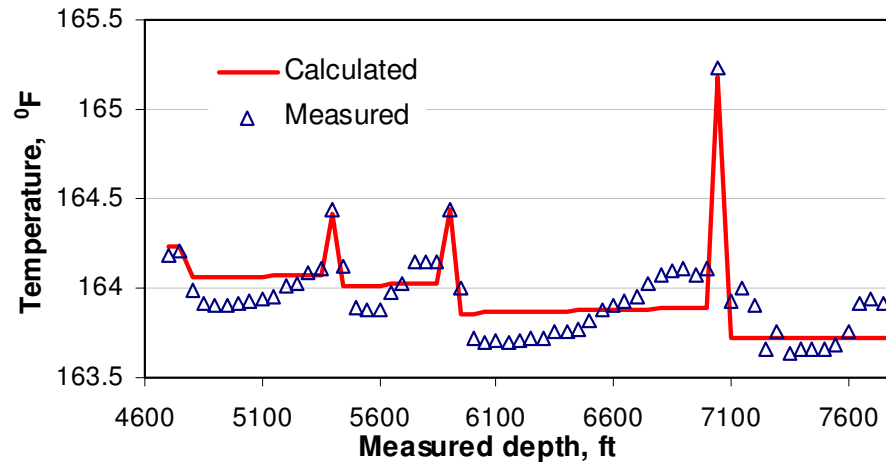
Fig. 5.18 Calculated temperature matches the trend of measured data

At this temperature matching condition, we also obtain downhole flow conditions. Fig. 5.19 provides the inverted gas and water flow rates in tubing, and Fig. 5.20 is the inverted permeability distribution. The interpretation result indicates that water and gas mainly enter into the horizontal well at some small ranges, which may be fracture locations.

From the interpretation we can see that there are at least three major fractures along the horizontal well, with most likely the fracture at 7100 ft producing the highest gas rate, and the other two fractures (at 5400 ft and 5900 ft) perform about the same. Water is produced almost evenly along the fractures.
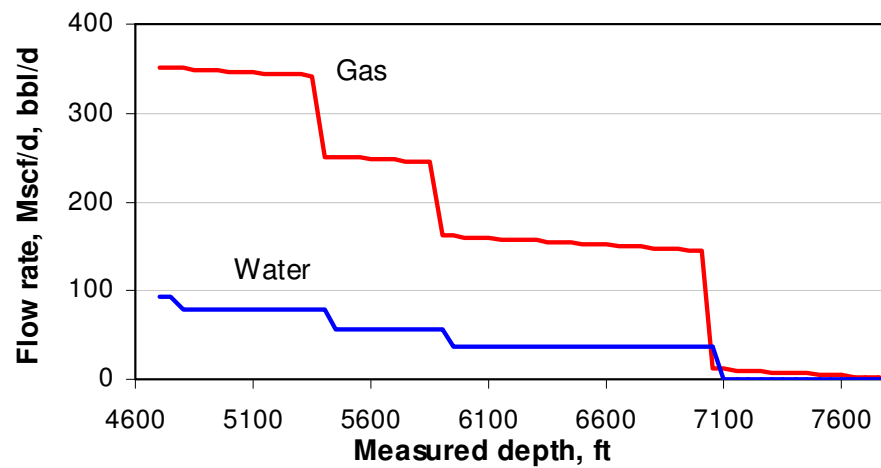
Fig. 5.19 Inverted flow rate distributions of gas and water
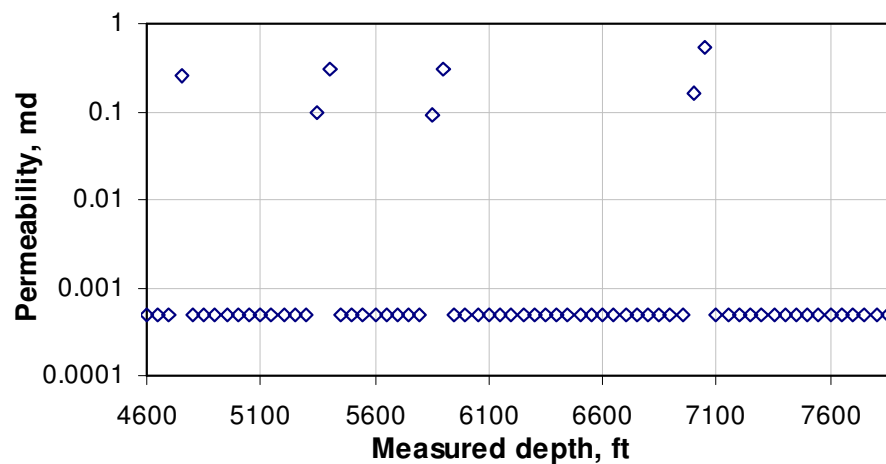
Fig. 5.20 Inverted permeability distribution of water entry gas well example

5.2   OPTIMIZE HORIZONTAL WELL PERFORMANCE BY INFLOW CONTROL VALVE FROM TEMPERATURE FEEDBACK

Downhole flow conditions are key information to optimize well performance. Recently, intelligent completions, such as inflow control valves (ICV) or inflow control devices (ICD), have been used to operate well performance based on downhole flow conditions or production data. Many studies have been presented in analyzing these data for production optimization. Alaeddin and Maizeret (2003) used production logging technology to evaluate the contribution of two horizontal legs and possible water entry locations. This information can help to manage reservoir for optimizing the re-development plan of the field. Real time production data is also used for optimizing oil recovery in multilateral wells (Alghareeb et al., 2009). Based on the production history data and reservoir permeability distribution, an optimum ICV configuration can be obtained so as to minimize water cut and maximize net present value. Qing and Davies (2009) presented a generalized predictive control for management of ICVs by production feedback update. Alhuthali et al. (2007) provided an optimal waterflood reservoir management by rate control. Their results show that the correct rate control for horizontal well with ICV completions can delay water breakthrough and significantly increase the reservoir recovery for a heterogeneous reservoir.

Much of the previous optimization works are based on assumed reservoir geologic models. Then, the downhole flow condition in horizontal wells can be predicted via forward modeling. However, in some situations, reservoir geologic models may not be available, or not exact enough to predict correct downhole flow conditions.

Production history matching is routinely used to update geologic models. But some important production data, such as water cut history, is useful when water breakthrough is observed. On the other hand, some optimized operations may achieve good result when they are used at the beginning of the well producing (Alhuthali et al., 2007).

In the previous chapter, it was concluded that downhole temperature data in horizontal well can reflect the inflow rate distribution. The transient temperature behavior can be measured by downhole permanent sensors such as distributed temperature sensor (DTS) throughout the lifetime of the well, which means that we probably can obtain downhole flow conditions at very early time.

Flow profile along a horizontal well strongly depends on the heterogeneity of the reservoir that is connected to the wellbore. Non-uniformly distributed flow in a horizontal well usually causes production problems such as early water or gas breakthrough at high permeability zones. Rather than wait until the well starts producing water or gas, it is suggested to use temperature distribution data as an indicator to locate the problem zones, and to operate ICVs to delay the early breakthrough. The purpose of this work is to use inflow control valves (ICV) to relocate the inflow distribution according to temperature feedback at early time of a well producing life when a reliable reservoir geologic model is not available. The inflow rate distribution in horizontal wells may achieve an optimized condition when the arriving time of fluid along a horizontal wellbore close to uniform distribution. At such a condition, oil production will be improved with delayed water/gas breakthrough.

5.2.1 Application Procedure of Temperature Feedback

Realized that the uniformed flow rate distribution does not necessarily mean uniformed temperature distribution because of heat transfer while flowing through the reservoir, we first need to identify the permeability field, and then find the desired temperature profile that corresponds to the uniformed flow distribution, and finally operating ICVs to achieve the optimal condition. Fig. 5.21 shows this procedure. It includes the following steps:

1. Start from an initial condition that assumes all ICVs are fully open.

2. Observe temperature distribution outside of ICVs. According to the measured data, estimate the inflow rate distribution along horizontal well, and identify the high inflow sections.

3. Establish a desired temperature distribution which yields an approximate optimal production condition. Estimate the flow rate change based on the temperature distribution.

4. Operating ICVs until the desired temperature distribution is achieved.

```
                          ┌─────────────┐
                          │    Start    │
                          └─────────────┘
                                 │
                                 ▼
        ┌────────────────────────────────────────────────┐
        │      Horizontal well produces, all ICVs are open │
        └────────────────────────────────────────────────┘
                                 │
                                 ▼
        ┌────────────────────────────────────────────────┐
        │        Observe temperature outside of ICVs;      │
        │ Estimate permeability and inflow rate distribution from │
        │           temperature interpretation model       │
        └────────────────────────────────────────────────┘
                                 │
                                 ▼
        ┌────────────────────────────────────────────────┐
        │ Calculated desired temperature profile based on permeability │
        │              field for uniform flow rate          │
        └────────────────────────────────────────────────┘
                                 │
                                 ▼
        ┌────────────────────────────────────────────────┐
        │ Operate ICVs and monitor temperature until it is close to the │
        │             desired temperature profile           │
        └────────────────────────────────────────────────┘
                                 │
                                 ▼
                          ┌─────────────┐
                          │     End     │
                          └─────────────┘
```
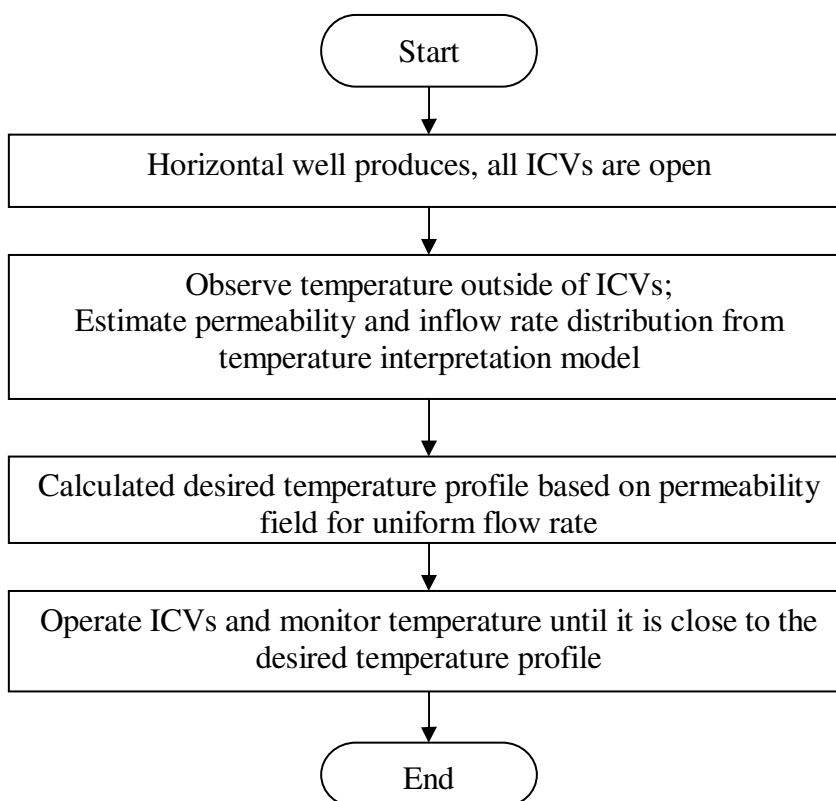
Fig. 5.21 Optimization procedure of operation on ICV from temperature feedback

ICV Effects on Temperature Behavior

The simulation on temperature behavior in horizontal well has been discussed in previous sections. If the horizontal well is equipped by ICVs, the ICV effect on temperature behavior should be considered. Muradov and Davies (2008, 2009) developed a temperature model for the wells with ICVs. They considered that the temperature effect of ICV is caused by pressure drop when fluid passes through the ICV. This temperature change can be calculated by the relation of Joule-Thomson effect:

$$\Delta T = C_D^2 \overline{K}_{JT} \Delta p \quad \text{...} \quad (5.1)$$

where Δp is the pressure change when the fluid pass through the ICV, $\overline{K}_{JT}$ is the average

Joule-Thomson effect if the fluid is multiphase, and C_D is a valve discharge coefficient,

and it is assumed to 1 in this chapter. It has a relation with the nozzle efficiency defining

for ICV flow model, and can be found in the work of Muradov and Davies (2008).

When ICVs are installed, it causes an additional pressure drop when fluid flow

through, which results in a corresponding temperature change. That is illustrated in Fig.

5.22.
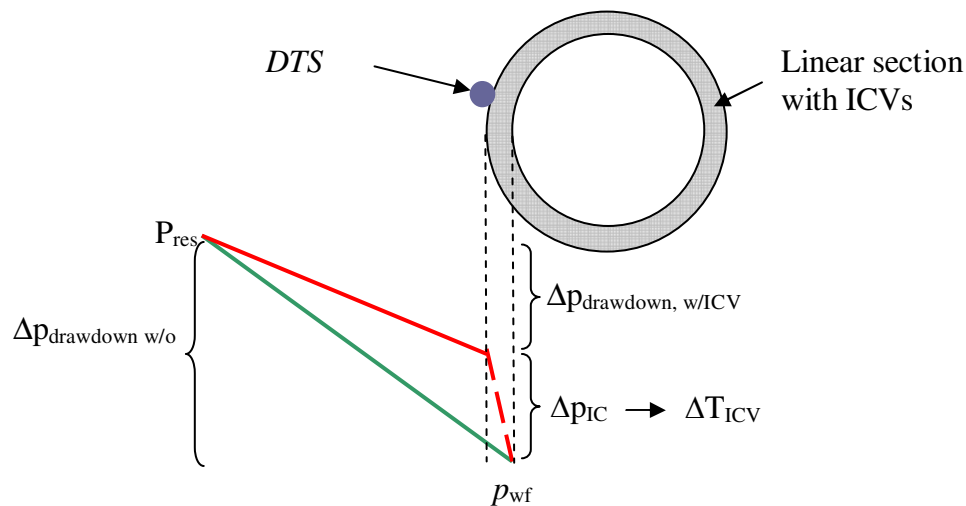
Fig. 5.22 ICV effect on pressure distribution and temperature in our model

As ICVs close up to control the flow rate, it causes an additional pressure drop.

Generally, the pressure drop through ICVs, Δp_{ICV} is relative to the flow rate passing

through the equipment (Perkins, 1993). However, this pressure drop may not be

measured, and it leads to an unknown inflow flux through the ICV. In reality, we might not know the amount of flow rate through the ICV when we make changes to it. Therefore, in the synthetic case shown here, a reasonable additional pressure was added to the inflow performance relationship for reservoir and wellbore connection. When we solve the reservoir pressure equation, the general sink/source term is modified to:

$$q_j = PI_j \left(p_{grid} - (p_w + \Delta p) \right)_j \text{...} (5.2)$$

where *PI* is the productivity index for the well presented by Peaceman (1983).

The Designed Temperature Distribution

The target is to achieve the condition where the arriving time of reservoir fluids along a horizontal well is close to a uniform distribution. This is hard to accomplish because we may not know the detailed reservoir description. We can use the arriving temperature to establish the permeability distribution, and then use it as a reference to regulate arriving time of fluid. For high inflow locations, we want to use ICVs to reduce the influx, and for low inflow locations, we assign ICVs to fully open to keep the maximum influx rate. The question is how this uniform distribution can be reflected by temperature information.

Once we understand the flow distribution without ICV regulation, we know, if ignore the pressure drop in horizontal well, the pressure drawdown distributions from reservoir to wellbore are the almost the same along the wellbore, with higher-permeability zones getting higher inflow rate and lower-permeability zones lower inflow rate. If ICVs are fully open, for oil reservoirs, temperature at higher-perm location will

be higher than the rest of wellbore location. Since using ICV to choke back flow rate generate additional pressure drop and more frictional heating (Fig. 5.22), an ideal temperature distribution should have lower temperature at higher-permeability locations. We can estimate this desired temperature distribution based on the permeability distribution we obtained from temperature assessment, and then operate ICVs to achieve the optimal condition. Most ICVs used in the field today have discontinuous operating positions (e.g., two-position: open/close, three-position: open/50% open/close, etc.). It is difficult to set exactly the ideal condition. To apply the method practically, we would gradually operate the ICVs and watch the temperature change to approach the desired condition. The following examples illustrate the procedure.

5.2.2   Bottom Water Driving Reservoir

The horizontal well structure used for this example is shown in Fig. 5.23, and Fig. 5.24 shows the reservoir geometry and the 2D permeability distribution. The horizontal well is 3000 ft long, equipped with ICVs at certain completed sections. The well is divided into 10 sections, each has 100-ft perforated zone with an ICV, and 200-ft blank section. The well is located at the middle of reservoir. A strong aquifer is at the bottom of the reservoir. The reservoir has a high permeability strip (200 md) at around 2000-ft location, with the permeability about four times of the average reservoir permeability (50 md). The input information for the reservoir and well system are in Table 4.1, and the fluid and rock thermodynamic properties are in Table 3.2.
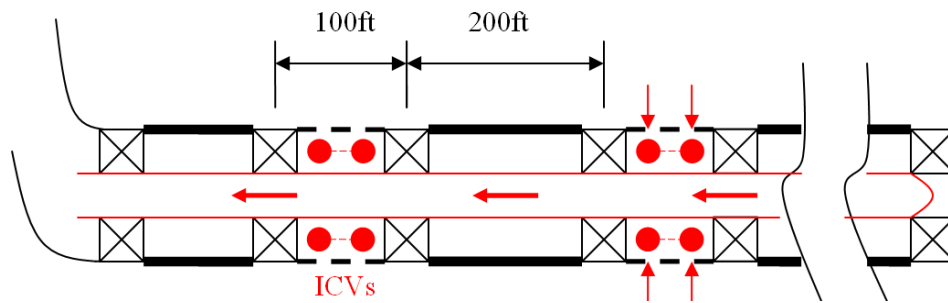
Fig. 5.23 Horizontal well structure
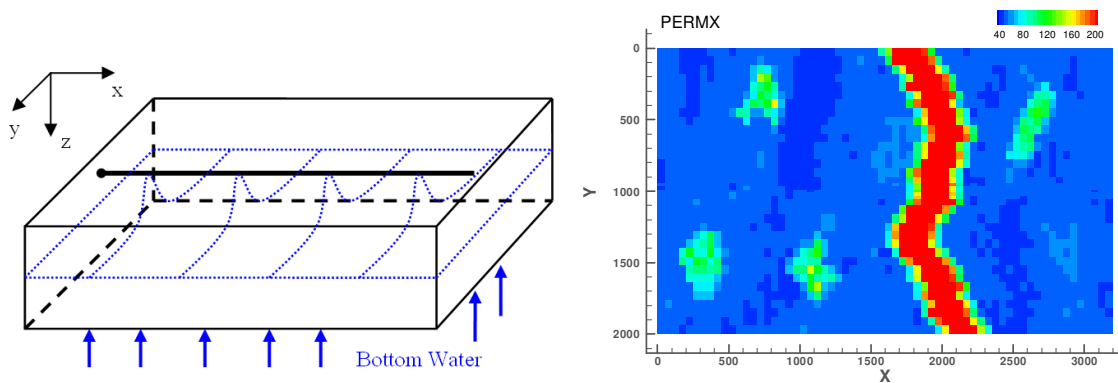
Fig. 5.24 Reservoir geometry and 2D permeability distribution

The temperature distribution in Fig. 5.25 is recorded outside of ICV at 0.5 day and 2 days, and the corresponding oil flow rate profile along the wellbore translated from the initial temperature data. During this period, all ICVs are fully open, and therefore they do not affect the temperature behavior. We observe a high temperature section from 1900 to 2100 ft. The previous study can translate this temperature profile to a flow rate distribution, shown in Fig. 5.26. This higher temperature is caused by a higher inflow rate which leads to a faster transient temperature increasing compared with the rest of the wellbore.
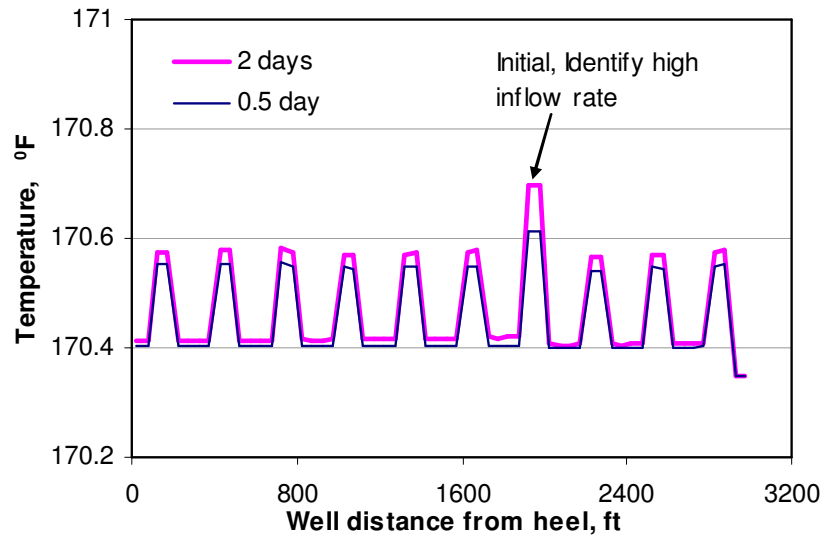
Fig. 5.25 Use temperature to identify high inflow rate before operating ICVs
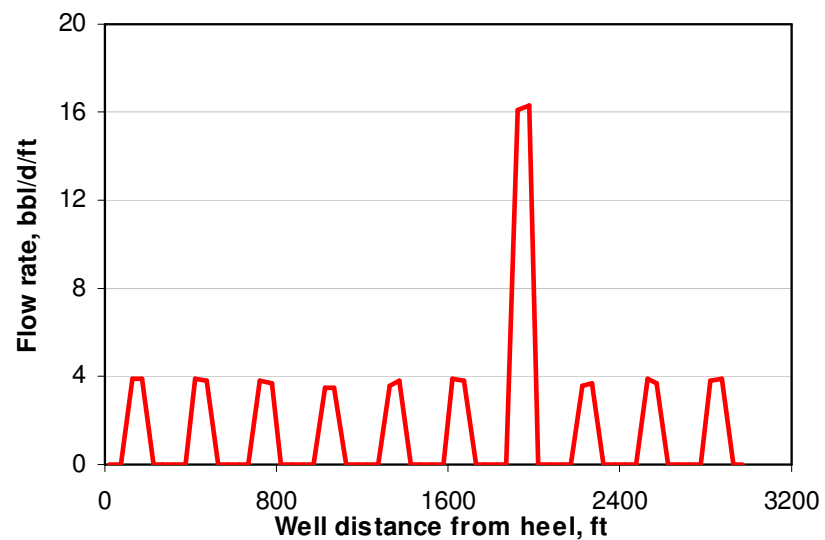
Fig. 5.26 Flow rate profile before operating ICVs

With this initial condition, we are ready to adjust the ICVs at 1900 to 2100 ft section to reduce the inflow rate. ICVs are designed as 2-position ICVs (open/close), 3-

position ICVs (open/50% open/close), 4 position ICVs, etc. When an ICV is operated to open or close at certain position, the pressure drop corresponding to the operation is unknown, so does the flow rate change. The relationship, as mentioned before, depends on individual ICV design. To include the effect of ICVs in the simulation, Eq. 5.2 is equal to,

$$q_j = \gamma \cdot PI_j \left(p_{grid} - p_w \right)_j \quad\text{.. (5.3)}$$

where γ is defined as a choking ratio for ICV, and $\gamma \in [0, 1]$. Then the equivalent pressure drop Δp is calculated by

$$\Delta p = (1 - \gamma)(p_{grid} - p_w) \quad\text{... (5.4)}$$

and Δp is further used to calculated temperature. Fig. 5.27 is the choking ratio distribution which will be used in the following calculation.
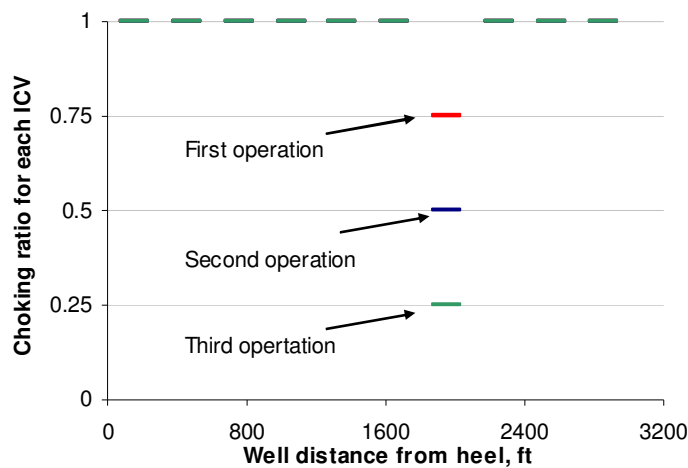
Fig. 5.27 Choking index ratio changes in simulation at different ICV stages

Suppose we start operating the ICVs at the end of 2 days of production. In this operation, γ is set to 0.75. But we do not know how much pressure drop it generates, and how much inflow fluid passes through the ICVs. Therefore, we use temperature feedback to analyze whether the operation achieves the optimal design. Fig. 5.28 is the observed temperature that is much less uniformed distributed along the wellbore after we control the ICVs. According to the procedure, this temperature distribution most likely does not meet our design requirement for optimization. Temperature at high inflow rate section still increases faster than other sections, which means the inflow rate here is still higher than the optimal design requires. Therefore, we need to further control the ICV.

It also shows that the temperature feedback is not instantaneous. It takes days to see whether the temperature at this location still increases faster. This is because of the formation heat resistance, which is a significant effect on the transient temperature behavior
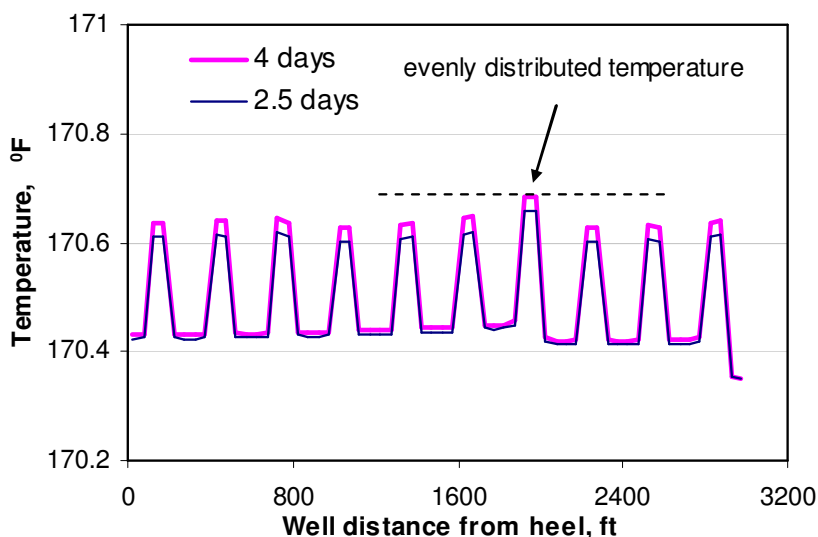
Fig. 5.28 Observe temperature feedback after controlling ICV at high inflow section

At 4.5 days, ICV is operated again with $\gamma = 0.5$, Fig. 5.29 shows the result of temperature and Fig. 5.30 gives the flow rate profiles. Temperature has reached the stable status, but the corresponding rate is still much higher at the high-permeability zone, which indicates that further choking is required at this moment.
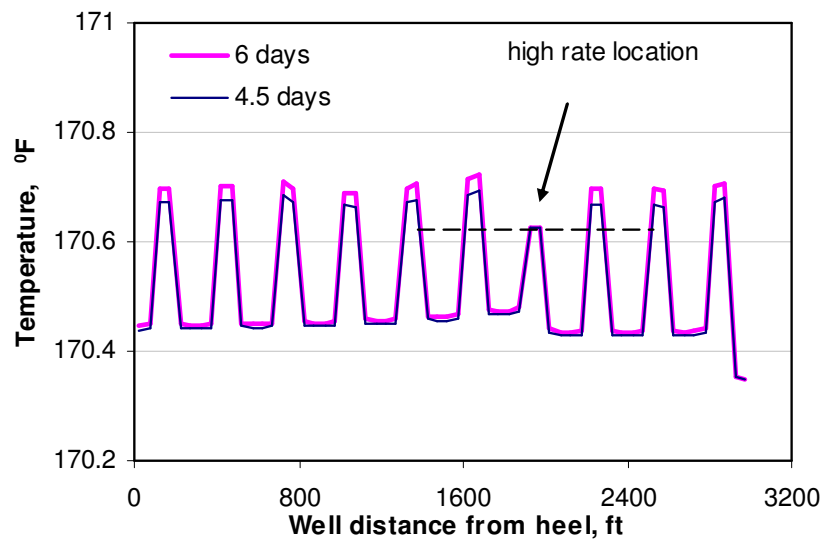
Fig. 5.29 Temperature achieves design at first adjustment
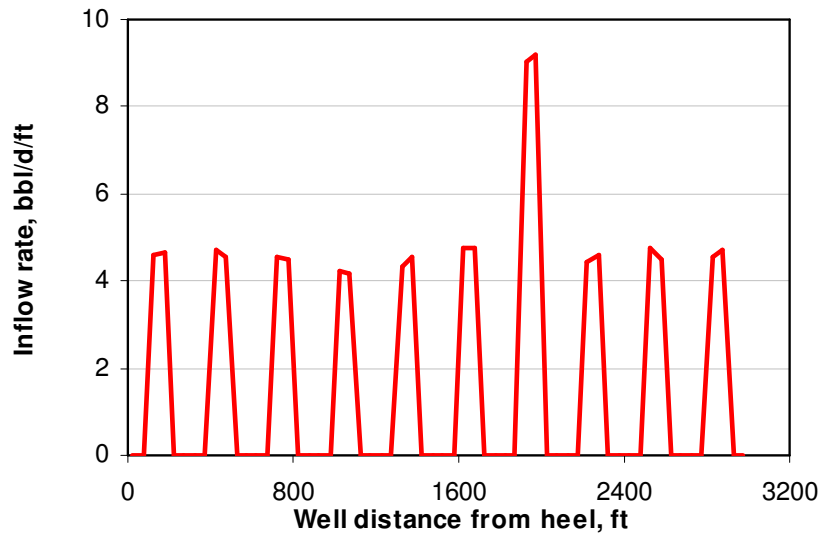
Fig. 5.30 Inflow rate distribution at first adjustment

To achieve a uniform inflow rate distribution in wellbore, the original inflow rate, 16 bbl/d/ft, should be reduced close to 4 bbl/d/ft of other section, as shown in Fig. 5.26. Then the estimated choking off rate at the identified high permeability section is about 0.75 of the original rate. Although the relation between ICV position and flow rate is not linear, we can use this as a guideline. We applied this amount to the ICV (set $\gamma = 0.25$) and let the temperature transient effect to settle down to reach the equilibrium. Fig. 5.31 and Fig. 5.32 show the inflow rate distribution at this status, the temperature stabled at the desired profile, and the flow rate is satisfied as much more even distribution along the wellbore is achieved.
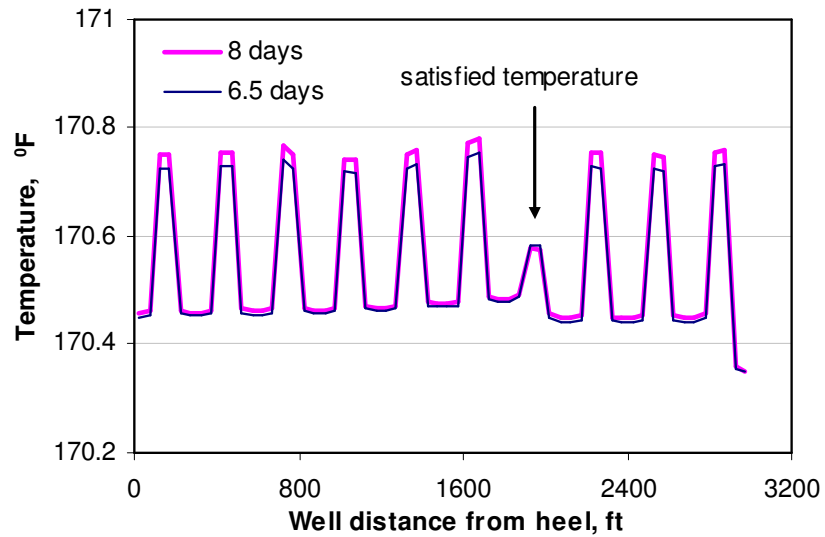
Fig. 5.31 Second ICV operation to meet the desired temperature
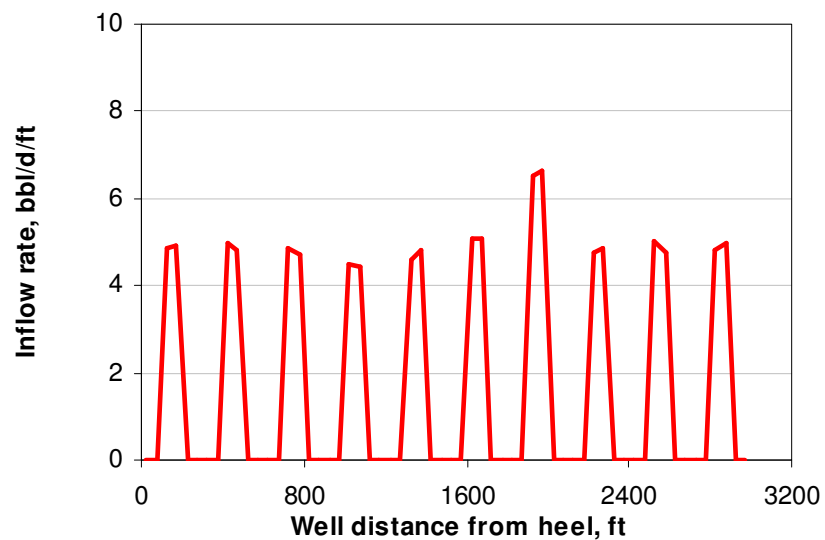
Fig. 5.32 Inflow rate is closed to evenly distribute

The daily oil rate is shown Fig. 5.33, and Fig. 5.34 shows the bottomhole pressure changes as a function of producing time at three conditions: no ICV choking,

initial adjustment with even temperature, and final adjustment with even flow rate. Notice that even though the inflow rate distribution at the final adjustment is closer to the uniform and the higher rate is choked back, its total oil rate is a little higher than the one without ICV control. The procedure of optimizing production by ICVs delayed water breakthrough, as well as increased daily oil rate.
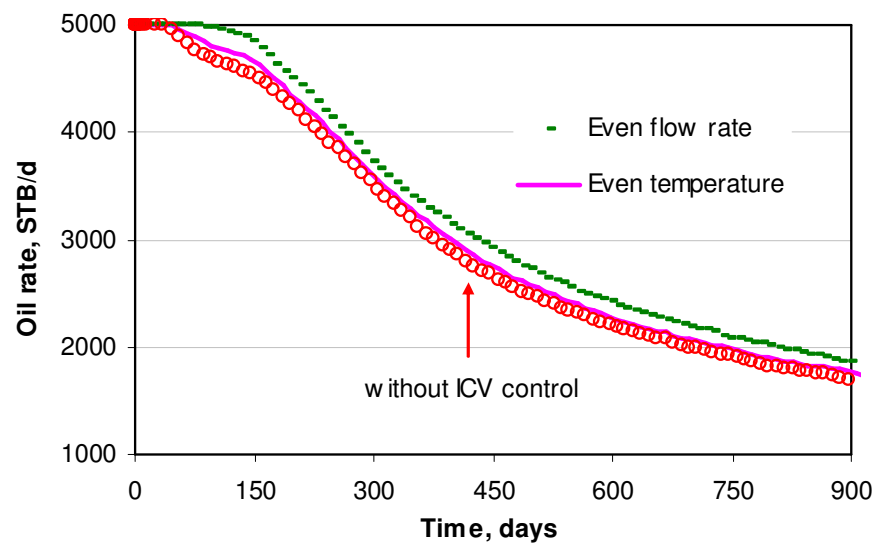
Fig. 5.33 Daily oil rate vs. time at three conditions
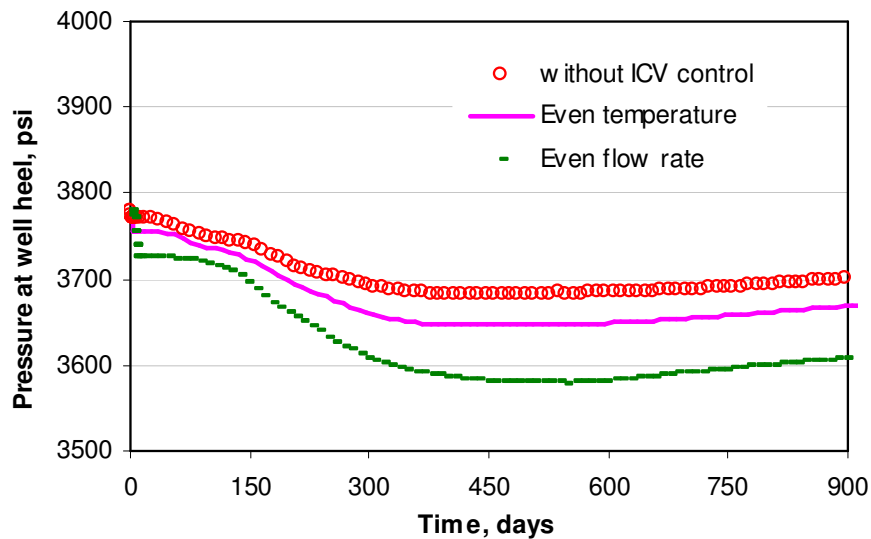
Fig. 5.34 Pressure at heel vs. time at three conditions

Sensor Resolution Effect

Temperature sensor resolution and noise will effect on reading and using the temperature data. To understand their influence on this temperature feedback procedure, this example is further used to study sensor resolution and noise effects. The sensor with higher resolution is better for the application of temperature data because it can identify smaller temperature change. This study exams the effect of sensor with a resolution (denoted by Rs) of 0.05 ^{0}F, which is easy to achieve for recent temperature sensor. Fig. 5.35 is the temperature at initial condition. The high inflow rate section is clearly detected by identifying the high temperature location. Then control the ICV at this section to reduce the inflow rate, using γ=0.25 stages for ICVs. Fig. 5.36 shows the temperature achieves design after operating ICVs at the resolution of 0.05 ^{0}F.
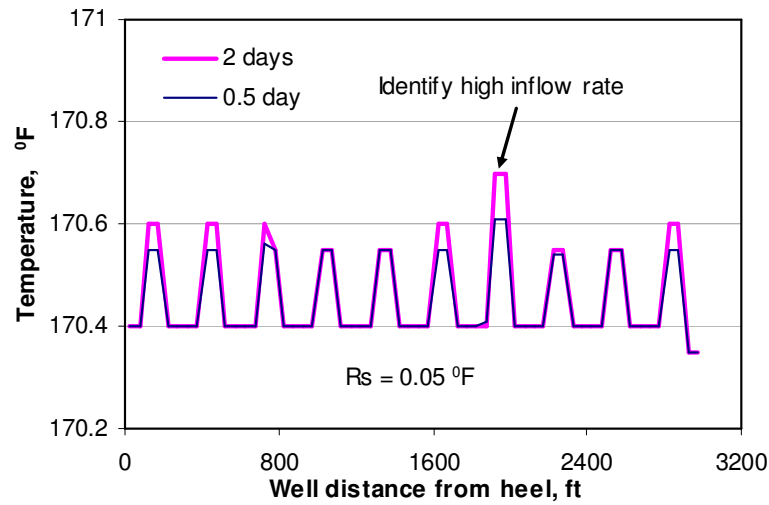
Fig. 5.35 Identify high inflow sections at initial, Rs = 0.05 ^{0}F
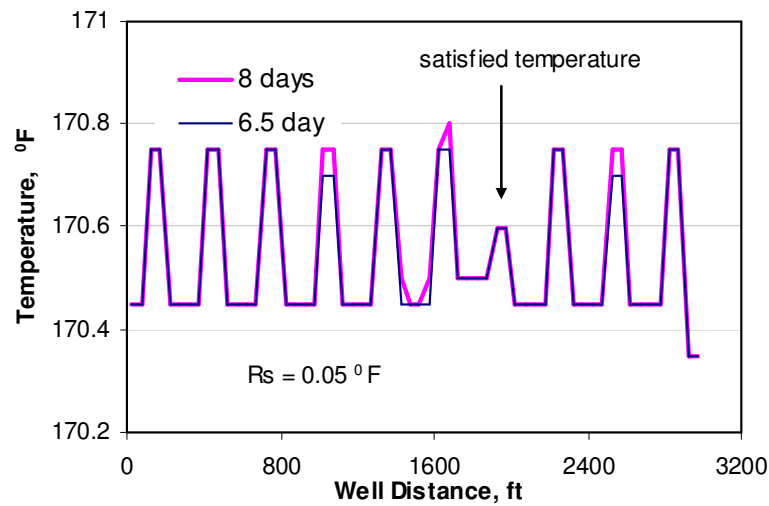
Fig. 5.36 Temperature achieves design, Rs = 0.05 ^{0}F

If the sensor with a resolution of 0.1 ^{0}F, the temperature at 0.5 day can not be used to identify high inflow rate section, as shown in Fig. 5.37. Fig. 5.38 shows that the temperature distribution at 1 day still can not be used.
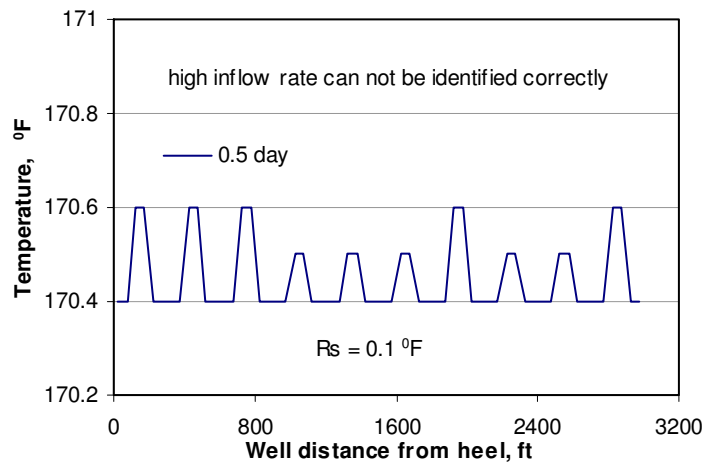
Fig. 5.37 Unable to identify high inflow sections at 0.5 day, Rs = 0.1 ^{0}F
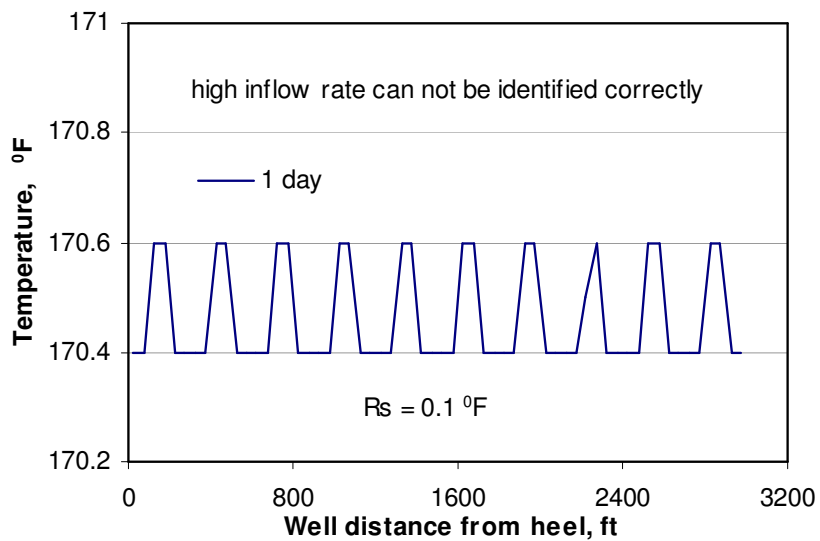
Fig. 5.38 Unable to identify high inflow sections at 1 day, Rs = 0.1 ^{0}F

The temperature data observed at 2 days may be used to identify the high inflow rate, as shown in Fig. 5.39. Operation of ICVs is not applied because the sensor with a resolution of 0.1 ^{0}F is not very successful to identify high inflow rate section.
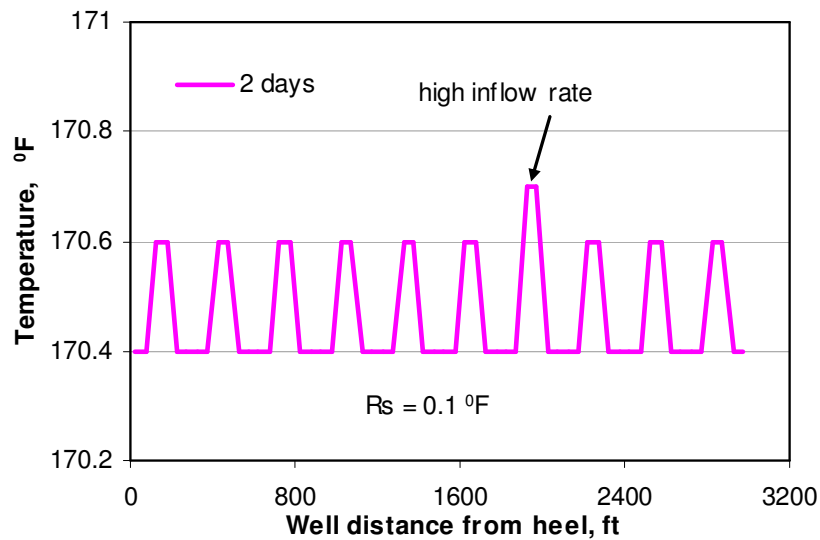
Fig. 5.39 May identify high inflow sections at 2 days, Rs = 0.1 ^{0}F

Noise Effect

The noise of the sensor has bigger effect on the result of the procedure. A normal distribution of noise is introduced to exam its effect on the temperature application. The noise is with zero mean and a variance of σ. Fig. 5.40 shows the temperature at initial condition, and its feedback after ICV operation when the noise variance is 0.033 ^{0}F. The higher temperature zone indicates the higher inflow zone before and after operating the ICVs by temperature feedback, showed in Fig. 5.41. The result shows that the optimization can be applied at this noise level.
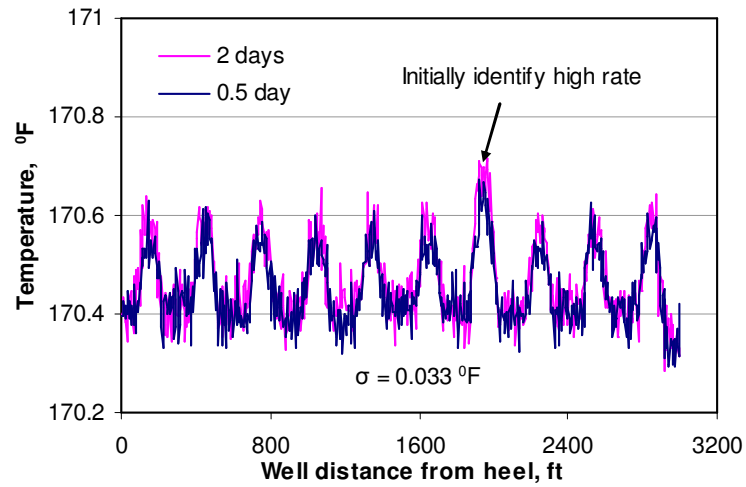
Fig. 5.40 Identify high inflow sections at initial, $\sigma = 0.033\ ^0F$
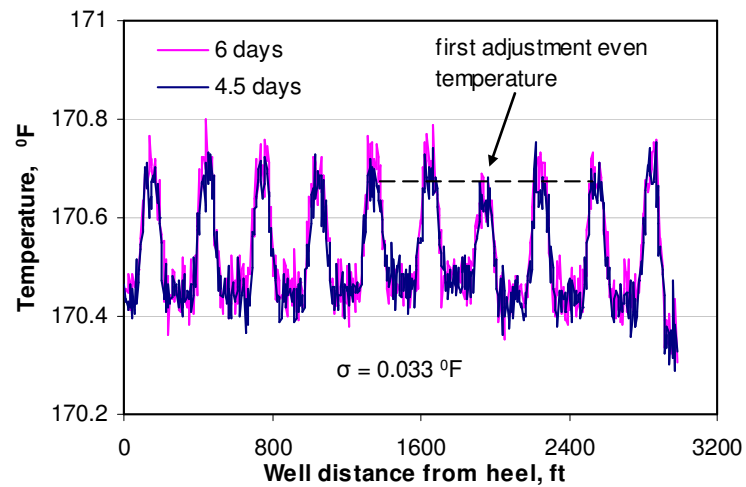
Fig. 5.41 Temperature achieves design, $\sigma = 0.033\ ^0F$

When the noise variance is 0.1 ^0F, the temperature distribution in wellbore are

shown Fig. 5.42 and Fig. 5.43. The result shows that the temperature data fails to detect

inflow rate distribution correctly at this noise level. The procedure cannot be used in this situation.
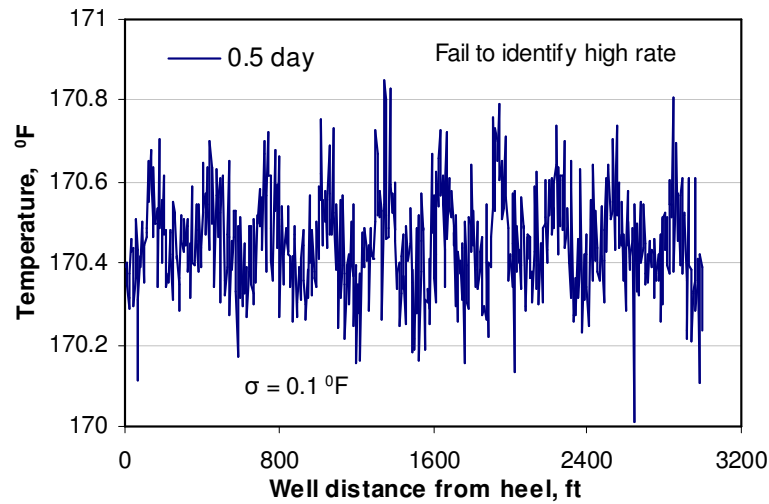
Fig. 5.42 Failure to identify high inflow sections at 0.5 day, $\sigma = 0.1\ ^0F$
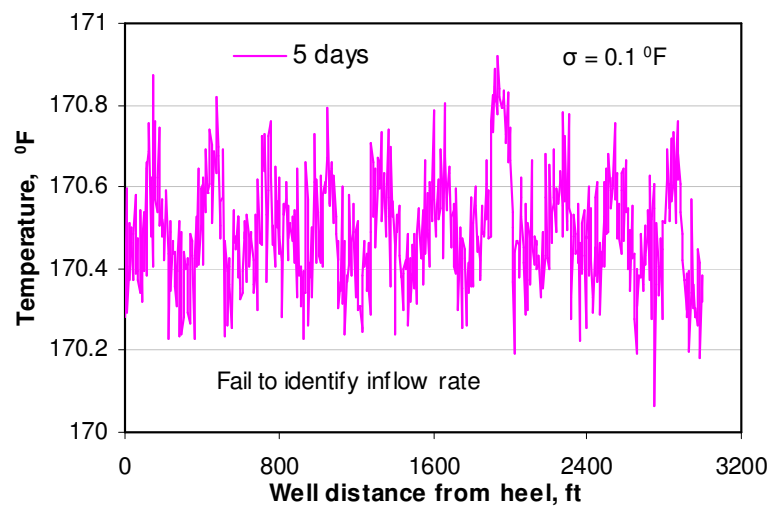
Fig. 5.43 Failure to identify high inflow sections at 5 day, $\sigma = 0.1\ ^0F$

5.2.3 Water Injection in Channel Formation

For the channel formation, Fig. 5.44 shows the reservoir geometry and the 2D permeability distribution which is generated by FLUVSIM (Deutsch and Tran, 2002). The reservoir has an average permeability of 50 md, with a channel in the reservoir only connecting the injector. The channel permeability is 700 md, which may be detected by openhole logging. However, it does not cross with the production well. We may not know the exact structure of this channel in the reservoir.

The reservoir thickness is 50 ft, and the production well and the injection well are located at the middle of the reservoir thickness. The producing well has a constant total liquid rate of 4000 bbl/day initially, and the injection well is at constant pressure 4000 psi, and the injected water temperature is $100\,^0$F.

The same as the previous example, we assumed that the well has 10 sections. Each section has an ICV and a blank pipe to isolate reservoir inflow. Each section is 300-ft long, as shown in Fig. 5.23. Other inputs are kept the same as the previous example.
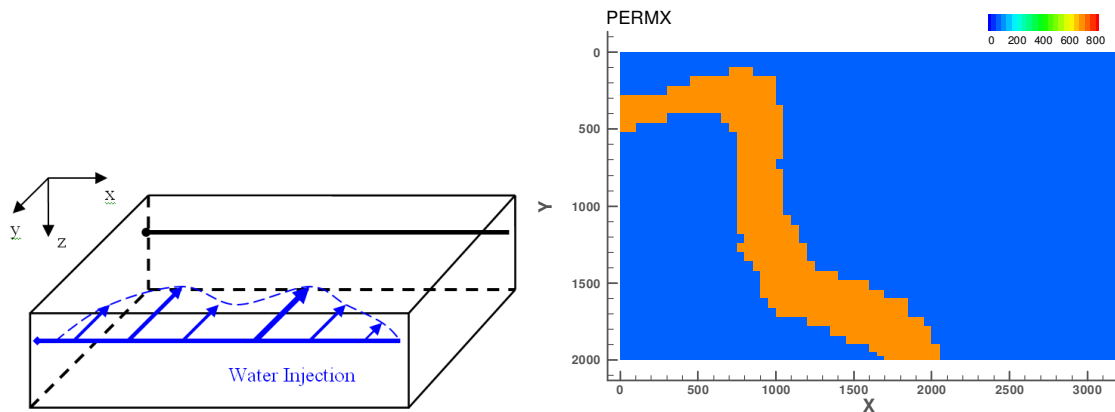
Fig. 5.44 Reservoir geometry and 2D permeability distribution used in example 2

The first step is to use temperature to identify high inflow rate sections. Fig. 5.45 shows the temperature behavior of the producing well. The temperature does not reflect the rate distribution at early time (0.5 days), and the high-temperature section becomes more obvious at 10 day. Thus, we detect the high inflow section from 0 to 1500 ft. The level of temperature increase along the section of 0 to 1500 ft is different, and the inflow rate from 700 ft to 800 ft is the highest. Fig. 5.46 shows the interpreted flow rate profile at initial condition without regulation by ICVs. The permeability heterogeneity will result in an early breakthrough of injected water first at the location of 700 ft to 800 ft, then the entire 1500 ft region towards the heel of the well. This study is to operate the ICVs at the section from 0 to 1500 ft, and monitor the temperature feedback. The adjustment on ICV at each section is different, depending on the observation from the temperature distribution at 10 days. For example, at the range with the highest initial temperature (700-800 ft), it is expected to have a lower temperature than other section after control; and temperature at other sections in the first 1500 ft would be a little higher

than the temperature at 700 - 800 ft section. Thus, the choking ratio γ is the lowest, γ is gradually increasing towards the toe, and γ is one (no choking) from 1800 to 3000 ft. Fig. 5.47 shows the change of ICV position along the wellbore.
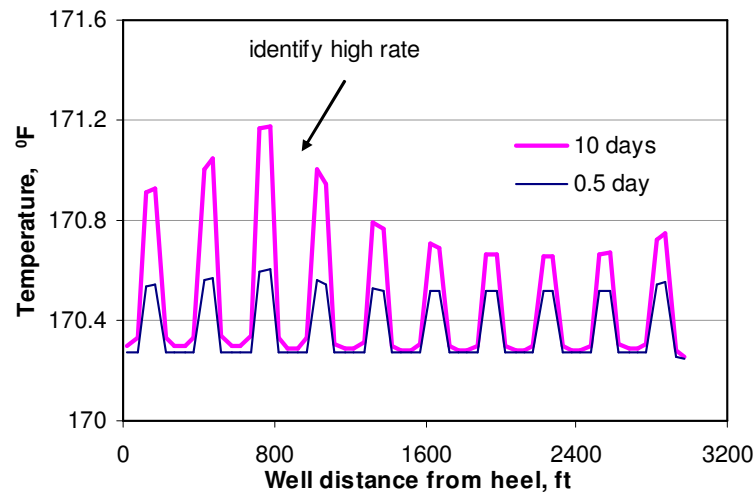
Fig. 5.45 Use temperature to identify inflow rate distribution
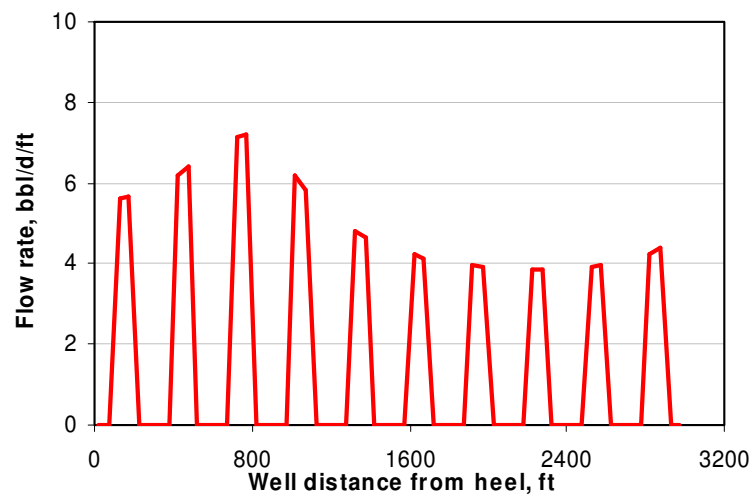
Fig. 5.46 Inflow rate distribution before operating ICV
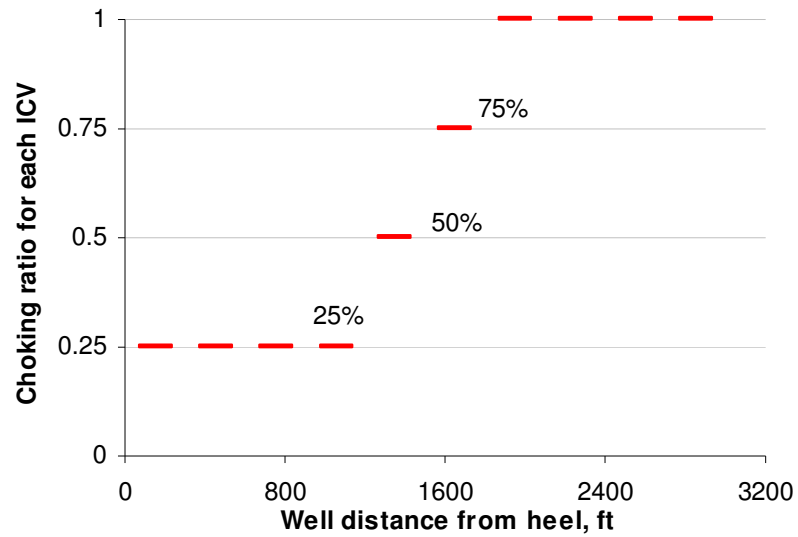
Fig. 5.47 Choking index ratio changes along wellbore

Because the ICV stages are discontinuous, they cannot be set as an arbitrary value. The temperature distribution in Fig. 5.48 does not achieve the desired temperature using the stages in Fig. 5.47. But compared with Fig. 5.45, it is improved. Fig. 5.49 shows that the flow rate distribution along the wellbore at this ICVs setting condition is much more evenly distributed.
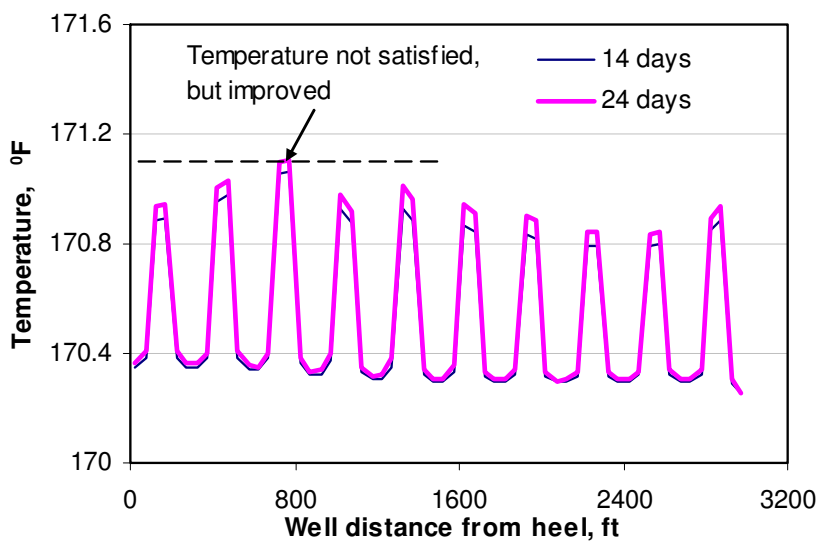
Fig. 5.48 Temperature after ICV operation
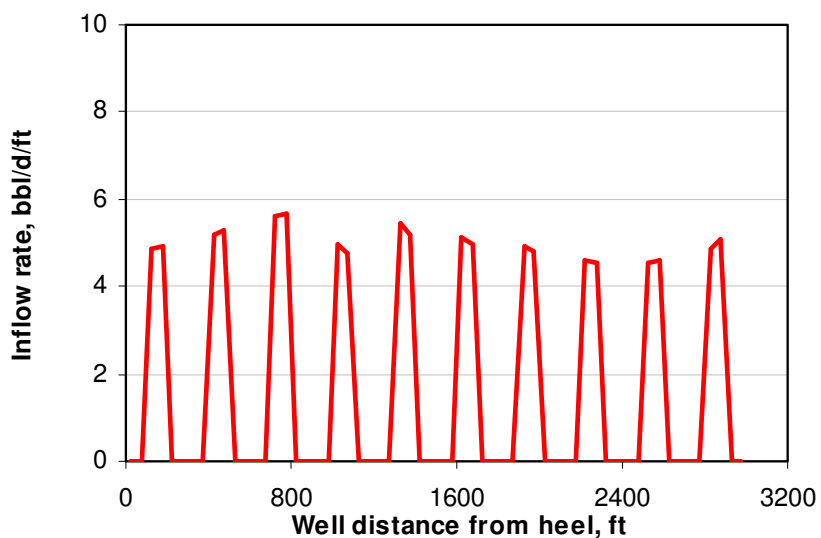
Fig. 5.49 Inflow rate distribution after ICV operation

The procedure presented in this paper helped to improve the well performance. It is realized that we can install ICVs on either or both producing well and injecting well.

Fig. 5.50 shows the predicted inflow rate for this example, including production without ICVs, production with ICVs only on the producer, and production with ICVs on both the producer and the injector. The ICVs setting stages for producing well are mentioned above. At the cross of the channel and the injecting well, the ICVs on injecting well is set to $\gamma=0.25$, which tries to reduce the water comes through the channel.

It is clear that ICVs on the producer is considerably beneficial compared with no ICVs at all. Oil production rate improved significantly in additional to delayed water breakthrough. With the initial temperature information, we may be able to detect the connection between the channel and the injector at 1760 ft to 2000 ft. But meanwhile, adding more ICVs on the injector at this location to control the injection rate does not yield enough further improvement to the production. If considering the complication, cost and risk involved, this is probably not recommended.
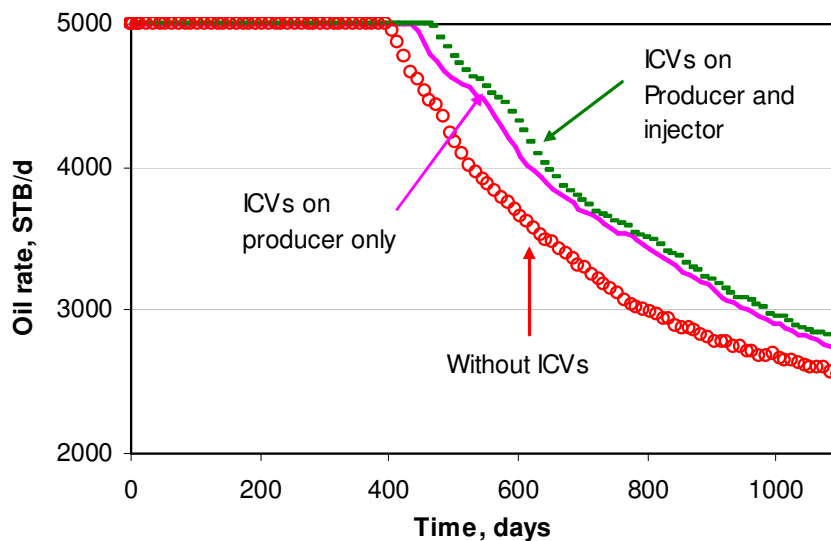
Fig. 5.50 Daily oil rate shows the production improvement

5.3   TEMPERATURE MEASUREMENT ASSISTS RESERVOIR

   CHARACTERIZATION

Most permeability fields contain certain geostatistical characteristics that are much more complicated than just a 1D variation, as shown in Chapter III. However, in Chapter III, the temperature inversion process results in a very coarse-scale estimate of the reservoir permeability distribution. This coarse-scale permeability can cause significant deviation on prediction of reservoir and well performance. For example, from Fig. 4.38, we can see that the simulated water-cut history with the inverted permeability distribution follows the trend of the observed data, but contains a significant mismatch. We can also see that the inverted temperature at the high permeability section increases faster than the observed data (Fig. 4.34). Some of these discrepancies arise from the fact that the inverted permeability is only 1D, which is an approximation of the true 2D permeability field.

Production histories, such as water cut and oil rate, can be collected at the surface. This history data is generally used to update reservoir characteristic. Recently, geologically-based history matching of production data has been used to improve the understanding of reservoir permeability field. A number of techniques have been reported in the literature. Integration of production data typically requires the minimization of a predefined objective function, which consists of data difference between observed and simulated production responses and penalty terms, which preserve the prior information and prevent rough changes. The streamline generalized travel time inversion technique has been proven to be an efficient means for computing parameter

sensitivities (Datta-Gupta et al., 2001; Cheng et al., 2004). This technique uses an analytical approach that involves 1D integral along streamlines to efficiently compute the parameter sensitivities using a single forward simulation, which can be either a streamline or a finite-difference simulator. This kind of history matching approach has been utilized in a large number of field applications (Cheng et al., 2005; Hohl et al., 2006; Rey et al., 2009).

Based on these techniques, we try to generate a high-resolution permeability model, including both temperature and production history information. A coarse-scale permeability distribution is obtained by temperature interpretation, as discussed in Chapter III. Then, the coarse-scale permeability is used as constraints in generating high resolution geological models using geostatistical method, sequential Gaussian simulation with block kriging. Finally, these models are calibrated to production data using streamline-based generalized travel time inversion.

5.3.1   Integrated Approach of Temperature and History Matching

The objective is to incorporate temperature information into geologic modeling and production history matching to better characterize the reservoir. There are two potential approaches, possibly among others. The first one is to incorporate the coarse-scale permeability information as 'secondary' information while constructing the prior geologic model. This model can then be history matched to further update the geologic model. Another approach would be to include the temperature-derived coarse-scale

permeability as a penalty function during the history matching process. The former approach is used here.

The outline of an integrated approach is shown in Fig. 5.51. It combines the temperature interpretation and production history matching for dynamic reservoir characterization and modeling. It includes four major steps as follows:

1. Use of temperature interpretation method to match the observed temperature data, and obtain a coarse-scale permeability distribution.

2. Generating high-resolution geologic model constrained to the coarse-scale permeability estimate. This is accomplished using sequential Gaussian simulation with block kriging, much along the line of seismic data integration into geologic models.

3. Use of the geologic model from step 2 as the prior model for production history matching. The history matching is carried out using a fast streamline-based approach.

4. Use the forward model of wellbore temperature to cross-check that the history matched model reproduces the temperature data. If the updated model reproduces the wellbore temperature measurements within pre-specified tolerance, we accept the refined permeability distribution. Otherwise, we go back to step 2 and repeat the process.
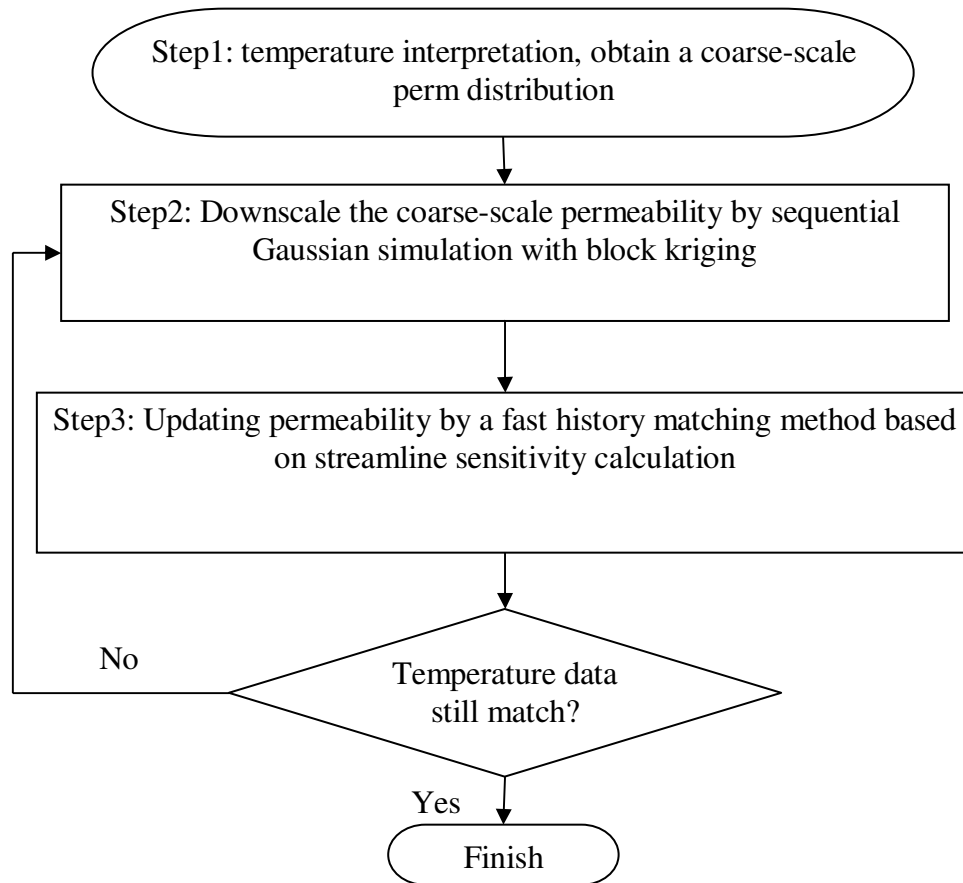
Fig. 5.51 Integrated approach for incorporating temperature data into history matching

5.3.2 Downscaling Method

The objective is to obtain a 2D fine-scale permeability distribution from the 1D coarse-scale permeability which is generated from the temperature inversion. Fig. 5.52 helps us to understand the purpose of this downscaling. In the downscaling process, the known values are the coarse-scale permeability (Fig. 5.52 a). The near wellbore permeability may be also obtained after the openhole logging, for example, permeability can be calculated using porosity provided by openhole logging. The unknown values need to be

determined are the permeability in each reservoir grid, which construct the fine-scale

permeability, as shown in Fig. 5.52 b.

a   b
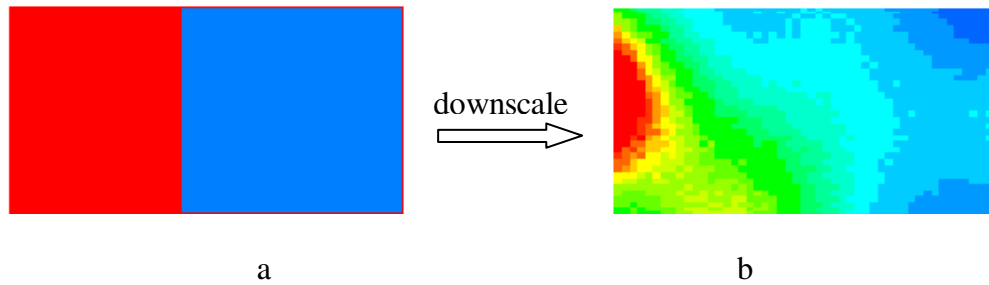
Fig. 5.52 Downscaling of the temperature inverted coarse-scale permeability

Kriging

In geostatistics, kriging is the estimation procedure using known values and location

information to determine unknown values. We use Fig. 5.53 to illustrate the kriging

estimation. Suppose permeabilities at points 1 and 2 are known, and they are 100 md and

200 md respectively. Permeability at point 0 is unknown and need to be determined. The

distance, $l_{10} = 50$ ft, $l_{20} = 100$ ft, and $l_{12} = 130$ ft.
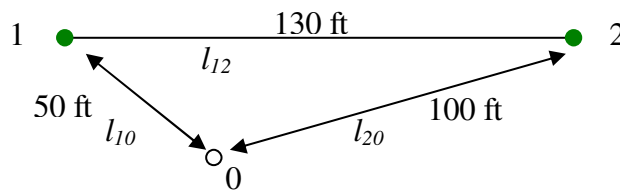
Fig. 5.53 Simple example for kriging estimation

The permeability, k_0, can be linearly estimated from known value, k_1, and k_2 by

$$k_0 = \lambda_1 k_1 + \lambda_2 k_2 + (1 - \lambda_1 - \lambda_2) \cdot m \quad \text{...} \quad (5.5)$$

where λ_1 and λ_2 are weights, and m is mean of k_0.

For λ_1 and λ_2, they are calculated by

$$\begin{aligned} \lambda_1 \cdot \gamma(l_{11}) + \lambda_2 \cdot \gamma(l_{12}) &= \gamma(l_{10}) \\ \lambda_1 \cdot \gamma(l_{12}) + \lambda_2 \cdot \gamma(l_{22}) &= \gamma(l_{20}) \end{aligned} \quad \text{...} \quad (5.6)$$

where γ is a semi-variogram, which can reflect the influence of locations between points. It can be adopted by different models. For example, γ can be given mathematically as

$$\gamma(l) = \begin{cases} c\left(\dfrac{3}{2}\dfrac{l}{a} - \dfrac{1}{2}\dfrac{l^3}{a^3} \right) & l < a \\ c & l \geq a \end{cases} \quad \text{...} \quad (5.7)$$

where c and a are constants which are determined by the known values (samples). This relation is spherical model. For simplification, these constants are set as $c = 1$, $a = 150$ ft.

There are many types of kriging based on how to solve Eq. 5.5. For simple kriging, the mean, m, must be known. For example, if we assume $m = 100$, then using Eq. 5.7 with the distance $l_{10} = 50$, $l_{20} = 100$, and $l_{22} = l_{11} = 0$, $l_{12} = 130$, we can get $\gamma(l_{11}) = \gamma(l_{22}) = 0$, $\gamma(l_{12}) = 0.9745$, $\gamma(l_{10}) = 0.4815$, $\gamma(l_{20}) = 0.8519$. Then substituting these values into Eq. 5.6, we get $\lambda_1 = 0.8742$, $\lambda_2 = 0.4941$. Finally, the permeability, k_0 can be obtained by Eq. 5.5, $k_0 = 149$ md.

For ordinary kriging, $\lambda_1 + \lambda_2 = 1$ is a constraint, the mean, m, is not necessary. This constraint is solved with modified Eq. 5.6 by introducing an unknown, η, called Lagrange multiplier. Then Eq. 5.6 becomes

$$
\begin{aligned}
\lambda_1 \cdot \gamma(l_{11}) + \lambda_2 \cdot \gamma(l_{12}) + \eta &= \gamma(l_{10}) \\
\lambda_1 \cdot \gamma(l_{12}) + \lambda_2 \cdot \gamma(l_{22}) + \eta &= \gamma(l_{20})
\end{aligned}
\quad\text{...} \quad (5.8)
$$

The solution for λ_1 and λ_2 are $\lambda_1 = 0.69$, $\lambda_2 = 0.31$. Therefore, $k_0 = 131$.

In the same time, for ordinary kriging, an estimation variance, σ_0, of this point can be calculated by

$$
\sigma_0{}^2 = \lambda_1 \gamma(l_{10}) + \lambda_2 \gamma(l_{20}) \quad\text{...} \quad (5.9)
$$

It indicates that the estimated value, k_0, should follow a normal distribution.

Reservoir grid can be treated as a block because it is a 3D object. Therefore, block kriging, which estimates the value of a block property from a set of nearby known values using kriging, is used in the downscaling. The estimation procedure is similar to the procedure above.

Sequential Gaussian Simulation

Generally, the result from kriging is very smooth. It may underestimate the heterogeneity. And the kriging result is deterministic. For unknown permeabilities, they may not be determined with certainty. Using stochastic method to describe them may be more reasonable. Therefore, the sequential simulation method with kriging is commonly used in geologic modeling. Because Gaussian (normal) distribution is the most popular

distribution in statistic, sequential Gaussian simulation with block kriging (Behrens et al., 1998) is used for downscaling in this study.

Suppose the reservoir permeability model has N_0 known values at initial, the sequential Gaussian simulation is performed as following steps:

1. Randomly select a reservoir grid, A_1.

2. Perform the kriging procedure based on the N_0 values, obtain an estimated value, k_1^*, for the selected grid, and its variance, σ_1. Then randomly generate k_1 from normal distribution $N(k_1^*, \sigma_1^2)$, and set this k_1 to the reservoir grid, A_1.

3. Include k_1 to the known values, then it has $N_0 + 1$ values. Based on this condition, repeat step 1 and 2, until all interested grids are completed.

After these steps, the sequential Gaussian simulation will generate a permeability distribution based on the known values.

In this study, the coarse-scale permeability distribution from temperature inversion, and permeability near wellbore are known values. The first one is treated as block data, and the second one is treated as point. The kriging estimator, Z_{SK}, conditioned to both point data and block data (Liu and Journel, 2009) is:

$$Z_{SK}(\mathbf{u}) = \mathbf{m}_0 + \Lambda^T \mathbf{D} \quad\text{.. (5.10)}$$

where $\mathbf{u}$ means the point which need to be estimated. $\mathbf{m}_0$ denotes stationary means, and it is a known value. $\mathbf{D}^T = [\mathbf{P}, \mathbf{B}]$ denotes the known data value vector, P denotes data points, B denotes block data, $\Lambda^T = [\lambda_P, \lambda_B]$ denotes the kriging weights for point data P and block data B. And it can be calculated similar to Eq. 5.6.

With this method, the coarse-scale permeability is downscaled and the fine-scale permeability distribution is assigned to reservoir grids. And it also includes the permeability information near wellbore.

5.3.3   Production History Matching

The fine-scale permeability distribution derived from downscaling is now further updated by history matching of production data. This step involves minimization of a least-square difference between the observed data and the calculated response with additional constraints by prior model. In this approach, we have adopted the streamline generalized travel time inversion for history matching, primarily because of its computational efficiency and quasi-linear properties (Cheng et al., 2005).

Suppose the water-cut history is observed, showing in Fig. 5.54 marked with triangles. The water-cut from initial permeability is calculated, showing in Fig. 5.54 marked as the circle in front of the observed data curve. The history matching method is to find an optimal time-shift to minimize the production data difference between observation data and calculated response. It only shifts the initial calculated water-cut history parallelly without changing its shape.

For a well of interest, the optimal shifted time can be obtained from the coefficient of determination, which is given by

$$R^2(\Delta t) = 1 - \frac{\sum_i \left[y^{obs}(t_i) - y^{cal}(t_i + \Delta t) \right]^2}{\sum_i \left[y^{obs}(t_i) - \overline{y^{obs}} \right]^2} \quad \text{...} \quad (5.11)$$

where y is the water cut. The only variable in Eq. 5.11 is Δt, which is the time used to shift the initial calculated water cut. The value of Δt leading the maximum R^2 is called the optimal shifted time, denoted by $\Delta \tilde{t}$. The left plot in Fig. 5.54 shows that with $\Delta \tilde{t}$, the shifted water cut is most close to the observed water cut. The right plot shows the coefficient of determination, R^2, as a function of Δt, and for $\Delta \tilde{t}$, R^2 has the maximum value.
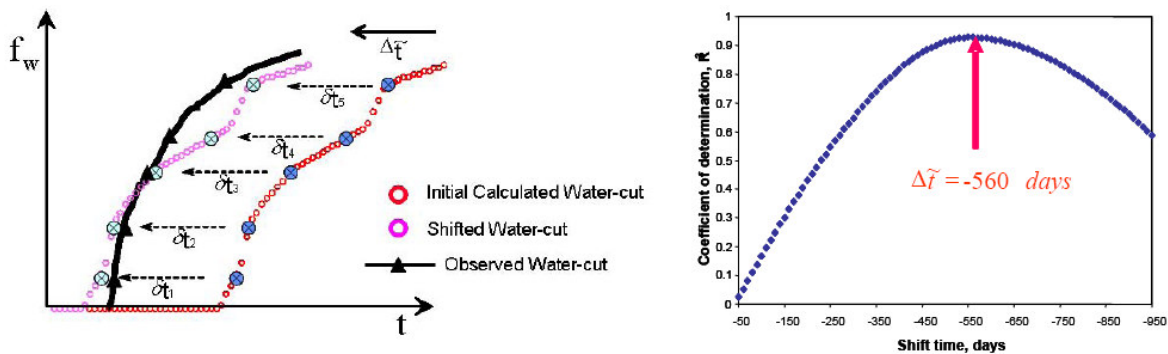
Fig. 5.54 Illustration of generalized travel time difference and correlation function

(Cheng et al., 2004)

Once the optimal shifted time $\Delta \tilde{t}$ is obtained, the next step is to change reservoir parameters to get the new calculated water cut, which is better matching the observed data. In this work, reservoir permeabilities are the parameters to be changed. The changing permeabilities can be determined by

$$\left\| \Delta \tilde{\mathbf{t}} - \mathbf{S} \delta \mathbf{k} \right\| = 0 \quad\text{.. (5.12)}$$

where $\mathbf{S}$ is the sensitivity of shifted time with respect to permeability,

$$\mathbf{S} = \frac{\partial \Delta \tilde{\mathbf{t}}}{\partial \mathbf{k}} \quad\text{.. (5.13)}$$

A critical aspect of production data integration is efficient computation of the sensitivities. We used a streamline-based approach to compute these sensitivities (Cheng et al., 2005; Datta-Gupta and King, 2007). Recall Eq. 2. 23, for two-phase incompressible flow of oil-water in a nondeformable, permeable medium, the transport equation can be written in the streamline time-of-flight coordinates as follows:

$$\frac{\partial S_w}{\partial t} + \frac{\partial F_w}{\partial \tau} = 0 \quad\text{.. (5.14)}$$

where τ represents time of flight which is the travel time along a streamline, ψ, and $s(\mathbf{x})$ is the "slowness" defined as the reciprocal of the total interstitial velocity

$$\tau = \int_\psi s(\mathbf{x}) dx \quad\text{... (5.15)}$$

$$s(\mathbf{x}) = \frac{1}{\left|\mathbf{v}(\mathbf{x})\right|} = \frac{\phi}{k \lambda_{rt} \left|\nabla p\right|} \quad\text{.. (5.16)}$$

where $\mathbf{x}$ is the reservoir grid where the streamline pass through. From Eq. 5.16, we have

$$\frac{\partial s}{\partial k} = -\frac{1}{k^2} \frac{\phi}{\lambda_{rt} \left|\nabla p\right|} = -\frac{s}{k} \quad\text{.. (5.17)}$$

Because changes in reservoir properties are small, it is assumed that streamline paths do not shift significantly. Then, the change in travel time is related to the change in reservoir properties and thus slowness by

$$\delta\tau = \int_\psi \delta s(\mathbf{x})dx = \int_\psi \left(\frac{\partial s}{\partial k} \delta k + \frac{\partial s}{\partial \phi} \delta\phi \right) dx = \int_\psi \left(-\frac{s}{k} \delta k + \frac{\partial s}{\partial \phi} \delta\phi \right) dx \quad \text{.....................} \quad (5.18)$$

In this work, the effective permeability is parameter to calibrate, therefore, $\delta\phi = 0$, and Eq. 5.18 becomes

$$\frac{d\tau}{dk(\mathbf{x})} = -\int_\Sigma \frac{s(\mathbf{x})}{k(\mathbf{x})} dx \quad \text{..} \quad (5.19)$$

which can be further related to arrival time of water front by

$$\frac{\partial t}{\partial k} = \frac{\partial t}{\partial \tau} \frac{d\tau}{dk} \quad \text{..} \quad (5.20)$$

According to Eq. 5.14, and F_w is only a function of S_w, it can be derived that

$$\frac{\partial t}{\partial \tau} = -\frac{\partial S_w}{\partial F_w} = -\frac{1}{dF_w / dS_w} \quad \text{...} \quad (5.21)$$

Therefore, the sensitivity along one streamline can be calculated by integrating the "slowness" from the reservoir grids where the streamline pass through

$$\frac{\partial t}{\partial k} = \frac{\partial t}{\partial \tau} \frac{d\tau}{dk} = -\frac{1}{dF_w / dS_w} \frac{d\tau}{dk} = \frac{1}{dF_w / dS_w} \int_\Sigma \frac{s(\mathbf{x})}{k(\mathbf{x})} dx \quad \text{..................................} \quad (5.22)$$

The overall sensitivity can be calculated by averaged sensitivities for all contributed streamlines at all time steps. Therefore, the sensitivity $\mathbf{S}$ is:

$$\mathbf{S} = \frac{\partial \Delta \tilde{t}}{\partial k} = -\overline{\frac{\partial t}{\partial k}} \quad \text{...} \quad (5.23)$$

Now the sensitivity $\mathbf{S}$ can be used in the production data integration. During this integration, we also want to preserve the initial permeability, and the permeability

changes should be smooth. But Eq. 5.12 cannot achieve this purpose. Therefore, a penalized difference function, $\mathbf{f(\delta k)}$, is given below

$$\mathbf{f(\delta k)} = \left\| \Delta \tilde{\mathbf{t}} - \mathbf{S} \delta \mathbf{k} \right\| + \beta_1 \left\| \delta \mathbf{k} \right\| + \beta_2 \left\| \mathbf{L} \delta \mathbf{k} \right\| \dots\dots\dots (5.24)$$

The permeability change, $\delta \mathbf{k}$, leading a minimum of $\mathbf{f(\delta k)}$, will be adding to the prior permeability in this history matching method. In Eq. 5.24, the first term is the data misfit as quantified by the generalized travel time shift, the second the term is the norm penalty and the third term is the roughness penalty. The norm penalty minimizes the changes to the prior model that already incorporates well and geologic data and also the coarse-scale permeability derived from the temperature data. The roughness penalty ensures that the changes to the model are smooth and large-scale consistent with the low resolution of the production data. The weights β_1 and β_2 determine the relative strengths of the prior model and the roughness term. The minimization of Eq. 5.24 is carried out using an iterative least squares solution approach (Paige and Saunders, 1982). The augmented least-squares system of equations is given as follows

$$\begin{pmatrix} \mathbf{S} \\ \beta_1 \mathbf{I} \\ \beta_2 \mathbf{L} \end{pmatrix} \delta \mathbf{k} = \begin{pmatrix} \Delta \tilde{\mathbf{t}} \\ \mathbf{0} \\ \mathbf{0} \end{pmatrix} \dots\dots\dots (5.25)$$

Eq. 5.25 results in an updated permeability model that matches the production data and also preserves the features of the prior permeability model. By incorporating the norm penalty and staying close to the prior model, we expect that the final updated model will still maintain the matches to the temperature data. We verify this by forward modeling of the wellbore temperature using the final updated permeability. Our

experience shows that for most cases the temperature matches are preserved. In rare cases when the temperature matches are not satisfied within specified tolerance, an alternative would be to start with another realization of the prior permeability distribution obtained from the sequential Gaussian simulation with block kriging.

5.3.4   Application of Approach

We use the synthetic water injection case (section 4.2) as the example. In the previous chapters, it showed that only temperature interpretation can catch the basic information of the reservoir, but the inverted permeability field from temperature is coarse-scale field, and it does not satisfy the production history very well. In this section, the integrated approach is applied to the same example. We first present the result of the integrated approach, and then compare the result with using production history matching only.

Result of Integrated Approach

The temperature inversion of this example is done in section 4.2.2. From temperature inversion, we obtain a coarse-scale permeability distribution. This temperature inverted permeability is shown in Fig. 4.35. The sections of coarse-scale permeability are treated as blocks. At the same time, the permeability near wellbore can be also assigned from the temperature inverted permeability. They are known point data. Then, we generate initial permeability models from sequential Gaussian simulation with block kriging. Finally, for each model, we perform a streamline-based inversion to match the water cut

data at the well. In this way we are able to take into consideration both temperature data and production history. This procedure is summarized in Fig. 5.51.

One realization of permeability distribution resulting from the integrated approach is shown in Fig. 5.55. And Fig. 5.56 through Fig. 5.58 show the corresponding water cut, calculated temperature distribution, and fluid flow rates along the wellbore. Compared with the result by temperature interpretation only, the water-cut history matching has significantly improved, the temperature match is still retained, and the calculated temperature at the high permeability section shows improved behavior. The water entry location is found correctly and the calculated water and oil flow rates in tubing are close to that of the true data.
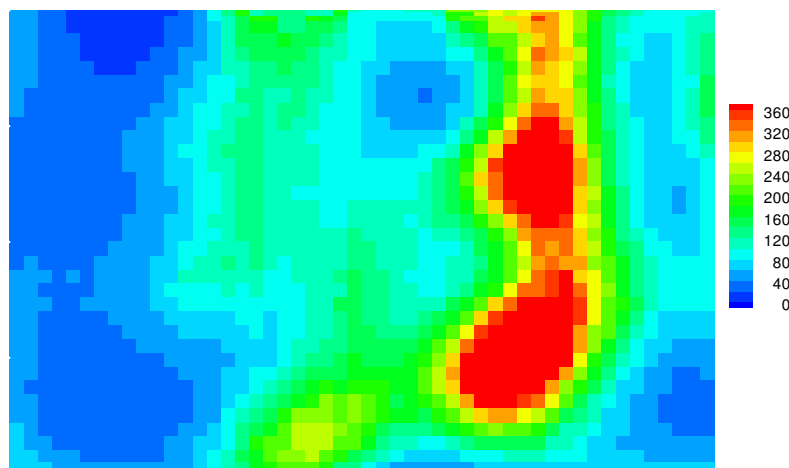
Fig. 5.55 A sample of generated permeability fields from the integrated approach
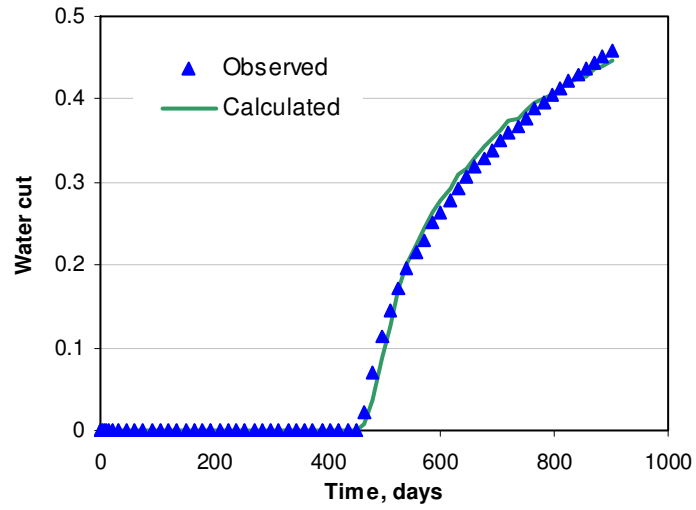
Fig. 5.56 Calculated water-cut history matches observation
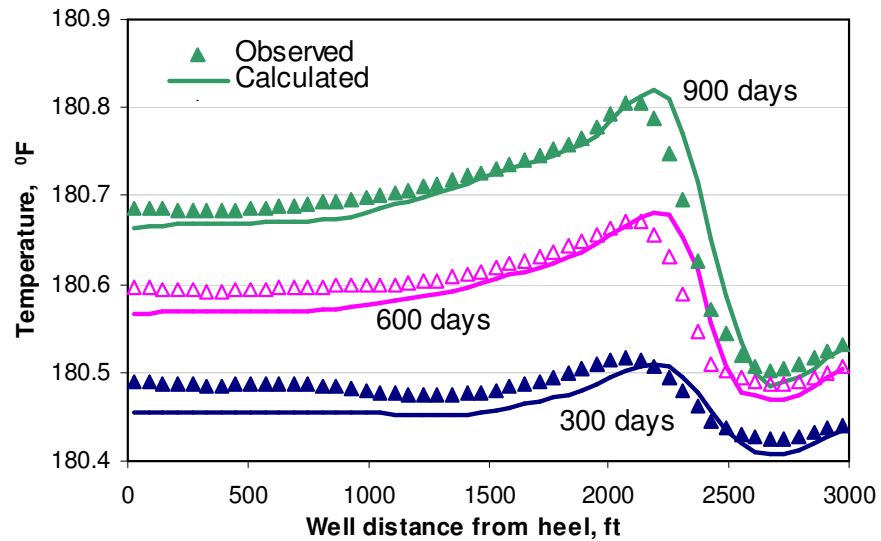
Fig. 5.57 Calculated temperature matches observation
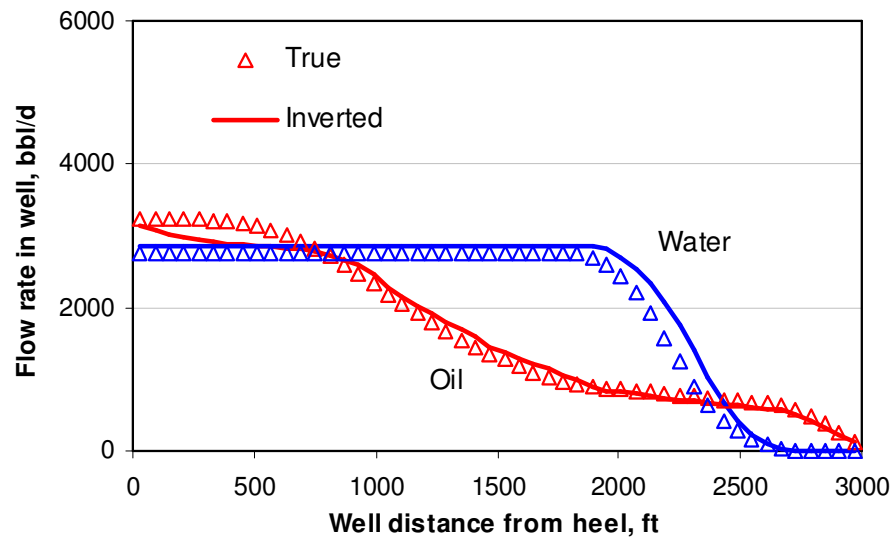
Fig. 5.58 Inverted flow rate profiles in tubing for oil and water

Once we detect the water entry location correctly, we can decide whether we need shut in the water producing zone (2100 to 2460 ft). By shutting in this zone to restrict the water entry, the well performance can be improved.

As a comparison to illustrate the advance of integrating temperature information for reservoir characterization, we show the history matching only. The only known data is the near wellbore permeability, which can be provided by openhole logging or interpretation. The temperature inverted permeability at the wellbore is assigned as the known value for the downscale. Then initial permeability model is generated using sequential Gaussian simulation with well permeability only and no secondary constrain. The permeability distribution is then updated using the water-cut data of the well at the surface.

Water-cut history matching results are shown in Fig. 5.59, where only production history is considered. There are more than one solutions that satisfy the convergence criteria. We plot two matched curves, and the corresponding permeability fields are shown in Fig. 5.60.
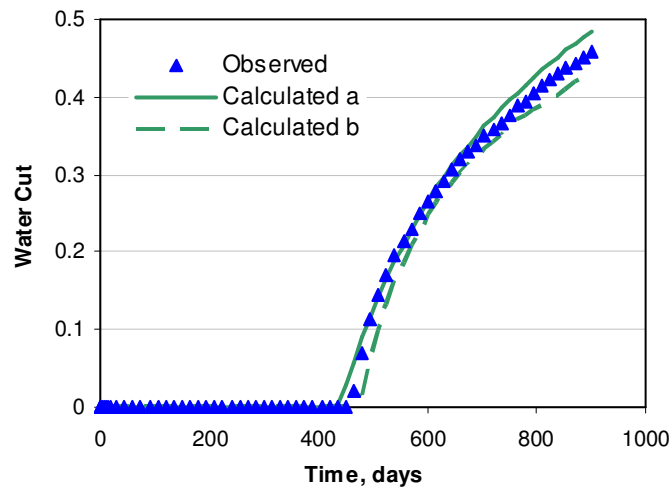
Fig. 5.59 Matching water-cut history

a   b
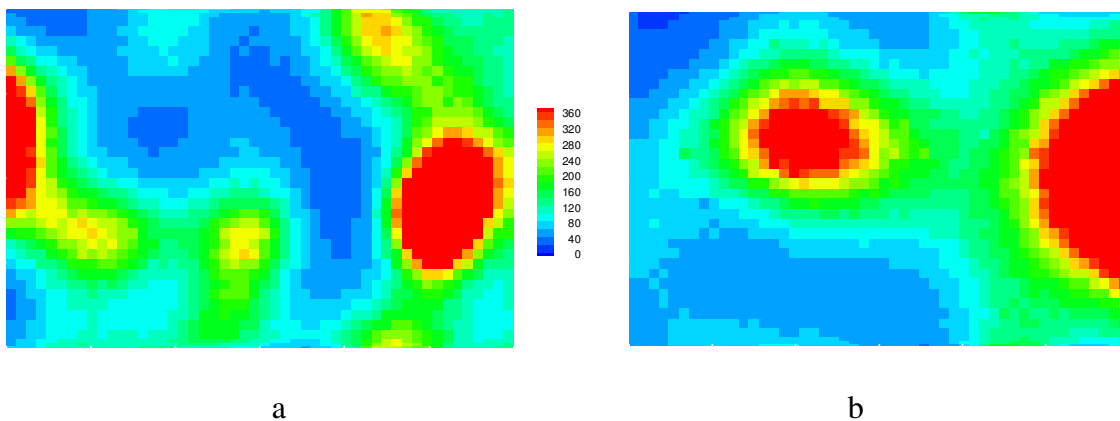
Fig. 5.60 Permeability distributions derived from water cut and well data only

From Fig. 5.59 we observed a satisfied production history matching with the permeability presented in Fig. 5.60. If we bring the temperature information in, we add new constraint to the matching. Fig. 5.61 shows the temperature calculated from the permeability field in Fig. 5.60 a. Obviously, the calculated temperature has intolerable deviation from the observed temperature, so does the flow rates distribution along the wellbore (Fig. 5.62), indicating clearly the error in permeability field estimation.
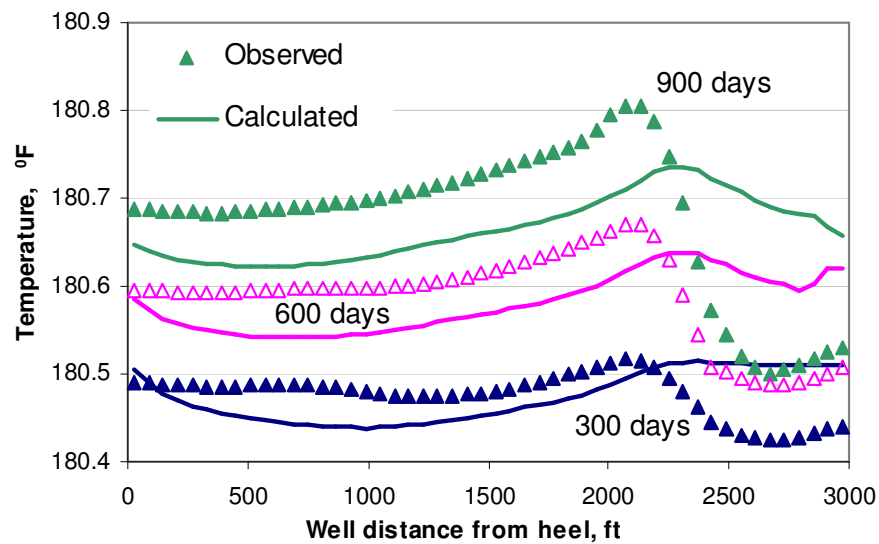
Fig. 5.61 Calculated temperature fails to match observation
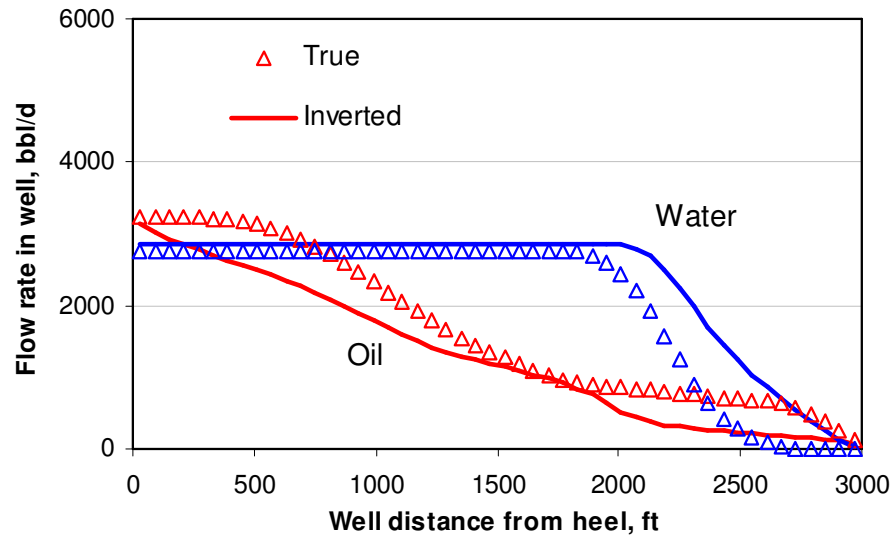
Fig. 5.62 Downhole flow rates may not be predicted correctly by history matching only

The procedure of combining the temperature interpretation method and production history matching has flexibility in generating reservoir characteristics and horizontal well flow conditions. The results show that the downhole temperature measurements can improve the understanding of reservoir characteristics. The outcome is a geologic model that is consistent with the prior static model and dynamic information, and also the wellbore temperature measurements. The updated model can then be used to predict the downhole flow conditions in the horizontal well operation.

CHAPTER VI

CONCLUSIONS

In this study, a methodology has been developed, which can be used to interpret temperature and pressure data measured by downhole sensors to downhole flow conditions. The approach uses a forward model to predict the transient temperature, and pressure based on given flow distribution of horizontal wells, and an inverse model to estimate the flow profile from temperature and pressure by minimize the objective function of difference between calculated and observed data. The method has been applied to examples at field conditions successfully. It is concluded from this study that:

1. The 3D transient flow simulation of reservoir flow and temperature is more flexible than the previously developed steady-state, 1D model. The simulated flow field as a function of producing time improves our understanding of downhole flow condition.

2. The transient flow effect on temperature behavior can provide additional information of locating of water or gas entries. This information can be used as preliminary screening of permeability variation along the wellbore.

3. Examples explain the detailed procedure of identifying water entry location and the effect of reservoir heterogeneity on early water breakthrough by the developed method. The method located water entry and water flow rate with a satisfied accuracy.

4. Using temperature feedback to operate ICV to achieve an optimized production

is valuable for reservoir/well performance optimization. A desired temperature profile can be generated by the method introduced in this work, which will yield an evenly distributed flow profile along a horizontal wellbore, and therefore to improve downhole flow condition.

5. Finally, temperature data can be extent to reservoir characterization and optimization. The procedure combines the temperature interpretation method and production history matching to generate reservoir characteristics and horizontal well flow conditions. The results show that the integrated downhole temperature inversion and history matching can improve the understanding of reservoir characteristics with a better resolution. It clearly demonstrates the benefits of the approach over either the temperature interpretation only or the production history matching only.

REFERENCES

Alaeddin, E. and Maizeret, P.-D. 2003. Using Production Logging Technology for Reservoir Management in the Persian Gulf. Paper SPE 85667 presented at Nigeria Annual International Conference and Exhibition, Abuja, Nigeria, 4-6 August. doi: 10.2118/85667-MS.

Alghareeb, Z. M., Horne, R. N., Yuen, B. B. and Shenawi, S. H. 2009. Proactive Optimization of Oil Recovery in Multilateral Wells Using Real Time Production Data. Paper SPE 124999 presented at SPE Annual Technical Conference and Exhibition, New Orleans, Louisiana, 4-7 October. doi: 10.2118/124999-MS.

Alhuthali, A. H., Oyerinde, D. and Datta-Gupta, A. 2007. Optimal Waterflood Management Using Rate Control. *SPE Reservoir Evaluation & Engineering* **10** (5): 539-551. doi: 10.2118/102478-PA.

Behrens, R. A., MacLeod, M. K., Tran, T. T. and Alimi, A. C. 1998. Incorporating Seismic Attribute Maps in 3D Reservoir Models. *SPE Reservoir Evaluation & Engineering* **1** (2): 122-126. doi: 10.2118/36499-PA.

Brady, J. L., Watson, B. A., Warner, D. W., North, R. J., Sommer, D. M., Colson, J. L., Kleinberg, R. L., Wolcott, D. S. and Sezginer, A. 1998. Improved Production Log Interpretation in Horizontal Wells Using a Combination of Pulsed Neutron Logs, Quantitative Temperature Log Analysis, Time Lapse LWD Resistivity Logs and Borehole Gravity. Paper SPE 48851 presented at SPE International Oil and Gas Conference and Exhibition in China, Beijing, China, 2-6 November. doi: 10.2118/48851-MS.

Carnegie, A., Roberts, N. and Clyne, I. 1998. Application of New Generation Technology to Horizontal Well Production Logging - Examples from the North West Shelf of Australia. Paper SPE 50178 presented at SPE Asia Pacific Oil and Gas Conference and Exhibition, Perth, Australia, 12-14 October 1998. doi: 10.2118/50178-MS.

Chace, D., Wang, J., Mirzwinski, R., Maxit, J. and Trcka, D. 2000. Applications of a New Multiple Sensor Production Logging System for Horizontal and Highly-Deviated Multiphase Producers. Paper SPE 63141 presented at SPE Annual Technical Conference and Exhibition, Dallas, Texas, 1-4 October doi: 10.2118/63141-MS.

Chen, N. H. 1979. An Explicit Equation for Friction Factor in Pipe. *Ind. Eng. Chem. Fund.* **18** (3): 296.

Cheng, H., Datta-Gupta, A. and He, Z. 2005. A Comparison of Travel-Time and Amplitude Matching for Field-Scale Production-Data Integration: Sensitivity,

Nonlinearity, and Practical Implications. *SPE Journal* **10** (1): 75-90. doi: 10.2118/84570-PA.

Cheng, H., Wen, X.-H., Milliken, W. J. and Datta-Gupta, A. 2004. Field Experiences with Assisted and Automatic History Matching Using Streamline Models. Paper SPE 89857 presented at SPE Annual Technical Conference and Exhibition, Houston, Texas, 26-29 September. doi: 10.2118/89857-MS.

Datta-Gupta, A. and King, M. J. 2007. *Streamline Simulation: Theory and Practice,* Textbook Series, SPE, Richardson, Texas **11:** 19, 48-51.

Datta-Gupta, A., Kulkarni, K. N., Yoon, S. and Vasco, D. W. 2001. Streamlines, Ray Tracing and Production Tomography: Generalization to Compressible Flow. *Petroleum Geoscience* **7** (S): S75-S86.

Deutsch, C. V. and Tran, T. T. 2002. FLUVSIM: A Program for Object-Based Stochastic Modeling of Fluvial Depositional Systems. *Computers & Geosciences* **28** (4): 525-535. doi: 10.1016/S0098-3004(01)00075-9.

Donovan, G., P.E., Dria, D., Ugueto, G. and Gysen, A. 2008. Improved Production Profiling Using Thermal Balance and Statistical Modeling in the Pinedale Anticline of the US Rocky Mountains. Paper SPE 115034 presented at SPE Annual Technical Conference and Exhibition, Denver, Colorado, 21-24 September. doi:10.2118/115034-MS.

Dranchuk, P. M. and Abou-Kassem. 1975. Calculation of z-Factors for Natural Gases Using Equations of State. *Journal of Canada Petroleum Technology* **14** (3): 34-36.

Duru, O. and Horne, R. N. 2008. Modeling Reservoir Temperature Transients and Matching to Permanent Downhole Gauge Data for Reservoir Parameter Estimation. Paper SPE 115791 presented at SPE Annual Technical Conference and Exhibition, Denver, Colorado, 21-24 September. doi: 10.2118/115791-MS.

Foucault, H., Poilleux, D., Djurisic, A., Slikas, M., Strand, J. and Silva, R. 2004. A Successful Experience for Fiber Optic and Water Shut Off on Horizontal Wells with Slotted Liner Completion in an Extra Heavy Oil field. Paper SPE 89405 presented at SPE/DOE Symposium on Improved Oil Recovery, Tulsa, Oklahoma, 17-21 April. doi:10.2118/89405-MS.

Frankenburg, A., Bartel, P., Roberts, G. and Hupp, D. 2000. Gas Shutoff Evaluation and Implementation, North Slope, Alaska. Paper SPE 62892 presented at SPE Annual Technical Conference and Exhibition, Dallas, Texas, 1-4 October. doi: 10.2118/62892-MS.

FrontSim 2008. S. G. R. T. Reference Manual, 2008.

Fryer, V., ShuXing, D., Otsubo, Y., Brown, G. and Guilfoyle, P. 2005. Monitoring of Real-Time Temperature Profiles Across Multizone Reservoirs during Production and Shut in Periods Using Permanent Fiber-Optic Distributed

Temperature Systems. Paper SPE presented at SPE Asia Pacific Oil and Gas Conference and Exhibition, Jakarta, Indonesia, 5-7 April 2005. doi:10.2118/92962-MS.

Furui, K., Zhu, D. and Hill, A. D. 2003. A Rigorous Formation Damage Skin Factor and Reservoir Inflow Model for a Horizontal Well. *SPE Production & Facilities* **18** (3): 151-157. doi: 10.2118/84964-PA.

Hasan, A. R. and Kabir, C. S. 1994. Aspects of Wellbore Heat Transfer During Two-Phase Flow *SPE Production & Facilities* **9** (3): 211-216. doi: 10.2118/22948-PA.

Heddleston, D. 2009. Horizontal Well Production Logging Deployment and Measurement Techniques for US Land Shale Hydrocarbon Plays. Paper SPE 120591 presented at SPE Production and Operations Symposium, Oklahoma City, Oklahoma, 4-8 April. 10.2118/120591-MS.

Hill, A. D. 1990. *Production Logging -Theoretical and Interpretive Elements,* Monograph Series, SPE, Richardson, Texas **14:** 28-29.

Hohl, D., Jimenez, E. and Datta-Gupta, A. 2006. Field Experiences With History Matching an Offshore Turbiditic Reservoir Using Inverse Modeling. Paper SPE 101983 presented at SPE Annual Technical Conference and Exhibition, San Antonio, Texas, 24-27 September. doi: 10.2118/101983-MS.

Huckabee, P. 2009. Optic Fiber Distributed Temperature for Fracture Stimulation Diagnostics and Well Performance Evaluation. Paper SPE presented at SPE Hydraulic Fracturing Technology Conference, The Woodlands, Texas, 19-21 January. doi: 10.2118/118831-MS.

Huebsch, H., Moss, M., Trilsbeck, T., Brown, G., Rogers, S. and Bouchard, T. 2008. Monitoring Inflow Distribution in Multi-zone, Velocity String Gas Wells Using Slickline Deployed Fiber Optic Distributed Temperature Measurements. Paper SPE 115816 presented at SPE Annual Technical Conference and Exhibition, Denver, Colorado, USA, 21-24 September doi:10.2118/115816-MS.

Izgec, B., Kabir, C. S., Zhu, D. and Hasan, A. R. 2006. Transient Fluid and Heat Flow Modeling in Coupled Wellbore/Reservoir Systems. *SPE Reservoir Evaluation & Engineering* **10** (3): 294-301. doi: 10.2118/102070-PA.

Jayawardena, S. S., Alkaya, B. R. and Brill, C. L. 2000. A New Model for Dispersed Multi-Layer Oil-Water Flow. *BHR Group Conference Series Publication* **40**: 77-90.

Jerauld, G. R. 1997. General Three-Phase Relative Permeability Model for Prudhoe Bay *SPE Reservoir Engineering* **12** (4): 255-263. doi: 10.2118/36178-PA.

Johnson, D., Sierra, J., Kaura, J. and Gualtieri, D. 2006. Successful Flow Profiling of Gas Wells Using Distributed Temperature Sensing Data. Paper SPE 103097

presented at SPE Annual Technical Conference and Exhibition, San Antonio, Texas, USA, 24-27 September. doi:10.2118/103097-MS.

Johnson, E. F., Bossler, D. P. and Naumann, V. O. 1959. Calculation of Relative Permeability from Displacement Experiments. *Petroleum Transactions, AIME* **216**: 370-372.

Julian, J. Y., King, G. E., Cismoski, D. A., Younger, R. O., Brown, D. L., Brown, G. A., Richards, K. M., Meyer, C. A., Sierra, J. R., Leckband, W. T., Sack, J. K. and Julian, F. C. 2007. Downhole Leak Determination Using Fiber-Optic Distributed-Temperature Surveys at Prudhoe Bay, Alaska. Paper SPE 107070 presented at SPE Annual Technical Conference and Exhibition, Anaheim, California, 11-14 November doi: 10.2118/107070-MS.

Kabir, C. S., Hasan, A. R., Jordan, D. L. and Wang, X. 1996. A Wellbore/Reservoir Simulator for Testing Gas Wells in High-Temperature Reservoirs *SPE Formation Evaluation* **11** (2): 128-134. doi: 10.2118/28402-PA.

Lake, L. W. 1989. *Enhanced Oil Recovery*. Englewood Cliffs, New Jersy: Prentice Hall.

Liu, Y. and Journel, A. G. 2009. A package for geostatistical integration of coarse and fine scale data. *Computers & Geosciences* **35** (3): 527-547. doi: 10.1016/j.cageo.2007.12.015.

Ma, X., Al-Harbi, M., Datta-Gupta, A. and Efendiev, Y. 2008. An Efficient Two-Stage Sampling Method for Uncertainty Quantification in History Matching Geological Models. *SPE Journal* **13** (1): 77-87. doi: 10.2118/102476-PA

Maubeuge, F., Eric, A. and Bertrand, O. 1994. MOTHER: A Model for Interpreting Thermometrics. Paper SPE 28588 presented at SPE Annual Technical Conference and Exhibition, New Orleans, Louisiana, 25-28 September doi: 10.2118/28588-MS.

Muradov, K. M. and Davies, D. R. 2008. Prediction of Temperature Distribution in Intelligent Wells. Paper SPE 114772 presented at SPE Russian Oil and Gas Technical Conference and Exhibition, Moscow, Russia, 28-30 October. doi: 10.2118/114772-MS.

Muradov, K. M. and Davies, D. R. 2009. Temperature Modeling and Analysis of Wells with Advanced Completion. Paper SPE 121054 presented at EUROPEC/EAGE Conference and Exhibition, Amsterdam, The Netherlands, 8-11 June. doi: 10.2118/121054-MS.

Oliver, D. S., Cunha, L. B. and Reynolds, A. C. 1997. Markov chain Monte Carlo methods for conditioning a permeability field to pressure data. *Mathematical Geology* **29** (1): 61-91. doi: 10.1007/BF02769620

Ouyang, L.-B., Arbabi, S. and Aziz, K. 1998. General Wellbore Flow Model for Horizontal, Vertical, and Slanted Well Completions. *SPE Journal* **3** (2): 124-133. doi: 10.2118/36608-PA.

Ouyang, L.-B. and Aziz, K. 2000. A Homogeneous Model for Gas-Liquid Flow in Horizontal Wells. Journal of Petroleum Science&Engineering 27 (3-4): 119-128. doi: 10.1016/S0920-4105(00)00053-X.

Ouyang, L.-B. and Belanger, D. 2006. Flow Profiling by Distributed Temperature Sensor (DTS) System—Expectation and Reality. *SPE Production & Operations* **21** (2): 269-281. doi: 10.2118/90541-PA.

Paige, C. C. and Saunders, M. A. 1982. An Algorithm for Sparse Linear Equations and Sparse Least Squares. *ACM Transactions on Mathematical Software* **8** (1): 43-71. doi: 10.1145/355984.355989.

Peaceman, D. W. 1983. Interpretation of Well-Block Pressures in Numerical Reservoir Simulation With Nonsquare Grid Blocks and Anisotropic Permeability. *SPE Journal* **23** (3): 531-543. doi: 10.2118/10528-PA.

Perkins, T. K. 1993. Critical and Subcritical Flow of Multiphase Mixtures Through Chokes. *SPE Drilling & Completion* **8** (4): 271-276. doi: 10.2118/20633-PA

Pinzon, I. D., Davies, J. E., Mammadkhan, F. and Brown, G. A. 2007. Monitoring Production From Gravel-Packed Sand-Screen Completions on BP's Azeri Field Wells Using Permanently Installed Distributed Temperature Sensors. Paper SPE 110064 presented at SPE Annual Technical Conference and Exhibition, Anaheim, California, USA, 11-14 November. doi:10.2118/110064-MS.

Pollock, D. W. 1988. Semeanalytical Computation of Path Lines for Finite-Difference Models. *Ground Water* **26** (6): 743-750.

Qing, Y. and Davies, D. R. 2009. A Generalized Predictive Control for Management of an Intelligent Well's Downhole, Interval Control Valves—Design and Practical Implementation. Paper SPE 123682 presented at Offshore Europe, Aberdeen, UK, 8-11 September. doi: 10.2118/123682-MS.

Ramey, H. J. 1962. Wellbore Heat Transmission. *Journal of Petroleum Technology* **14** (4): 427-435. doi: 10.2118/96-PA.

Rey, A., Ballin, P. R., Vitalis, C. F., Parke, J. and Datta-Gupta, A. 2009. Assisted History Matching in an Offshore Turbidite Reservoir With Active Reservoir Management. Paper SPE 124950 presented at SPE Annual Technical Conference and Exhibition, New Orleans, Louisiana, 4-7 October. doi: 10.2118/124950-MS.

Sagar, R., Doty, D. R. and Schmidt, Z. 1991. Predicting Temperature Profiles in a Flowing Well *SPE Production Engineering* **6** (4): 441-448. doi: 10.2118/19702-PA.

Satter, A. 1965. Heat Losses During Flow of Steam Down a Wellbore. *Journal of Petroleum Technology* **17** (7): 845-851. doi: 10.2118/1071-PA.

Sui, W. 2009. Determining Multilayer Formation Properties from Transient Temperature and Pressure Measurements. PhD thesis, Texas A&M Univeristy, College Station, Texas.

Sui, W., Zhu, D., Hill, A. D. and Ehlig-Economides, C. A. 2008a. Determining Multilayer Formation Properties From Transient Temperature and Pressure Measurements. Paper SPE 116270 presented at SPE Annual Technical Conference and Exhibition, Denver, Colorado, USA, 21-24 September. doi:10.2118/116270-MS.

Sui, W., Zhu, D., Hill, A. D. and Ehlig-Economides, C. A. 2008b. Model for Transient Temperature and Pressure Behavior in Commingled Vertical Wells. Paper SPE 115200 presented at SPE Russian Oil and Gas Technical Conference and Exhibition, Moscow, Russia, 28-30 October. doi:10.2118/115200-MS.

Wang, X., Lee, J., Thigpen, B., Vachon, G., Poland, S. and Norton, D. 2008. Modeling Flow Profile Using Distributed Temperature Sensor (DTS) System. Paper SPE presented at Intelligent Energy Conference and Exhibition, Amsterdam, The Netherlands, 25-27 February doi: 10.2118/111790-MS.

Willhite, G. P. 1967. Over-all Heat Transfer Coefficients in Steam And Hot Water Injection Wells. *Journal of Petroleum Technology* **19** (5): 607-615. doi: 10.2118/1449-PA.

Yoshioka, K. 2007. Detection of Water or Gas Entry into Horizontal Wells by Using Permanent Downhole Monitoring System. PhD thesis, Texas A&M Univeristy, College Station, Texas.

Yoshioka, K., Zhu, D. and Hill, A. D. 2007a. A New Inversion Method to Interpret Flow Profiles From Distributed Temperature and Pressure Measurements in Horizontal Wells. Paper SPE 109749 presented at SPE Annual Technical Conference and Exhibition, Anaheim, California, 11-14 November. doi:10.2118/109749-MS.

Yoshioka, K., Zhu, D., Hill, A. D., Dawkrajai, P. and Lake, L. W. 2007b. Prediction of Temperature Changes Caused by Water or Gas Entry Into a Horizontal Well. *SPE Production & Operations* **22** (4): 425-433. doi: 10.2118/100209-PA.

Yoshioka, K., Zhu, D., Hill, A. D., Dawkrajai, P. and Lake, L. W. 2005. A Comprehensive Model of Temperature Behavior in a Horizontal Well. Paper SPE 95656 presented at SPE Annual Technical Conference and Exhibition, Dallas, Texas, 9-12 October. doi:10.2118/95656-MS.

APPENDIX A

DIFFERENTIAL SCHEME OF RESERVOIR TEMPERATURE EQUATION

The partial difference equation for reservoir temperature has already been derived from reservoir energy balance as follows:

$$
\begin{aligned}
-&\left[\sum_l \left(\phi S_l \rho_l C_{pl}\right)+(1-\phi)\rho_s C_{ps}\right]\frac{\partial T}{\partial t}+\sum_l\left(\phi S_l \beta_l T \frac{\partial p_l}{\partial t}\right) \\
&=\sum_l \rho_l \bar{u}_l \cdot C_{pl}\nabla T - \nabla\cdot\left(K_{Tt}\nabla T\right)+\sum_l \bar{u}_l\cdot\nabla p_l \\
&\quad -\sum_l \beta_l T\left(\bar{u}_l\cdot\nabla p_l\right)+\sum_l \rho_l\bar{u}_l\cdot\nabla(gD)
\end{aligned}
\qquad \text{............................. (A-1)}
$$

This appendix provides the differential procedure of this equation by Finite Volume Scheme (FVS) method. To avoid the general meaning of i as x direction grid, the subscript l is used to represent the fluid phase, it could be oil, gas, or water.

First, substituting the mass balance equation of each phase

$$
\nabla\cdot\left(\rho_l\bar{u}_l\right)=-\frac{\partial}{\partial t}\left(\phi\rho_l S_l\right)
\qquad \text{... (A-2)}
$$

into Eq. A-1. Then Eq. A-1 becomes:

$$
\begin{aligned}
-&\left[\sum_l C_{pi}\frac{\partial\left(\phi S_l\rho_l T\right)}{\partial t}+(1-\phi)\rho_s C_{ps}\frac{\partial T}{\partial t}\right]+\sum_l\left(\phi S_l\beta_l T\frac{\partial p_l}{\partial t}\right) \\
&=\sum_l C_{pl}\nabla\left(\rho_l\bar{u}_l T\right)-\nabla\cdot\left(K_{Tt}\nabla T\right)+\sum_l\bar{u}_l\cdot\nabla p_l \\
&\quad -\sum_l\beta_l T\left(\bar{u}_l\cdot\nabla p_l\right)+\sum_l\rho_l\bar{u}_l\cdot\nabla(gD)
\end{aligned}
\qquad \text{........................ (A-3)}
$$

For the black oil, three Phase case, Eq. A-3 can be written as

$$-\left[C_{po}\frac{\partial(\phi S_o\rho_o T)}{\partial t}+C_{pw}\frac{\partial(\phi S_w\rho_w T)}{\partial t}+C_{pg}\frac{\partial(\phi S_g\rho_g T)}{\partial t}+(1-\phi)\rho_s C_{ps}\frac{\partial T}{\partial t}\right]$$

$$+\phi\left(S_o\beta_o\frac{\partial p_o}{\partial t}+S_w\beta_w\frac{\partial p_w}{\partial t}+S_g\beta_g\frac{\partial p_g}{\partial t}\right)T$$

$$=\left[C_{po}\nabla\cdot(\rho_o\vec{u}_o T)+C_{pw}\nabla\cdot(\rho_w\vec{u}_w T)+C_{pg}\nabla\cdot(\rho_g\vec{u}_g T)\right]-\nabla\cdot(K_{Tt}\nabla T) \qquad ...\text{ (A-4)}$$

$$-\left(\beta_o\vec{u}_o\cdot\nabla p_o+\beta_w\vec{u}_w\cdot\nabla p_w+\beta_g\vec{u}_g\cdot\nabla p_g\right)T$$

$$+\vec{u}_o\cdot\nabla p_o+\vec{u}_w\cdot\nabla p_w+\vec{u}_g\cdot\nabla p_g+\left(\rho_o\vec{u}_o+\rho_w\vec{u}_w+\rho_g\vec{u}_g\right)\cdot\nabla(gD)$$

RHS Expression of FVS Method

The expansion form for RHS of Eq. A-4 can be written down as:

$$C_{po}\nabla\cdot(\rho_o\vec{u}_o T)+C_{pw}\nabla\cdot(\rho_w\vec{u}_w T)+C_{pg}\nabla\cdot(\rho_g\vec{u}_g T)=$$

$$C_{po}\left(\frac{\partial(\rho_o u_{ox}T)}{\partial x}+\frac{\partial(\rho_o u_{oy}T)}{\partial y}+\frac{\partial(\rho_o u_{oz}T)}{\partial z}\right)$$

$$+C_{pw}\left(\frac{\partial(\rho_w u_{wx}T)}{\partial x}+\frac{\partial(\rho_w u_{wy}T)}{\partial y}+\frac{\partial(\rho_w u_{wz}T)}{\partial z}\right) \qquad\text{................................ (A-5)}$$

$$+C_{pg}\left(\frac{\partial(\rho_g u_{gx}T)}{\partial x}+\frac{\partial(\rho_g u_{gy}T)}{\partial y}+\frac{\partial(\rho_g u_{gz}T)}{\partial z}\right)$$

$$\nabla\cdot(K_{Tt}\nabla T)=\frac{\partial}{\partial x}\left(K_{Tt}\frac{\partial T}{\partial x}\right)+\frac{\partial}{\partial y}\left(K_{Tt}\frac{\partial T}{\partial y}\right)+\frac{\partial}{\partial y}\left(K_{Tt}\frac{\partial T}{\partial y}\right) \qquad\text{........................... (A-6)}$$

$$\left(\beta_o \vec{u}_o \cdot \nabla p_o + \beta_w \vec{u}_w \cdot \nabla p_w + \beta_g \vec{u}_g \cdot \nabla p_g \right) T =$$

$$\beta_o \left(u_{ox} \frac{\partial p_o}{\partial x} + u_{oy} \frac{\partial p_o}{\partial y} + u_{oz} \frac{\partial p_o}{\partial z} \right) T$$

$$+ \beta_w \left(u_{wx} \frac{\partial p_w}{\partial x} + u_{wy} \frac{\partial p_w}{\partial y} + u_{wz} \frac{\partial p_w}{\partial z} \right) T \quad \text{.....................................} \quad \text{(A-7)}$$

$$+ \beta_g \left(u_{gx} \frac{\partial p_g}{\partial x} + u_{gy} \frac{\partial p_g}{\partial y} + u_{gz} \frac{\partial p_g}{\partial z} \right) T$$

$$\vec{u}_o \cdot \nabla p_o + \vec{u}_w \cdot \nabla p_w + \vec{u}_g \cdot \nabla p_g = \left(u_{ox} \frac{\partial p_o}{\partial x} + u_{oy} \frac{\partial p_o}{\partial y} + u_{oz} \frac{\partial p_o}{\partial z} \right) +$$

$$+ \left(u_{wx} \frac{\partial p_w}{\partial x} + u_{wy} \frac{\partial p_w}{\partial y} + u_{wz} \frac{\partial p_w}{\partial z} \right) + \left(u_{gx} \frac{\partial p_g}{\partial x} + u_{gy} \frac{\partial p_g}{\partial y} + u_{gz} \frac{\partial p_g}{\partial z} \right) \quad \text{... (A-8)}$$

$$\left(\rho_o \vec{u}_o + \rho_w \vec{u}_w + \rho_g \vec{u}_g \right) \cdot \nabla (gD) = \left(\rho_o u_{oz} + \rho_w u_{wz} + \rho_g u_{gz} \right) g \quad \text{...........................} \quad \text{(A-9)}$$

Temperature is solved implicitly. The velocity, pressure and saturation fields are use the $n+1$ time step information. Fluid properties are functions of temperature and pressure. During the production, because the temperature change in the whole reservoir is very small, we assume that the properties are only affected by pressure. We use the properties information at new pressure solution, $n+1$ time step, but for temperature, they are at n time step.

Define: i represents x direction, j represents y direction, and k represents z direction. Our field and grids are all rectangular. Δx_i is the length of the ith control volume, δx_i is the distance between $(i-1)th$ and ith points. All the properties are stored

on the points. All the velocities are stored at the interface of grids. The velocity from Darcy's law:

$$\left(u_{lx}\right)_{i-1/2} = -k_x \lambda_{rl} \frac{\left(p_l - \rho g D\right)_i - \left(p_l - \rho g D\right)_{i-1}}{\delta x_i} \quad \text{.. (A-10)}$$

where $\lambda_r = \dfrac{k_r}{\mu}$, and l could be oil, water, or gas. k is absolutely permeability, k_r is relative permeability. And we use upwind scheme for velocity calculation.

Now we apply finite volume scheme to Eq. A-4. For the convection term in temperature, Eq. A-5 has three terms about different fluid phases. Here we just give oil phase term as example (all other terms are the same):

$$\int_{t^n}^{t^{n+1}} \int_{x_{i-1/2}}^{x_{i+1/2}} \int_{y_{j-1/2}}^{y_{j+1/2}} \int_{z_{k-1/2}}^{z_{k+1/2}} C_{po}\left(\frac{\partial(\rho_o u_{ox} T)}{\partial x} + \frac{\partial(\rho_o u_{oy} T)}{\partial y} + \frac{\partial(\rho_o u_{oz} T)}{\partial z}\right) dxdydzdt$$

$$= \left(C_{po}\right)_{i,j,k}^{n+1}\left[\left(\rho_o\right)_{i+1/2,j,k}^{n+1}\left(u_{ox}\right)_{i+1/2,j,k}^{n+1} T_{i+1/2,j,k}^{n+1} - \left(\rho_o\right)_{i-1/2,j,k}^{n+1}\left(u_{ox}\right)_{i-1/2,j,k}^{n+1} T_{i-1/2,j,k}^{n+1}\right]\Delta y_j \Delta z_k \Delta t$$

$$+ \left(C_{po}\right)_{i,j,k}^{n+1}\left[\left(\rho_o\right)_{i,j+1/2,k}^{n+1}\left(u_{oy}\right)_{i,j+1/2,k}^{n+1} T_{i,j+1/2,k}^{n+1} - \left(\rho_o\right)_{i,j-1/2,k}^{n+1}\left(u_{oy}\right)_{i,j-1/2,k}^{n+1} T_{i,j-1/2,k}^{n+1}\right]\Delta x_i \Delta z_k \Delta t$$

$$+ \left(C_{po}\right)_{i,j,k}^{n+1}\left[\left(\rho_o\right)_{i,j,k+1/2}^{n+1}\left(u_{oz}\right)_{i,j,k+1/2}^{n+1} T_{i,j,k+1/2}^{n+1} - \left(\rho_o\right)_{i,j,k-1/2}^{n+1}\left(u_{oz}\right)_{i,j,k-1/2}^{n+1} T_{i,j,k-1/2}^{n+1}\right]\Delta x_i \Delta y_j \Delta t$$

$$\text{...(A-11)}$$

Use upstream scheme for the "1/2" term, which means:

$$\text{If}\left(u_{ox}\right)_{i-1/2,j,k} > 0, \ T_{i-1/2,j,k}^{n+1} = T_{i-1,j,k}^{n+1} \quad \text{..(A-12)}$$

For the thermal conduction term in reservoir, Eq. A-6 can be expressed as:

$$\int\limits_{t^n}^{t^{n+1}} \int\limits_{x_{i-1/2}}^{x_{i+1/2}} \int\limits_{y_{j-1/2}}^{y_{j+1/2}} \int\limits_{z_{k-1/2}}^{z_{k+1/2}} \left[\frac{\partial}{\partial x}\left(K_{Tt}\frac{\partial T}{\partial x}\right) + \frac{\partial}{\partial y}\left(K_{Tt}\frac{\partial T}{\partial y}\right) + \frac{\partial}{\partial z}\left(K_{Tt}\frac{\partial T}{\partial z}\right) \right] dxdydzdt$$

$$= \left[\left(K_{Tt}^{n+1}\left(\frac{\partial T}{\partial x}\right)^{n+1}\right)_{i+1/2,j,k} - \left(K_{Tt}^{n+1}\left(\frac{\partial T}{\partial x}\right)^{n+1}\right)_{i-1/2,j,k} \right]\Delta y_j\Delta z_k\Delta t$$

$$+ \left[\left(K_{Tt}^{n+1}\left(\frac{\partial T}{\partial y}\right)^{n+1}\right)_{i,j+1/2,k} - \left(K_{Tt}^{n+1}\left(\frac{\partial T}{\partial y}\right)^{n+1}\right)_{i,j-1/2,k} \right]\Delta x_i\Delta z_k\Delta t \quad ....(A\text{-}13)$$

$$+ \left[\left(K_{Tt}^{n+1}\left(\frac{\partial T}{\partial z}\right)^{n+1}\right)_{i,j,k+1/2} - \left(K_{Tt}^{n+1}\left(\frac{\partial T}{\partial z}\right)^{n+1}\right)_{i,j,k-1/2} \right]\Delta x_i\Delta y_j\Delta t$$

And for example, $\left(K_{Tt}^{n+1}\left(\frac{\partial T}{\partial x}\right)^{n+1}\right)_{i+1/2,j,k} = \left(K_{Tt}^{n+1}\right)_{i+1/2,j,k}\dfrac{T_{i+1,j,k}^{n+1} - T_{i,j,k}^{n+1}}{\delta x_{i+1}}$. Because it

assumes that the total heat conductivity is constant, it is easy to assign a number for all

grids and their contact surfaces.

For the fluid compressibility term, Eq. A-7, it becomes:

$$\int\limits_{t^n}^{t^{n+1}} \int\limits_{x_{i-1/2}}^{x_{i+1/2}} \int\limits_{y_{j-1/2}}^{y_{j+1/2}} \int\limits_{z_{k-1/2}}^{z_{k+1/2}} \beta_o\left(u_{ox}\frac{\partial p_o}{\partial x} + u_{oy}\frac{\partial p_o}{\partial y} + u_{oz}\frac{\partial p_o}{\partial z}\right)Tdxdydzdt$$

$$= (\beta_o)_{i,j,k}^{n+1}(u_{ox})_{i,j,k}^{n+1}\left[p_{oi+1/2,j,k}^{n+1} - p_{oi-1/2,j,k}^{n+1}\right]T_{i,j,k}^{n+1}\Delta y_j\Delta z_k\Delta t \quad ....(A\text{-}14)$$

$$+ (\beta_o)_{i,j,k}^{n+1}(u_{oy})_{i,j,k}^{n+1}\left[p_{oi,j+1/2,k}^{n+1} - p_{oi,j-1/2,k}^{n+1}\right]T_{i,j,k}^{n+1}\Delta x_i\Delta z_k\Delta t$$

$$+ (\beta_o)_{i,j,k}^{n+1}(u_{oz})_{i,j,k}^{n+1}\left[p_{oi,j,k+1/2}^{n+1} - p_{oi,j,k-1/2}^{n+1}\right]T_{i,j,k}^{n+1}\Delta x_i\Delta y_j\Delta t$$

For the viscous dissipation heating term, Eq. A-8, it is:

$$\int\limits_{t^n}^{t^{n+1}} \int\limits_{x_{i-1/2}}^{x_{i+1/2}} \int\limits_{y_{j-1/2}}^{y_{j+1/2}} \int\limits_{z_{k-1/2}}^{z_{k+1/2}} \left(u_{ox}\frac{\partial p_o}{\partial x} + u_{oy}\frac{\partial p_o}{\partial y} + u_{oz}\frac{\partial p_o}{\partial z}\right)dxdydzdt$$

$$= (u_{ox})_{i,j,k}^{n+1}\left[p_{oi+1/2,j,k}^{n+1} - p_{oi-1/2,j,k}^{n+1}\right]\Delta y_j\Delta z_k\Delta t \quad ....(A\text{-}15)$$

$$+ (u_{oy})_{i,j,k}^{n+1}\left[p_{oi,j+1/2,k}^{n+1} - p_{oi,j-1/2,k}^{n+1}\right]\Delta x_i\Delta z_k\Delta t$$

$$+ (u_{oz})_{i,j,k}^{n+1}\left[p_{oi,j,k+1/2}^{n+1} - p_{oi,j,k-1/2}^{n+1}\right]\Delta x_i\Delta y_j\Delta t$$

For the potential energy term, Eq. A-9 has the following form:

$$\int_{t^n}^{t^{n+1}} \int_{x_{i-1/2}}^{x_{i+1/2}} \int_{y_{j-1/2}}^{y_{j+1/2}} \int_{z_{k-1/2}}^{z_{k+1/2}} \left(\rho_o u_{oz} + \rho_w u_{wz} + \rho_g u_{gz}\right) g \, dxdydzdt$$

$$= \left(\rho_o u_{oz} + \rho_w u_{wz} + \rho_g u_{gz}\right)_{i,j,k}^{n+1} g \Delta x_i \Delta y_j \Delta z_k \Delta t \quad\text{...............................(A-16)}$$

LHS Expression of FVS Method

The LHS of Eq. A-5 includes the accumulative term and the thermal expansion term relative to transient pressure change. For the accumulative term, it is:

$$\int_{t^n}^{t^{n+1}} \int_{x_{i-1/2}}^{x_{i+1/2}} \int_{y_{j-1/2}}^{y_{j+1/2}} \int_{z_{k-1/2}}^{z_{k+1/2}} \left[\frac{C_{po}\partial(\phi S_o \rho_o T)}{\partial t} + \frac{C_{pw}\partial(\phi S_w \rho_w T)}{\partial t} + \frac{C_{pg}\partial(\phi S_g \rho_g T)}{\partial t} + (1-\phi)\rho_s C_{ps}\frac{\partial T}{\partial t} \right] dxdydzdt$$

$$= \left[\begin{array}{c} C_{po}^{n+1}\left((\phi S_o \rho_o T)^{n+1} - (\phi S_o \rho_o T)^n\right) + C_{pw}^{n+1}\left((\phi S_w \rho_w T)^{n+1} - (\phi S_w \rho_w T)^n\right) \\ + C_{pg}^{n+1}\left((\phi S_g \rho_g T)^{n+1} - (\phi S_g \rho_g T)^n\right) \end{array} \right]_{i,j,k} \Delta x_i \Delta y_j \Delta z_k$$

$$+ \left((1-\phi)\rho_s C_{ps}\right)_{i,j,k}^{n+1} \left(T_{i,j,k}^{n+1} - T_{i,j,k}^n\right) \Delta x_i \Delta y_j \Delta z_k$$

$$= \left[\left(C_{po}^{n+1}(\phi S_o \rho_o)^{n+1} + C_{pw}^{n+1}(\phi S_w \rho_w)^{n+1} + C_{pg}^{n+1}(\phi S_g \rho_g)^{n+1} + \left((1-\phi)\rho_s C_{ps}\right)^{n+1}\right)_{i,j,k} T_{i,j,k}^{n+1}\right.$$

$$\left. - \left(C_{po}^{n+1}(\phi S_o \rho_o)^n + C_{pw}^{n+1}(\phi S_w \rho_w)^n + C_{pg}^{n+1}(\phi S_g \rho_g)^n + \left((1-\phi)\rho_s C_{ps}\right)^{n+1}\right)_{i,j,k} T_{i,j,k}^n\right] \Delta x_i \Delta y_j \Delta z_k$$

$$\text{...(A-17)}$$

For the thermal expansion term, the formulation becomes:

$$\int_{t^n}^{t^{n+1}} \int_{x_{i-1/2}}^{x_{i+1/2}} \int_{y_{j-1/2}}^{y_{j+1/2}} \int_{z_{k-1/2}}^{z_{k+1/2}} \phi\left(S_o\beta_o\frac{\partial p_o}{\partial t} + S_w\beta_w\frac{\partial p_w}{\partial t} + S_g\beta_g\frac{\partial p_g}{\partial t}\right) T dxdydzdt$$

$$= \left[(\phi(S_o\beta_o))_{i,j,k}^{n+1}\left(p_{oi,j,k}^{n+1} - p_{oi,j,k}^n\right) + (\phi(S_w\beta_w))_{i,j,k}^{n+1}\left(p_{wi,j,k}^{n+1} - p_{wi,j,k}^n\right)\right. \quad\text{...................(A-18)}$$

$$\left. + (\phi(S_g\beta_g))_{i,j,k}^{n+1}\left(p_{gi,j,k}^{n+1} - p_{gi,j,k}^n\right)\right] \cdot T_{i,j,k}^{n+1} \Delta x_i \Delta y_j \Delta z_k$$

General Expression for Discretized Equation

Substituting Eq. A-11 through Eq. A-18 into Eq. 4, and rearranging it, the general discretized equation is given by:

$$AP_{i,j,k}T_{i,j,k}^{n+1} = AW_{i,j,k}T_{i-1,j,k}^{n+1} + AE_{i,j,k}T_{i+1,j,k}^{n+1} + AS_{i,j,k}T_{i,j-1,k}^{n+1} + AN_{i,j,k}T_{i,j+1,k}^{n+1}$$
$$+ AB_{i,j,k}T_{i,j,k-1}^{n+1} + AT_{i,j,k}T_{i,j,k+1}^{n+1} + B_{i,j,k} \quad \ldots\ldots \text{(A-19)}$$

First, declare $\llbracket a, \quad 0 \rrbracket = \max(a, \quad 0)$; Then

$$AW_{i,j,k} = \left(\frac{\left(K_{Tt}^{n+1}\right)_{i-1/2,j,k}}{\delta x_i} + \left(C_{po}\right)_{i,j,k}^{n+1} \left\llbracket \left(\rho_o u_{ox}\right)_{i-1/2,j,k}^{n+1}, \quad 0 \right\rrbracket \right.$$
$$+ \left(C_{pw}\right)_{i,j,k}^{n+1} \left\llbracket \left(\rho_w u_{wx}\right)_{i-1/2,j,k}^{n+1}, \quad 0 \right\rrbracket \qquad \ldots\ldots\ldots\ldots\ldots\ldots\text{(A-20)}$$
$$+ \left(C_{pg}\right)_{i,j,k}^{n+1} \left\llbracket \left(\rho_g u_{gx}\right)_{i-1/2,j,k}^{n+1}, \quad 0 \right\rrbracket \right) \Delta y_j \Delta z_k \Delta t$$

$$AE_{i,j,k} = \left(\frac{\left(K_{Tt}^{n+1}\right)_{i+1/2,j,k}}{\delta x_{i+1}} + \left(C_{po}\right)_{i,j,k}^{n+1} \left\llbracket -\left(\rho_o u_{ox}\right)_{i+1/2,j,k}^{n+1}, \quad 0 \right\rrbracket \right.$$
$$+ \left(C_{pw}\right)_{i,j,k}^{n+1} \left\llbracket -\left(\rho_w u_{wx}\right)_{i+1/2,j,k}^{n+1}, \quad 0 \right\rrbracket \qquad \ldots\ldots\ldots\ldots\ldots\text{(A-21)}$$
$$+ \left(C_{pg}\right)_{i,j,k}^{n+1} \left\llbracket -\left(\rho_g u_{gx}\right)_{i+1/2,j,k}^{n+1}, \quad 0 \right\rrbracket \right) \Delta y_j \Delta z_k \Delta t$$

$$AS_{i,j,k} = \left(\frac{\left(K_{Tt}^{n+1}\right)_{i,j-1/2,k}}{\delta y_j} + \left(C_{po}\right)_{i,j,k}^{n+1} \left\llbracket \left(\rho_o u_{oy}\right)_{i,j-1/2,k}^{n+1}, \quad 0 \right\rrbracket \right.$$
$$+ \left(C_{pw}\right)_{i,j,k}^{n+1} \left\llbracket \left(\rho_w u_{wy}\right)_{i,j-1/2,k}^{n+1}, \quad 0 \right\rrbracket \qquad \ldots\ldots\ldots\ldots\ldots\ldots\text{(A-22)}$$
$$+ \left(C_{pg}\right)_{i,j,k}^{n+1} \left\llbracket \left(\rho_g u_{gy}\right)_{i,j-1/2,k}^{n+1}, \quad 0 \right\rrbracket \right) \Delta x_i \Delta z_k \Delta t$$

$$AN_{i,j,k} = \left(\frac{\left(K_{Tt}^{n+1}\right)_{i,j+1/2,k}}{\delta y_{j+1}} + \left(C_{po}\right)_{i,j,k}^{n+1} \left[\!\left[-\left(\rho_o u_{oy}\right)_{i,j+1/2,k}^{n+1} , \quad 0 \right]\!\right] \right.$$

$$+ \left(C_{pw}\right)_{i,j,k}^{n+1} \left[\!\left[-\left(\rho_w u_{wy}\right)_{i,j+1/2,k}^{n+1} , \quad 0 \right]\!\right] \qquad \text{............................(A-23)}$$

$$\left. + \left(C_{pg}\right)_{i,j,k}^{n+1} \left[\!\left[-\left(\rho_g u_{gy}\right)_{i,j+1/2,k}^{n+1} , \quad 0 \right]\!\right] \right) \Delta x_i \Delta z_k \Delta t$$

$$AB_{i,j,k} = \left(\frac{\left(K_{Tt}^{n+1}\right)_{i,j,k-1/2}}{\delta z_k} + \left(C_{po}\right)_{i,j,k}^{n+1} \left[\!\left[\left(\rho_o u_{oz}\right)_{i,j,k-1/2}^{n+1} , \quad 0 \right]\!\right] \right.$$

$$+ \left(C_{pw}\right)_{i,j,k}^{n+1} \left[\!\left[\left(\rho_w u_{wz}\right)_{i,j,k-1/2}^{n+1} , \quad 0 \right]\!\right] \qquad \text{...........................(A-24)}$$

$$\left. + \left(C_{pg}\right)_{i,j,k}^{n+1} \left[\!\left[\left(\rho_g u_{gz}\right)_{i,j,k-1/2}^{n+1} , \quad 0 \right]\!\right] \right) \Delta x_i \Delta y_j \Delta t$$

$$AT_{i,j,k} = \left(\frac{\left(K_{Tt}^{n+1}\right)_{i,j,k+1/2}}{\delta z_{k+1}} + \left(C_{po}\right)_{i,j,k}^{n+1} \left[\!\left[-\left(\rho_o u_{oz}\right)_{i,j,k+1/2}^{n+1} , \quad 0 \right]\!\right] \right.$$

$$+ \left(C_{pw}\right)_{i,j,k}^{n+1} \left[\!\left[-\left(\rho_w u_{wz}\right)_{i,j,k+1/2}^{n+1} , \quad 0 \right]\!\right] \qquad \text{...........................(A-25)}$$

$$\left. + \left(C_{pg}\right)_{i,j,k}^{n+1} \left[\!\left[-\left(\rho_g u_{gz}\right)_{i,j,k+1/2}^{n+1} , \quad 0 \right]\!\right] \right) \Delta x_i \Delta y_j \Delta t$$

and

$$AP_{i,j,k} = AP_{1i,j,k} + AP_{2i,j,k} + AP_{3i,j,k} + AP_{4i,j,k} \text{ ....(A-26)}$$

where:

$AP_{1i,j,k}$: The coefficients from conductivity and convection terms.

$AP_{2i,j,k}$: The coefficients from the nondeterministic term, time-dependent term.

$AP_{3i,j,k}$: The coefficients from the space pressure compressible term.

$AP_{4i,j,k}$: The coefficients from the time pressure compressible term.

The detailed expressions of these four components are written as follows:

$$
\begin{aligned}
AP_{1i,j,k} = {} & \left[\frac{\left(K_{Tt}^{n+1}\right)_{i-1/2,j,k}}{\delta x_i} + \frac{\left(K_{Tt}^{n+1}\right)_{i+1/2,j,k}}{\delta x_{i+1}} + \sum_{l=1}^{3}\left(C_{pl}\right)_{i,j,k}^{n+1}\left[\left(\rho_l u_{lx}\right)_{i+1/2,j,k}^{n+1},\quad 0\right] + \right. \\
& \left. \sum_{l=1}^{3}\left(C_{pl}\right)_{i,j,k}^{n+1}\left[-\left(\rho_l u_{lx}\right)_{i-1/2,j,k}^{n+1},\quad 0\right] \right] \Delta y_j \Delta z_k \Delta t \\[2ex]
& + \left[\frac{\left(K_{Tt}^{n+1}\right)_{i,j-1/2,k}}{\delta y_j} + \frac{\left(K_{Tt}^{n+1}\right)_{i,j+1/2,k}}{\delta y_{j+1}} + \sum_{l=1}^{3}\left(C_{pl}\right)_{i,j,k}^{n+1}\left[\left(\rho_l u_{ly}\right)_{i,j+1/2,k}^{n+1},\quad 0\right] + \right. \\
& \left. \sum_{l=1}^{3}\left(C_{pl}\right)_{i,j,k}^{n+1}\left[-\left(\rho_l u_{ly}\right)_{i,j-1/2,k}^{n+1},\quad 0\right] \right] \Delta x_i \Delta z_k \Delta t \\[2ex]
& + \left[\frac{\left(K_{Tt}^{n+1}\right)_{i,j,k-1/2}}{\delta z_k} + \frac{\left(K_{Tt}^{n+1}\right)_{i+1/2,j,k}}{\delta z_{k+1}} + \sum_{l=1}^{3}\left(C_{pl}\right)_{i,j,k}^{n+1}\left[\left(\rho_l u_{lz}\right)_{i,j,k+1/2}^{n+1},\quad 0\right] + \right. \\
& \left. \sum_{l=1}^{3}\left(C_{pl}\right)_{i,j,k}^{n+1}\left[-\left(\rho_l u_{lz}\right)_{i,j,k-1/2}^{n+1},\quad 0\right] \right] \Delta x_i \Delta y_j \Delta t
\end{aligned}
$$

....(A-27)

$$
\begin{aligned}
AP_{2i,j,k} = {} & \left(C_{po}^{n+1}\left(\phi S_o \rho_o\right)^{n+1} + C_{pw}^{n+1}\left(\phi S_w \rho_w\right)^{n+1} \right. \\
& \left. + C_{pg}^{n+1}\left(\phi S_g \rho_g\right)^{n+1} + \left((1-\phi)\rho_s C_{ps}\right)^{n+1} \right)_{i,j,k} \Delta x_i \Delta y_j \Delta z_k
\end{aligned}
$$

...................(A-28)

$$
\begin{aligned}
-AP_{3i,j,k} = {} & \left(\beta_o u_{ox}\right)_{i,j,k}^{n+1}\left[p_{oi+1/2,j,k}^{n+1} - p_{oi-1/2,j,k}^{n+1}\right]\Delta y_j \Delta z_k \Delta t \\
& + \left(\beta_o u_{oy}\right)_{i,j,k}^{n+1}\left[p_{oi,j+1/2,k}^{n+1} - p_{oi,j-1/2,k}^{n+1}\right]\Delta x_i \Delta z_k \Delta t \\
& + \left(\beta_o u_{oz}\right)_{i,j,k}^{n+1}\left[p_{oi,j,k+1/2}^{n+1} - p_{oi,j,k-1/2}^{n+1}\right]\Delta x_i \Delta y_j \Delta t \\
& + \left(\beta_w u_{wx}\right)_{i,j,k}^{n+1}\left[p_{wi+1/2,j,k}^{n+1} - p_{wi-1/2,j,k}^{n+1}\right]\Delta y_j \Delta z_k \Delta t \\
& + \left(\beta_w u_{wy}\right)_{i,j,k}^{n+1}\left[p_{wi,j+1/2,k}^{n+1} - p_{wi,j-1/2,k}^{n+1}\right]\Delta x_i \Delta z_k \Delta t \\
& + \left(\beta_w u_{wz}\right)_{i,j,k}^{n+1}\left[p_{wi,j,k+1/2}^{n+1} - p_{wi,j,k-1/2}^{n+1}\right]\Delta x_i \Delta y_j \Delta t \\
& + \left(\beta_g u_{gx}\right)_{i,j,k}^{n+1}\left[p_{gi+1/2,j,k}^{n+1} - p_{gi-1/2,j,k}^{n+1}\right]\Delta y_j \Delta z_k \Delta t \\
& + \left(\beta_g u_{gy}\right)_{i,j,k}^{n+1}\left[p_{gi,j+1/2,k}^{n+1} - p_{gi,j-1/2,k}^{n+1}\right]\Delta x_i \Delta z_k \Delta t \\
& + \left(\beta_g u_{gz}\right)_{i,j,k}^{n+1}\left[p_{gi,j,k+1/2}^{n+1} - p_{gi,j,k-1/2}^{n+1}\right]\Delta x_i \Delta y_j \Delta t
\end{aligned}
$$

................................(A-29)

$$AP_{4i,j,k} = -\Big[\big(\phi(S_o\beta_o)\big)_{i,j,k}^{n+1}\big(p_{oi,j,k}^{n+1} - p_{oi,j,k}^{n}\big) + \big(\phi(S_w\beta_w)\big)_{i,j,k}^{n+1}\big(p_{wi,j,k}^{n+1} - p_{wi,j,k}^{n}\big)$$
$$+ \big(\phi(S_g\beta_g)\big)_{i,j,k}^{n+1}\big(p_{gi,j,k}^{n+1} - p_{gi,j,k}^{n}\big)\Big] \cdot \Delta x_i \Delta y_j \Delta z_k \qquad \text{......(A-30)}$$

From the mass balance, Eq. A-2, we can find that

$$AP_{1i,j,k} + AP_{2i,j,k} = AW_{i,j,k} + AE_{i,j,k} + AS_{i,j,k} + AN_{i,j,k} + AB_{i,j,k} + AT_{i,j,k}$$
$$+ \big(C_{po}^n(\phi S_o\rho_o)^n + C_{pw}^n(\phi S_w\rho_w)^n + C_{pg}^n(\phi S_g\rho_g)^n\big)_{i,j,k}\Delta x_i \Delta y_j \Delta z_k$$
$$+ \big((1-\phi)\rho_s C_{ps}\big)_{i,j,k}^{n+1}\Delta x_i \Delta y_j \Delta z_k \qquad \text{.........(A-31)}$$
$$= AW_{i,j,k} + AE_{i,j,k} + AS_{i,j,k} + AN_{i,j,k} + AB_{i,j,k} + AT_{i,j,k} + AP'_{2i,j,k}$$

where

$$AP'_{2i,j,k} = \big(C_{po}^n(\phi S_o\rho_o)^n + C_{pw}^n(\phi S_w\rho_w)^n + C_{pg}^n(\phi S_g\rho_g)^n\big)_{i,j,k}\Delta x_i \Delta y_j \Delta z_k$$
$$+ \big((1-\phi)\rho_s C_{ps}\big)_{i,j,k}^{n+1}\Delta x_i \Delta y_j \Delta z_k \qquad \text{...............(A-32)}$$

Therefore,

$$AP_{i,j,k} = AW_{i,j,k} + AE_{i,j,k} + AS_{i,j,k} + AN_{i,j,k} + AB_{i,j,k} + AT_{i,j,k}$$
$$+ AP'_{2i,j,k} + AP_{3i,j,k} + AP_{4i,j,k} \qquad \text{.....................(A-33)}$$

With Eq. A-31, there is another way to calculate $AP_{1i,j,k}$, and $AP_{2i,j,k}$ is replaced

by $AP'_{2i,j,k}$.

For the source term, $B_{i,j,k}$, its formulation is:

$$B_{i,j,k} = B_{1i,j,k} + B_{2i,j,k} + B_{3i,j,k} \text{ ....(A-34)}$$

where

$B_{1i,j,k}$: From Eq. A-15, the viscous dissipation heating term.

$B_{2i,j,k}$: From Eq. A-16, the potential energy, gravity term.

$B_{3i,j,k}$: From previous time step temperature, $T_{i,j,k}^n$

The detailed expressions are:

$$
\begin{aligned}
- B_{1i,j,k} =\ & (u_{ox})_{i,j,k}^{n+1} \left(p_{oi+1/2,j,k}^{n+1} - p_{oi-1/2,j,k}^{n+1} \right) \Delta y_j \Delta z_k \Delta t \\
& + (u_{oy})_{i,j,k}^{n+1} \left(p_{oi,j+1/2,k}^{n+1} - p_{oi,j-1/2,k}^{n+1} \right) \Delta x_i \Delta z_k \Delta t \\
& + (u_{oz})_{i,j,k}^{n+1} \left(p_{oi,j,k+1/2}^{n+1} - p_{oi,j,k-1/2}^{n+1} \right) \Delta x_i \Delta y_j \Delta t + (u_{wx})_{i,j,k}^{n+1} \left(p_{wi+1/2,j,k}^{n+1} - p_{wi-1/2,j,k}^{n+1} \right) \Delta y_j \Delta z_k \Delta t \\
& + (u_{wy})_{i,j,k}^{n+1} \left(p_{wi,j+1/2,k}^{n+1} - p_{wi,j-1/2,k}^{n+1} \right) \Delta x_i \Delta z_k \Delta t + (u_{wz})_{i,j,k}^{n+1} \left(p_{wi,j,k+1/2}^{n+1} - p_{wi,j,k-1/2}^{n+1} \right) \Delta x_i \Delta y_j \Delta t \\
& + (u_{gx})_{i,j,k}^{n+1} \left(p_{gi+1/2,j,k}^{n+1} - p_{gi-1/2,j,k}^{n+1} \right) \Delta y_j \Delta z_k \Delta t + (u_{gy})_{i,j,k}^{n+1} \left(p_{gi,j+1/2,k}^{n+1} - p_{gi,j-1/2,k}^{n+1} \right) \Delta x_i \Delta z_k \Delta t \\
& + (u_{gz})_{i,j,k}^{n+1} \left(p_{gi,j,k+1/2}^{n+1} - p_{gi,j,k-1/2}^{n+1} \right) \Delta x_i \Delta y_j \Delta t
\end{aligned}
$$

$$\text{...(A-35)}$$

$$
B_{2i,j,k} = -\left(\rho_o u_{oz} + \rho_w u_{wz} + \rho_g u_{gz} \right)_{i,j,k}^{n+1} g \Delta x_i \Delta y_j \Delta z_k \Delta t \text{ ....(A-36)}
$$

$$
\begin{aligned}
B_{3i,j,k} =\ & \left(C_{po}^{n+1} (\phi S_o \rho_o)^n + C_{pw}^{n+1} (\phi S_w \rho_w)^n + C_{pg}^{n+1} (\phi S_g \rho_g)^n \right. \\
& \left. + \left((1-\phi) \rho_s C_{ps} \right)^{n+1} \right)_{i,j,k} T_{i,j,k}^n \Delta x_i \Delta y_j \Delta z_k
\end{aligned}
$$

$$\text{...............................(A-37)}$$

The Variance Value at Grid Surface

As mentioned before, all the properties are stored on the points. All the velocities are stored at the interface of grids.

For pressure, use arithmetic average, which means pressure is linear change between too grid centers.

$$
p_{li-1/2,j,k} = \left(p_{li-1,j,k} \cdot \Delta x_{i-1} + p_{li,j,k} \cdot \Delta x_i \right) / (\Delta x_{i-1} + \Delta x_i)
$$

$$
p_{li,j-1/2,k} = \left(p_{li,j-1,k} \cdot \Delta y_{j-1} + p_{li,j,k} \cdot \Delta y_j \right) / (\Delta y_{j-1} + \Delta y_j)
$$

$$
p_{li,j,k-1/2} = \left(p_{li,j,k-1} \cdot \Delta z_{k-1} + p_{li,j,k} \cdot \Delta z_k \right) / (\Delta z_{k-1} + \Delta z_k)
$$

For velocity, $(u_{lx})_{i-1/2,j,k} = -(k_x \lambda_{rl})_{i-1/2,j,k} \dfrac{(p_l)_i - (p_l)_{i-1}}{\delta x_i}$, where k_x is the absolute

permeability, $\lambda_r = \dfrac{k_r}{\mu}$, k_r is the relative permeability, μ is the viscosity.

Harmonic average for k_x

$$k_{xi-1/2,j,k} = \delta x_i \left(\frac{\Delta x_{i-1}/2}{k_{xi-1,j,k}} + \frac{\Delta x_i/2}{k_{xi,j,k}} \right)^{-1}, \text{ where } \delta x_i = (\Delta x_{i-1} + \Delta x_i)/2$$

Upstream scheme for relative permeability k_r

If $(p_l)_{i-1} \geq (p_l)_i$, $k_{ri-1/2,j,k} = k_{ri-1,j,k}$, else $k_{ri-1/2,j,k} = k_{ri,j,k}$

Arithmetic average for viscosity μ

$$\mu_{li-1/2,j,k} = (\mu_{li-1,j,k} \cdot \Delta x_{i-1} + \mu_{li,j,k} \cdot \Delta x_i)/(\Delta x_{i-1} + \Delta x_i)$$

And the velocity on the point, because the ½ is at the grid surface (edge), so for these

velocities: $u_{oi,j,k}, u_{wi,j,k}\ u_{gi,j,k}$

$$u_{lxi,j,k} = (u_{lxi-1/2,j,k} + u_{lxi+1/2,j,k})/2,$$

$$u_{lyi,j,k} = (u_{lyi,j-1/2,k} + u_{lyi,j+1/2,k})/2,$$

$$u_{lzi,j,k} = (u_{lzi,j,k-1/2} + u_{lzi,j,k+1/2})/2$$

For heat conductivity K_{Tt}, use harmonic average

$$\frac{\delta x_i}{(K_{Tt})_{i-1/2,j,k}} = \frac{\Delta x_{i-1}/2}{(K_{Tt})_{i-1,j,k}} + \frac{\Delta x_i/2}{(K_{Tt})_{i,j,k}}, \text{ for rectangular grids: } \delta x_i = (\Delta x_{i-1} + \Delta x_i)/2$$

So $(K_{Tt})_{i-1/2,j,k} = \delta x_i \left(\dfrac{\Delta x_{i-1}/2}{(K_{Tt})_{i-1,j,k}} + \dfrac{\Delta x_i/2}{(K_{Tt})_{i,j,k}} \right)^{-1}$

and $(K_{Tt})_{i+1/2,j,k} = \delta x_{i+1} \left(\dfrac{\Delta x_i/2}{(K_{Tt})_{i,j,k}} + \dfrac{\Delta x_{i+1}/2}{(K_{Tt})_{i+1,j,k}} \right)^{-1}$

For each phase density, ρ_o, ρ_w, ρ_g, use arithmetic average:

$\rho_{li-1/2,j,k} = \left(\rho_{li-1,j,k} \cdot \Delta x_{i-1} + \rho_{li,j,k} \cdot \Delta x_i \right) / (\Delta x_{i-1} + \Delta x_i)$, l=1, 2, 3, which can represent oil, water, and gas.

Now, with all equations above, we obtain a large linear matrix of temperature equations:

$$\mathbf{A}\,\mathbf{T} = \mathbf{B}$$ ....(A-38)

where $\mathbf{A}$ is the coefficients matrix, which is a large sparse matrix, $\mathbf{T}$ is the unknown temperature vector, and $\mathbf{B}$ is the source term.

The coefficients matrix $\mathbf{A}$ has seven linear domains which include non-zero elements, and all other elements in matrix $\mathbf{A}$ are zero.

$$\mathbf{A} = \begin{bmatrix}
* & * & & & & & * & & & & & & * & & & \\
* & * & * & & & & & * & & & & & & * & & \\
& * & * & * & & & & & * & & & & & & * & \\
& & * & * & * & & & & & * & & & & & & * \\
& & & * & * & & & & & & & & & & & \\
* & & & & & & * & * & & & & & & & & \\
& * & & & & & * & * & * & & & & * & & & \\
& & * & & & & & * & * & * & & & & * & & \\
& & & * & & & & & * & * & * & & & & * & \\
& & & & & & & & & * & * & & & & & * \\
& & & & & & & & & & * & * & & & & \\
* & & & & & & * & & & & & * & * & * & & \\
& * & & & & & & * & & & & & * & * & * & \\
& & * & & & & & & * & & & & & * & * & * \\
& & & * & & & & & & * & & & & & * & * \\
\end{bmatrix}$$

Then, a program can be developed to solve this set of equations and obtain temperature behavior in reservoir.

VITA

Name: Zhuoyi Li

Contact: c/o Dr. Ding Zhu

                  Department of Petroleum Engineering

                  Texas A&M University

                  College Station, TX 77843-3116

Email Address: lizhuoyi99@gmail.com

Education: B.E., Engineering Mechanics, Tsinghua University, 2003
                  M.E., School of Aerospace, Tsinghua University. 2005
                  Ph. D, Petroleum Engineering, Texas A&M University, 2010